

Final Technical Report

(2)

DARPA Order No. ~~541-008 dar 01~~

9526/ONR

DARPA Contract No. N00014-88-K-0392

Title: Superionics

**AD-A240 352**

Period: 1 May 1988 - 30 April 1991



Principal Investigator: Richard F. Wallis

Telephone No.: 714-856-6393

*University of California, Irvine*

**DTIC**  
**S** **ELECTE** **D**  
**D** **SEP 12 1991**

This document has been approved  
for public release and sale; its  
distribution is unlimited.

**91-10411**

APPROVED FOR PUBLIC RELEASE  
DISTRIBUTION UNLIMITED

**91 9 12 026**

## TABLE OF CONTENTS

I. Report Summary.....	1
A. Dynamical Properties of Fast Ion Conducting Borate Glasses..	2
B. Effect of Intercalated Lithium on the Electronic Structure of Indium Selenide.....	2
C. Lattice Vibrational Properties of Lithium-Intercalated Indium Selenide.....	3
D. Molecular Dynamics Study of the Lattice Vibration Contribution to the Frequency-Dependent Dielectric Constant of Lithium Iodide.....	3
II. Detailed Project Reports.....	5
A. Dynamical Properties of Fast Ion Conducting Borate Glasses..	5
B. Effect of Intercalated Lithium on the Electronic Structure of Indium Selenide.....	70
C. Lattice Vibrational Properties of Lithium-Intercalated Indium Selenide.....	86
D. Molecular Dynamics Study of the Lattice Vibration Contribution to the Frequency-Dependent Dielectric Constant of Lithium Iodide.....	100
III. Publications.....	130
IV. Ph.D. Theses Completed.....	131



Accession For	
NTIS	CRA&I <input checked="" type="checkbox"/>
DTIC	TAB <input type="checkbox"/>
Unannounced <input type="checkbox"/>	
Justification .....	
By <i>per ltr</i>	
Distribution /	
Availability Codes	
Dist	Avail and/or Special
A-1	

## I. Report Summary

The research supported by DARPA Contract No. N00014-88-K-0392 concerns the investigation of the physical properties of the components of a new solid state microbattery. This battery consists of a lithium metal anode, a lithium borate glass separator, and a cathode of the layer compound InSe which readily intercalates lithium ions and which is also an electronic conductor. The battery operates by the passage of lithium ions between the electrodes through the borate glass separator and the passage of electrons between the electrodes via the external circuit. A single battery of this type produces a voltage of 2.7 V, can be discharged with a current density of  $50\mu Acm^{-2}$  and can achieve a specific energy of  $300Wh\ kg^{-1}$ . It is the ultimate objective of this project to produce systems composed of many microbatteries for applications requiring high voltage, high current density and/or high energy density.

In order to achieve this objective, it is necessary to have a fundamental understanding of fast ion transport in the lithium borate glasses and of both fast ion and electron transport in the layer compound. This fundamental understanding has been advanced by both experimental and theoretical work, the experimental work being carried out at the Laboratoire de Physique des Solides in Paris by the group of Professor M. Balkanski of the Université Pierre et Marie Curie, and the theoretical work being carried out at the University of California, Irvine, under this contract. For the lithium borate glasses the experimental work has provided measurements of ionic conductivity as well as infrared and Raman spectra, while the theoretical work has provided a quantitative understanding of ion migration and interionic forces. For the lithium-intercalated layer compound InSe, the experimental studies have yielded important data on optical properties due to electronic transitions and on infrared and Raman spectra. The theoretical studies have yielded the electronic band structure of lithium intercalated InSe

and detailed information on interionic forces in this material. The results of the investigations just described provide the basis for establishing the desired fundamental understanding of fast ion and electron transport in the microbattery components.

Summaries of the individual projects now follow.

A. Dynamical Properties of Fast Ion Conducting Borate Glasses

Experimental and theoretical investigations which lead to an improved understanding of the physics of ion diffusion in lithium-doped borate glasses have been carried out. The results of network dynamics and lattice dynamics calculations of the atomic vibrations of undoped and doped borate glasses, i.e.,  $B_2O_3$  and  $B_2O_3 - xLi_2O$ , respectively, have been correlated with Raman scattering and infrared reflectivity measurements. Addition of the modifier  $Li_2O$  has been shown to cause a transformation of three-coordinated to four-coordinated boron atoms. The force constant for  $B-O$  interactions has been found to be larger for four-coordinated boron than for three-coordinated boron. The introduction of dopants, e.g.,  $Li_2SO_4$  or  $LiX$  (with  $X = F, Cl, Br, I$ ) leads to a significant increase in the ionic conductivity.

B. Effect of Intercalated Lithium on the Electronic Structure of Indium Selenide

The effect of intercalated lithium on the electronic structure of the  $\beta$ - and  $\gamma$ - polytypes of InSe has been investigated using a tight-binding model. The energy bands of the pure polytypes were calculated and the results compared with previous work. The tight-binding parameters associated with intercalated lithium atoms were obtained using tabulated atomic functions. The modifications of the energy bands and Fermi level produced by the introduction of one lithium atom per unit cell were calculated for the lowest potential energy positions of the lithium atom in the Van der Waals gap between layers. The intercalation

induced changes in the smallest and next-to-smallest direct band gaps were determined. An interpretation of a new photoluminescence peak in lithium-intercalated InSe has been developed, and the existence of a lithium impurity band in this material has been established.

C. Lattice Vibrational Properties of Lithium-Intercalated Indium Selenide

A theoretical investigation of the normal modes of vibration of pure and lithium-intercalated InSe has been carried out. Lattice dynamical models have been developed for both materials. The force constants were determined by fitting calculated normal mode frequencies to experimental infrared and Raman spectra. It has been found that localized vibrational modes associated with lithium-atom vibrations appear in the lithium-intercalated InSe. One localized mode occurs at a very high frequency and corresponds to a lithium atom vibrating perpendicular to the layer plane, while a second localized mode occurs at a much lower frequency and corresponds to a lithium atom vibrating parallel to the layer plane. The results of this investigation provide precise information concerning the forces of interaction between an intercalated lithium atom and the neighboring indium and selenium atoms.

D. Molecular Dynamics Study of the Lattice Vibration Contribution to the Frequency-Dependent Dielectric Constant of Lithium Iodide

A promising approach to realistic calculations of fast ion dynamics in lithium borate glasses involves molecular dynamics whereby one solves the classical equations of motion of the ions on a computer for a given set of interionic potentials. This is a very complicated problem for a disordered system such as a glass, so we have started this project by performing a molecular dynamics simulation of a simpler system, namely, the crystal lithium iodide, *LiI*. A rigid ion potential was used with parameters fit to thermal expansion, isothermal compressibility, lattice energy, and the frequency of the transverse optical mode at

the zone center. The current-current correlation function was calculated at  $T = 200K$  and  $400K$ , and from this function the real and imaginary parts of the dielectric function as functions of frequency were obtained. Anharmonic broadening was observed at the higher temperature. The experience gained from this calculation will be of great value in carrying out the more difficult molecular dynamics simulation for a lithium borate glass.

## II. Detailed Project Reports

### A. Dynamical Properties of Fast Ion Conducting Borate Glasses

M. Balkanski\*, R. F. Wallis, J. Deppe

Department of Physics  
University of California  
Irvine, CA 92717, U.S.A.

M. Massot

Laboratoire de Physiques des Solides  
Universite Pierre et Marie Curie  
4, place Jussieu, 75252 Paris Cedex 05, FRANCE

#### 1. Introduction

Fast ion conducting glasses have attracted considerable interest in recent years in view of their use as separators in solid state batteries. A solid state cell is formed of three components: an ion source, usually Li; a dielectric insulator but good ion conductor such as the lithium borate glass, for example, which acts as a separator between the anode, ion source and the cathode or electron exchanger; and an insertion compound acting as an electron exchanger. The requirements of the separator are to be shape adaptable in order to assure good contact with the ion source and the exchanger and to have a good ionic conductivity. Another important characteristic is that the separator should be as perfect a dielectric as possible in order to prevent electronic leakage and assure a long shelf lifetime of the batteries. The borate glasses are one of the best materials among those known

today to respond to all these requirements.

The boron oxide glass is a very good insulator and constitutes the glass former. Upon the addition of a modifier such as  $\text{Li}_2\text{O}$ , for example, the structure of the glass is significantly changed. In addition, some fraction of the  $\text{Li}_2\text{O}$  dissociates releasing free lithium ions and thus considerably increasing the ion conductivity of the glass. A further increase of the conductivity is achieved by adding a dopant containing the mobile ion, Li in this case. The effect of the dopant upon the concentration of free ions available for the conduction process has been investigated recently [1]. Spectroscopic investigations on the structure of borate glasses with different modifier concentrations and different dopants have also been extensively developed and a summary is given in a recent publication [2].

The structural modifications conditioning the fast ion conduction in borate glasses are inferred mainly from spectroscopic data which reflects the dynamical properties of the glass matrix. It was therefore important to develop theoretical studies on the vibrations of the glass in parallel with the experimental investigations. We shall present here simultaneously the theoretical and experimental results on the vibrational properties of the borate glass with the aim of reaching some conclusions on the conditions for increasing the ionic conductivity of the glass. In successive chapters we shall deal with the vibrations of pure borate glass, Chapter 2, and with the modifications occurring when different concentrations of  $\text{Li}_2\text{O}$  are added to the borate glass, Chapter 3. Chapter 4 will be devoted to the effect of different dopants, and in Chapter 5 we shall discuss the effect of the glass structure on the lithium mobility and present a

statistical mechanical theory of ionic conductivity. In Chapter 6 a double well model of frequency-dependent conductivity will be discussed.

## 2. Vibrations of Boron Oxide Glass

The structure of the boron oxide glass has been studied by X-ray [3], Raman [4], infrared [5], nuclear magnetic resonance [6] and neutron diffraction [7] measurements. According to these observations, boron oxide glass is formed of an infinite network of boroxol groups  $B_3O_3$ . The six atoms inside the group form a planar ring and the B-O-B angle is  $120^\circ$ . These boroxol hexagons are interconnected by an oxygen bridge -O- and the external B-O-B angle  $\theta$ , less accurately determined, is about  $130^\circ$ . The relative geometry of two successive boroxol planes is not well known.

One of the characteristic features of the vibrational spectra of  $v\text{-}B_2O_3$  observed by Raman scattering [2] and shown in Fig. 1 is the presence of a sharp peak at  $800\text{ cm}^{-1}$  which is strong and well polarized [8]. Usually the vibrational spectra of amorphous solids are expected to consist of broad bands (see for example ref. 9). This is because the localized molecular mode responsible for a sharp peak couples with all other atoms and broadens when a network is formed. For example, Galeener et al. [8] have calculated vibrations of  $v\text{-}B_2O_3$  using the Bethe lattice approximation (described in detail below) and obtained only broad bands due to extended modes.

There have been a few attempts to understand theoretically the possible existence of sharp features in the vibrational spectra. Kristiansen and Krogh-Moe [10] calculated the vibrational frequencies of the boroxol molecule with atoms of variable mass

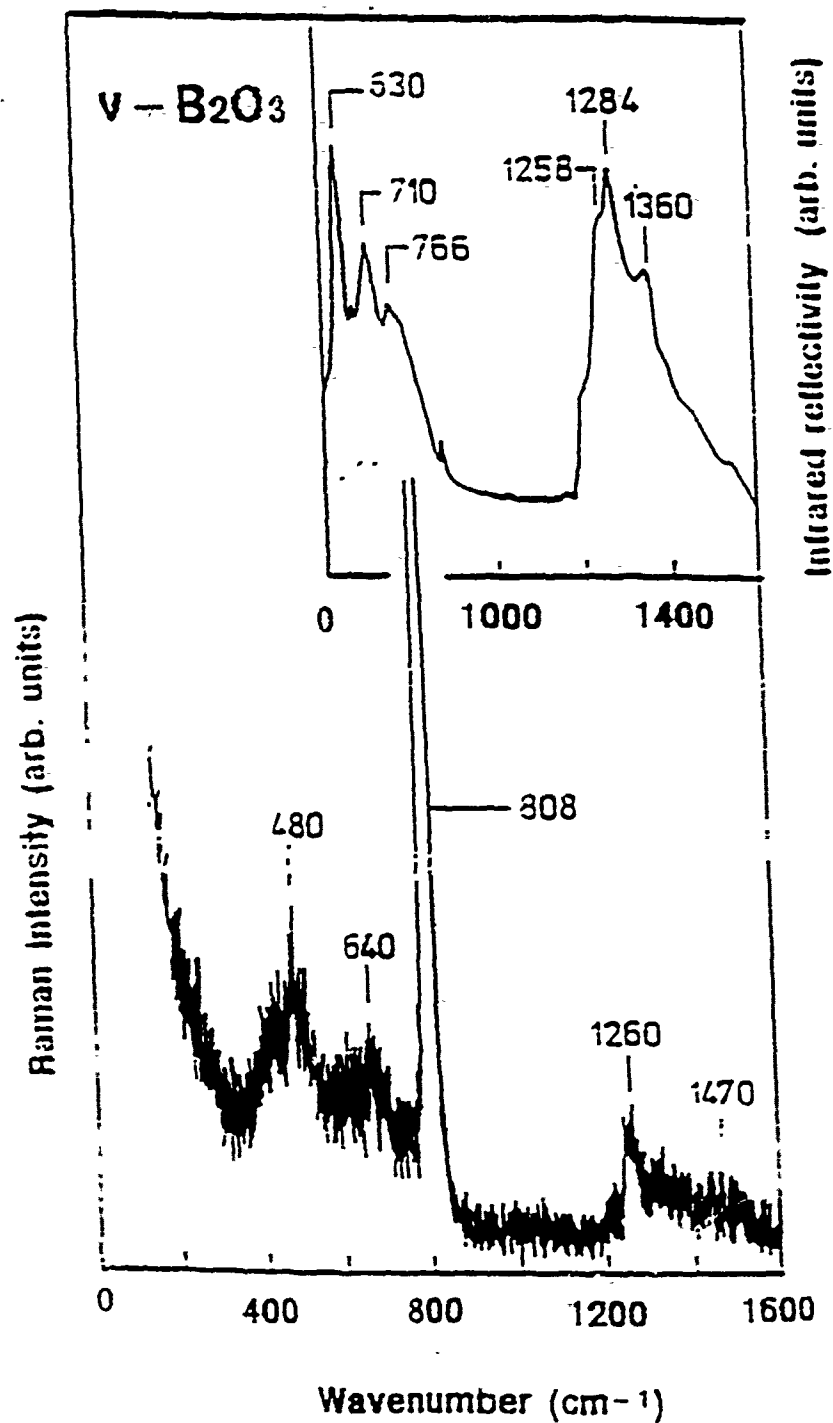


Fig. 1. Raman data and infrared data (inset) for pure  $\text{B}_2\text{O}_3$ . The sharp peak at  $808 \text{ cm}^{-1}$  is attributed to the breathing mode of the six-membered boroxol ring,  $\nu_2$ , in Fig. 2.

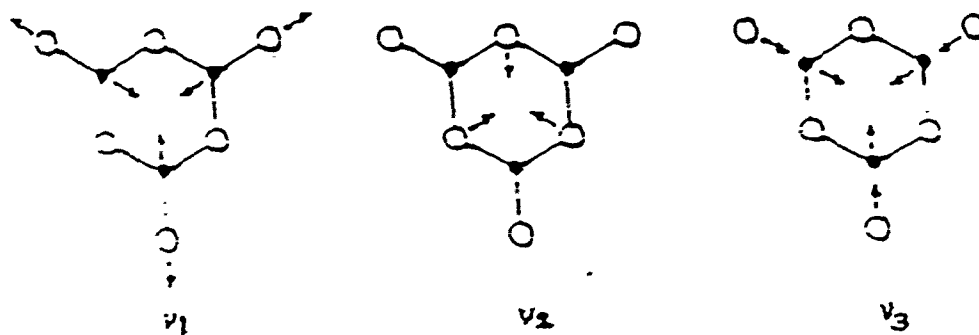


Fig. 2. The three symmetrical vibrations of the boroxol rings

attached to the outer oxygen atoms and found that the mode at  $800\text{ cm}^{-1}$  does not vary much when the mass is changed. Galeener et al. [11] explain the decoupling of rings from the rest of the network by a somewhat fortuitous cancellation of central and noncentral forces.

Galeener and Thorpe [12] have also discussed the introduction of 6-fold boroxol rings into a continuous random network model of  $\nu\text{-B}_2\text{O}_3$ . They conclude that the  $800\text{ cm}^{-1}$  mode consists of a breathing motion of the intra-ring oxygen, and therefore does not couple to the outside network.

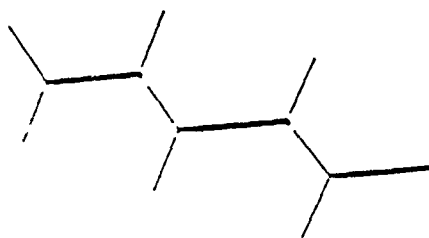
Kanehisa and Elliott [13] have demonstrated this decoupling explicitly using a cluster Bethe-lattice approximation as outlined in the following section.

#### 2.1. The Bethe lattice approximation

M. A. Kanehisa and R. J. Elliott [13] have used an extension of the Bethe lattice approximation to calculate a partial vibrational density of states of the boroxol network. They show by explicit calculation that the  $800\text{ cm}^{-1}$  mode  $\nu_2$  of the boroxol group remains sharp even when an infinite network is formed. This calculation confirms the earlier assumption [4,5] that this mode involves mainly the "breathing" motion of oxygen atoms inside the ring while the boroxol-boroxol coupling on network formation involves mainly motion of the boron atoms and the external (binding) oxygen atoms.

Using the Bethe lattice approximation Kanehisa and Elliott were able to solve the equations of motion for an infinite system having definite local symmetry without long-range order. The Bethe lattice considered is pictured in Fig. 3. The mathematical details and the methods used to treat a boroxol unit embedded in

(a)



(b)

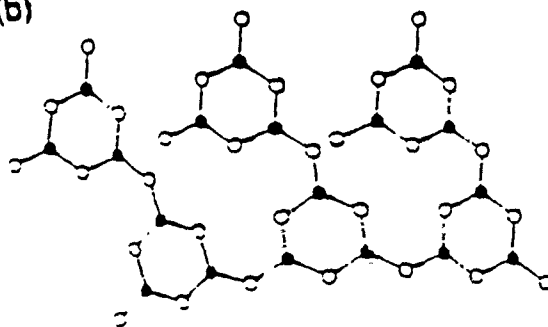


Fig. 3. (a) Generic threefold Bethe lattice; (b) boron oxide glass modelled as a Bethe lattice of boroxol units with bridging oxygen atoms.

the Bethe lattice are published elsewhere [13].

The vibrational spectrum of an isolated boroxol molecule is calculated first. By adjusting the  $\nu_2$  mode frequency for the isolated boroxol molecule to the experimental value of  $800\text{ cm}^{-1}$ , the force constant  $\alpha$  is determined to be  $9.4 \times 10^5\text{ dyn cm}^{-1}$ . The vibrational density of states calculated for the network is shown in Fig. 4. A width  $\gamma$  of  $100\text{ cm}^{-1}$  is added in order to account for the bond angle fluctuation around the ideal values. The calculated vibrational density of states spectrum compares reasonably well with the experimental Raman spectrum, shown in Fig. 1. There is a gap at  $1200\text{--}1500\text{ cm}^{-1}$  separating the low and high frequency bands in the calculated spectrum as in the experimental spectrum. The higher frequency bands are mainly due to boron atom motion while those below the gap are due mainly to oxygen atom motion. The most remarkable feature in this calculation is the fact that the  $\nu_2$  mode at  $800\text{ cm}^{-1}$ , remains sharp without any significant broadening on network formation. This is probably the first explicit demonstration of the vibrational decoupling of a molecular mode from the rest of the network.

### 3. Effect of the addition of modifier $\text{Li}_2\text{O}$ to $\text{v-B}_2\text{O}_3$ : The system

#### $\text{B}_2\text{O}_3\text{-xLi}_2\text{O}$

##### 3.1. Experimental results

The Raman spectra of the binary glass  $\text{B}_2\text{O}_3\text{-xLi}_2\text{O}$  are shown in Fig. 5. At low  $\text{Li}_2\text{O}$  concentration,  $x = 0.1$ , the  $800\text{ cm}^{-1}$  band corresponding to the breathing oxygen motion in the boroxol ring, the  $\nu_2$  mode trigonal deformation of the ring shown in Fig. 2, is still narrow and strong. A new band appears at  $780\text{ cm}^{-1}$  which corresponds to the trigonal deformation of six-membered borate

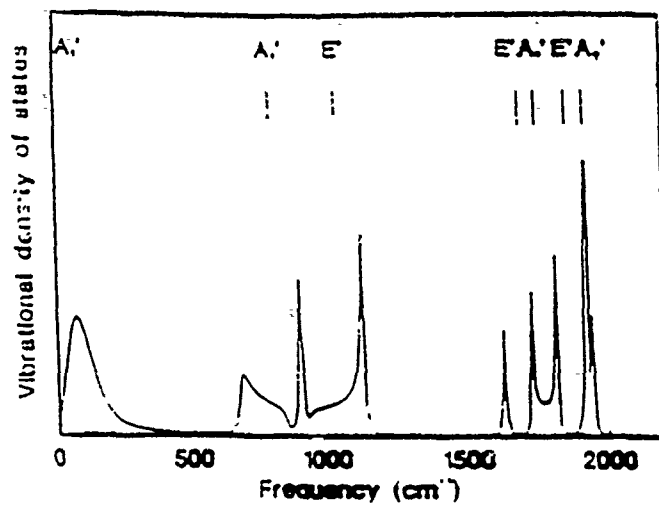


Fig. 4. Vibrational density of states of the boroxol network due to the internal oxygen atoms.

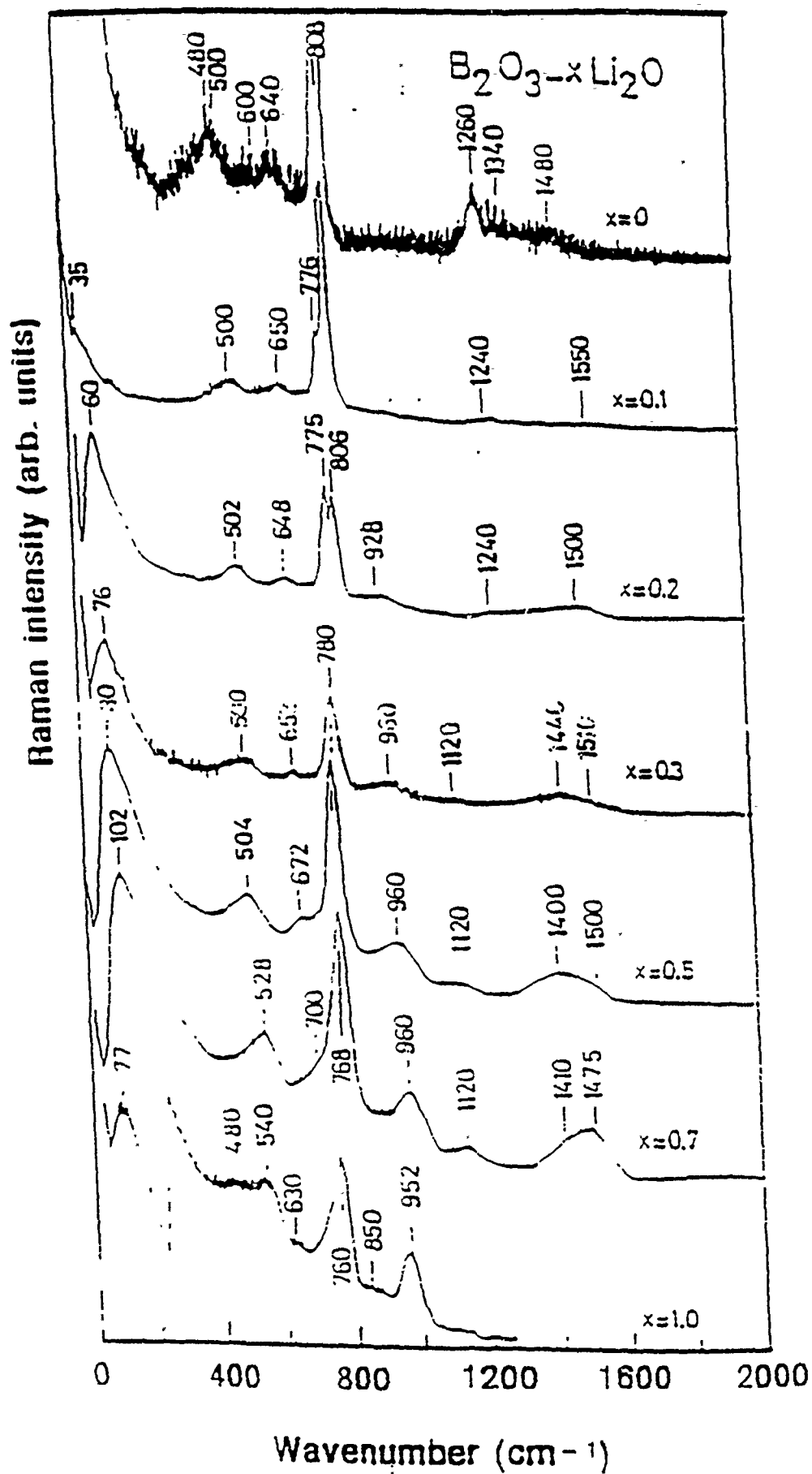
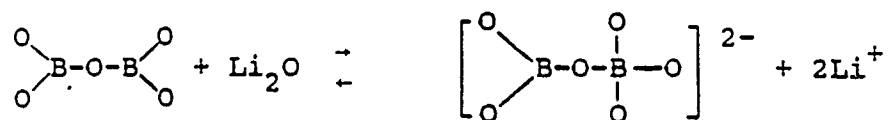


Fig. 5. Raman spectra of the binary glass system  $B_2O_3-xLi_2O$ .

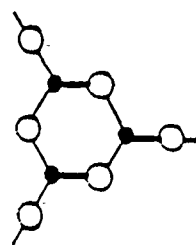
rings with one or two  $\text{BO}_4$  units [2] as shown in Fig. 6 for the tetraborate, triborate or diborate configuration. The band at  $500\text{ cm}^{-1}$  corresponds to the breathing mode  $\nu_3$  (Fig. 2) where the boron and the bridging oxygen atoms move in phase. The mode  $\nu_1$ , at  $1240\text{ cm}^{-1}$ , is associated with the symmetric vibration of the same atoms. The band between  $1400$  and  $1550\text{ cm}^{-1}$  is associated with the stretching vibrations of the B-O bonds in  $\text{BO}_3$  units. The three regions associated with the stretching vibrations of the B-O bonds which link the boron-oxygen network will be modified upon addition of  $\text{Li}_2\text{O}$ , which leads to the transformation of trihedrally coordinated boron,  $\text{B}^{\text{III}}$ , to tetrahedrally coordinated boron,  $\text{B}^{\text{IV}}$ , according to the reaction



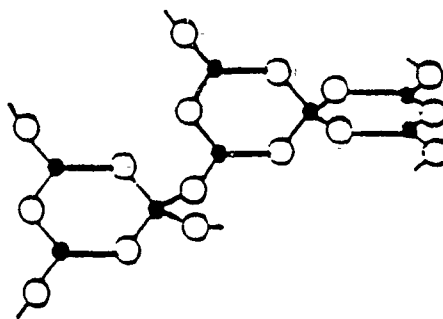
For low  $\text{Li}_2\text{O}$  concentration, the abundance of  $\text{B}^{\text{IV}}$  increases, (with increasing modifier concentration); as a consequence, the intensity of the line at  $780\text{ cm}^{-1}$  increases while that at  $806\text{ cm}^{-1}$  decreases and finally vanishes at  $x = 0.3$ . For  $x$  larger than  $0.5$ , the frequency of the  $\text{B}^{\text{IV}}$  band decreases until it reaches  $760\text{ cm}^{-1}$  in the metaborate glass  $x = 1.0$ .

At high  $\text{Li}_2\text{O}$  concentration ( $x > 0.5$ ), the formation of non-bridging oxygen atoms is inferred from the relative intensity increase of the two bands at  $960$  and  $1480\text{ cm}^{-1}$ .

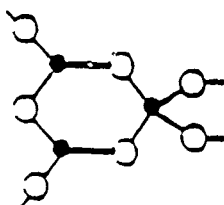
Two stages of modification can be distinguished when the concentration of the modifier increases. During the first stage, the tetrahedrally coordinated boron units increase and lead to an



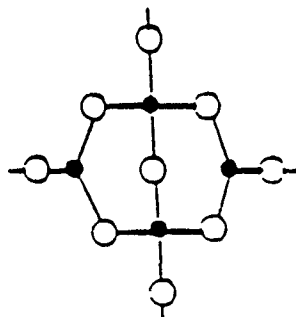
Boroxol



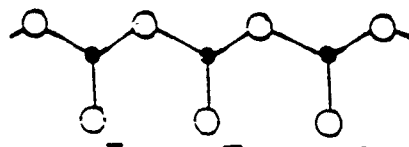
Tetraborate



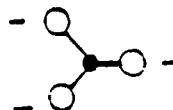
Triborate



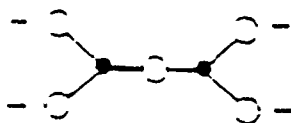
Diborate



Metaborate



Orthoborate



Pyroborate

● Boron atoms

○ Oxygen atoms

The oxygen atoms labeled — are non-bridging oxygen atoms (NBO).

Fig. 6. Some typical borate groups.

increase of the linkage of the boron-oxygen network up to  $x = 0.5$ . Above this concentration, formation of  $\text{BO}_3$  units with nonbridging oxygen atoms "opens" the borate units and consequently the degree of linkage of the network is decreased.

### 3.2 Theory

With the vibrational frequencies of groups of atoms in a given configuration deduced from spectroscopy data, it is of interest to calculate the vibrational spectrum with some specific short-range configuration. Toward this end, we have employed the network-dynamics theory and lattice dynamics in order to effect an indirect determination of the glass structure. Central force network-dynamics seems an ideal method to investigate the relation between local environmental changes and the modes of vibrations, since the short range order can be easily modified.

### 3.3. Methods of Calculation

#### 3.3.1. Network dynamics

The network-dynamics method, introduced by Sen and Thorpe [14], considers only nearest-neighbor central forces in the continuous random network under consideration; the other forces, for example, long-range Coulomb and angle bending forces, are much smaller in many cases. This approximation might be expected to hold particularly well in the optical frequency range with which we will be concerned.

Thorpe and Galeener [15] have put the central-force model of Sen and Thorpe in a more general framework using a Lagrangian formulation.

In the above-mentioned formulation, the bond directions at each atom are used to define a local coordinate system. The labels,  $l$ ,  $l'$ , etc., denote the sites, or atoms, in the network

and  $\Delta, \Delta',$  etc., denote the bonds or directions at each site. The displacement of the  $\ell^{\text{th}}$  atom along the  $\Delta^{\text{th}}$  bond is written as  $q_{\Delta}(\ell)$ . With this notation,  $q_{\Delta}(\ell), q_{\Delta'}(\ell)$  refer to displacements at the same site, but in different directions, and  $q_{\Delta}(\ell), q_{\Delta}(\ell')$  refer to displacements of two nearest neighbors along the bond joining them. In this case, the potential energy of the network takes a particularly simple form:

$$V = \frac{\alpha}{2} \sum_{(\ell, \ell', \Delta)} [q_{\Delta}(\ell) + q_{\Delta}(\ell')]^2, \quad (3.1)$$

where  $\alpha$  is the nearest-neighbor force constant. The angular brackets under the summation indicate that each bond is to be counted only once.

In the case of fourfold-coordinated (or planar threefold-coordinated) atoms, the  $q_{\Delta}(\ell)$  form an overcomplete set, so a constraint must be built into the the Lagrangian to ensure that  $\sum_{\Delta} q_{\Delta}(\ell) = 0$  for each atom  $\ell$ . One can accomplish this by adding to the potential a term

$$\frac{\lambda}{2} \sum_{\ell} \left[ \sum_{\Delta} q_{\Delta}(\ell) \right]^2 \quad (3.2)$$

and then taking the limit  $\lambda \rightarrow \infty$  at the end of the calculation to ensure that all solutions are consistent with the constraint  $\sum_{\Delta} q_{\Delta}(\ell) = 0$ .

The expression for the kinetic energies depends on the particular local environment of the atom, i.e., whether it has two, three, or four nearest neighbors. To find this expression, we consider the transformation between a fixed  $x, y, z$  coordinate system and the local bond direction coordinate system as shown in Fig. 7. With these expressions in hand, it is straightforward to generate the Lagrangian for any particular network under consideration,

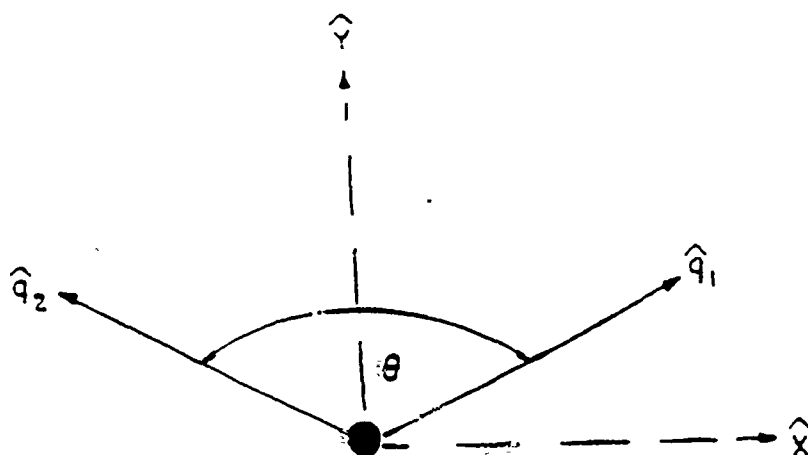


Fig. 7. Possible coordinate system for a twofold-coordinated atom. The  $\hat{q}$ -axes define the local bond directions,  $\theta$  is the bridging angle. The  $\hat{y}$ -axis bisects the angle between the  $\hat{q}$  axes.

$$L(\{q_i, \dot{q}_i\}) = T(\{\dot{q}_i\}) - V(\{q_i\}) , \quad (3.5)$$

where the curly braces,  $\{\dots\}$ , indicate the set of  $q_i$  for all atoms  $i$ . The equations of motion are then given by

$$\frac{d}{dt} \frac{\partial L}{\partial \dot{q}_i} - \frac{\partial L}{\partial q_i} = 0 .$$

As discussed in the previous section, we have seen that the addition of  $\text{Li}_2\text{O}$  to  $\text{B}_2\text{O}_3$  is accompanied by the appearance of groups containing fourfold-coordinated borons. In addition, the concentration of these structures increases proportionally with the concentration of the modifier  $\text{Li}_2\text{O}$  up to a critical value  $x_c$ . We shall consider a network containing both threefold- and fourfold-coordinated borons. Indeed, for the composition  $\text{B}_2\text{O}_3\text{-}0.5\text{Li}_2\text{O}$ , one can envision a network of equal numbers of threefold- and fourfold-coordinated borons. Here we consider one such network, with each threefold-coordinated boron surrounded by fourfold-coordinated borons and vice versa. shown in Fig. 8

Using the results from the last section for twofold-, threefold- and fourfold-coordinated atoms, the Lagrangian for the network drawn in Fig. 8 takes the form

$$L = \frac{3m}{8} \sum_{\ell, \Delta} [\dot{q}_\Delta(\ell)]^2 + \frac{M}{2} \sum_{\ell} \left[ \sum_{\Delta} a \dot{x}_\Delta^2(\ell) + b \left( \sum_{\Delta} \dot{x}_\Delta(\ell) \right)^2 \right] + \frac{m}{2} a' \sum_{\ell, \Delta} \dot{y}_\Delta^2(\ell) \\ - \frac{1}{2} \lambda \sum_{\ell} \left( \sum_{\Delta} q_\Delta(\ell) \right)^2 - \frac{1}{2} \lambda \sum_{\ell} \left( \sum_{\Delta} y_\Delta(\ell) \right)^2 \\ - \frac{\alpha}{2} \sum_{(\ell, \ell', \Delta)} [q_\Delta(\ell) + x_1(\ell')]^2 - \frac{\beta}{2} \sum_{(\ell, \ell', \Delta)} [y_\Delta(\ell) + x_2(\ell')]^2 ,$$

where  $a = (1 - \cos\theta)^{-1}$  ,  $a + 2b = (1 + \cos\theta)^{-1}$  , and

where we use  $q_\Delta(\ell)$  and force constant  $\alpha$  for the fourfold-coordinated borons,  $y_\Delta(\ell)$  and force constant  $\beta$  for the threefold-

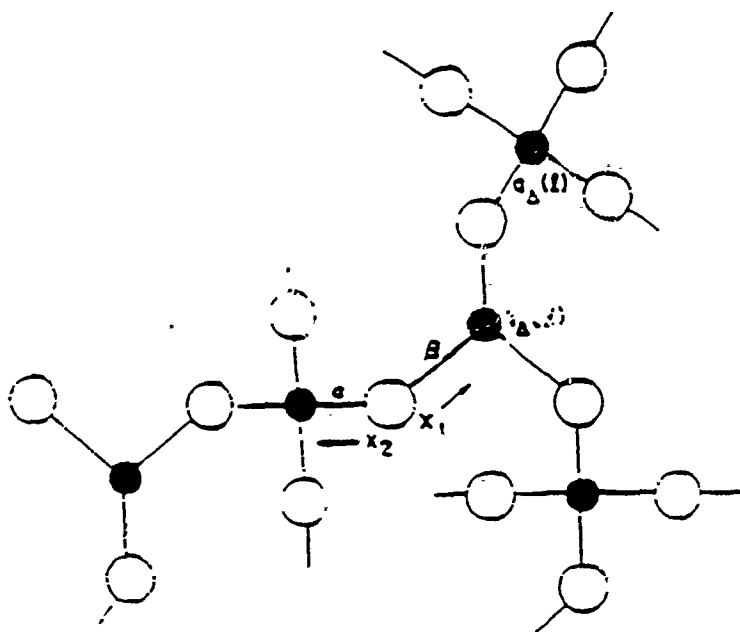


Fig. 3. Network considered as a possible structure of  $B_2O_3-0.5Li_2O$ .  $x_1$  is specified as being in the direction of the threefold-coordinated boron,  $\gamma_3(1)$ , and  $x_2$  toward the fourfold-coordinated boron,  $q_4(1)$ .  $\alpha$  = bond label and therefore direction. We take  $\alpha$  = force constant of fourfold-coordinated B-O bonds, and  $\beta$  that of threefold-coordinated B-O bonds.

coordinated borons,  $x_{1,2}(l)$  for the oxygen in the directions of  $q(l), y(l)$ , respectively, and again  $M_{\text{boron}} = m$ ,  $M_{\text{oxygen}} = M$ . The equations of motion and their solution are presented in a separate publication [16].

The central-force eigenfrequencies of the network are determined by the relation

$$12(\beta_1 - m\omega^2)(\alpha_1 - \frac{3}{4}\omega^2) = (\alpha'\epsilon)^2,$$

where we have defined the frequency-dependent force constants

$$\alpha' = \frac{M\omega^2 \alpha \beta \cos \theta}{(M\omega^2)^2 - (\alpha + \beta)M\omega^2 + \alpha \beta \sin^2 \theta},$$

$$\alpha_1 = \alpha + \frac{\alpha^2 (M\omega^2 - \beta \sin^2 \theta)}{(M\omega^2)^2 - (\alpha + \beta)M\omega^2 + \alpha \beta \sin^2 \theta},$$

$$\beta_1 = \beta + \frac{\beta^2 (M\omega^2 - \alpha \sin^2 \theta)}{(M\omega^2)^2 - (\alpha + \beta)M\omega^2 + \alpha \beta \sin^2 \theta}.$$

This equation determines the allowed central-force frequency bands as a function of the force constants  $\alpha$  and  $\beta$ , the masses, and the bridging angle  $\theta$ .

### 3.3.2. Lattice Dynamics

The lattice-dynamics calculations were carried out as an independent check on the network-dynamics results. As such, they were done in the nearest-neighbor central-force approximation.

No disagreement was found between the lattice-dynamics and network-dynamics calculations. The two methods are quite complementary in examining the effect of varying various parameters,

such as force constants, intermolecular bridging angles, or configurations on the vibrational spectrum of the solid.

### 3.4. Results and Discussion

When a modifier,  $\text{Li}_2\text{O}$  for example, is added to the glass former  $\text{B}_2\text{O}_3$ , the modes involving the B-O bonds which link the boron oxygen network are modified. This can be understood as being due to the transformation of threefold- to fourfold-coordinated boron.

As can be seen in the experimental data for  $\text{B}_2\text{O}_3\text{-}0.1\text{Li}_2\text{O}$  from Fig. 5, the vibrational spectra are significantly modified by the addition of lithium oxide [18]. A new band appears at  $776\text{ cm}^{-1}$  in the Raman spectrum, and a set of broad features moves up in the infrared spectrum, all due to the presence of  $\text{BO}_4^-$  groups. At the same time, the intensities of the  $808\text{-}$  and  $1260\text{-cm}^{-1}$  peaks in the Raman spectrum and the  $1360\text{-cm}^{-1}$  peak in the infrared spectrum are seen to decrease in intensity, relative to the other peaks, with increasing  $\text{Li}_2\text{O}$  concentration. The new bands observed in the infrared spectrum at  $800$  and  $1030\text{ cm}^{-1}$  are attributed to  $\text{BO}_4$  bond stretching in tetraborate groups [19].

In Fig. 9, the results of network- and lattice-dynamics calculations [16] are presented for  $\beta/\alpha = 0.8$ . Note that the general features in the spectra such as the narrowing of the middle frequency gap as compared to the data of pure  $\text{B}_2\text{O}_3$ , are found in the network-dynamics results. The widening of the high-frequency gap, presumably due to the difficulty of the modes associated with  $\text{BO}_3$  groups to hybridize with those of the stiffer  $\text{BO}_4$  groups, is also found.

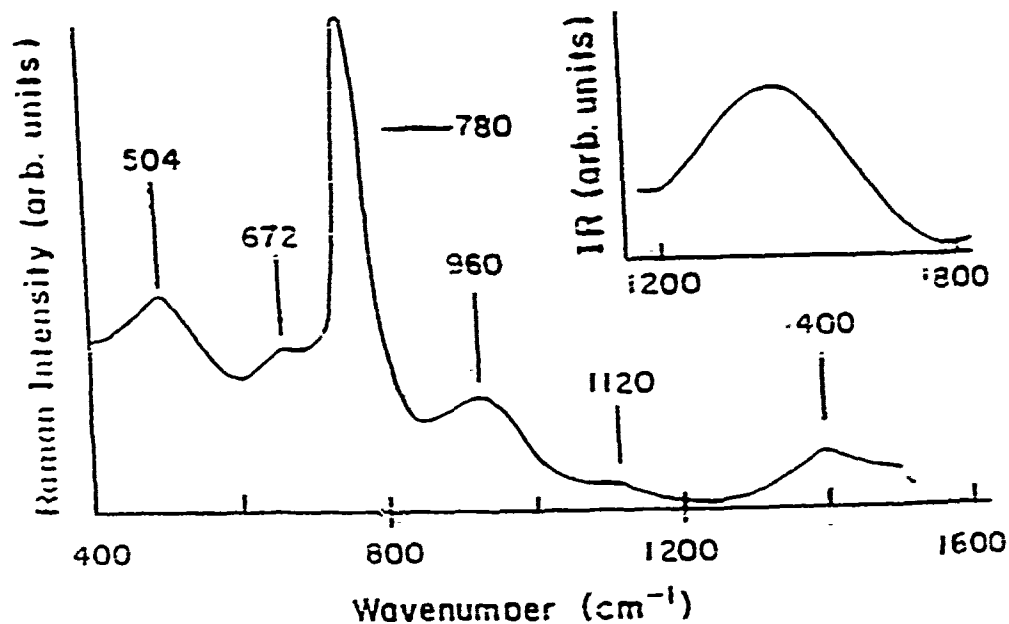
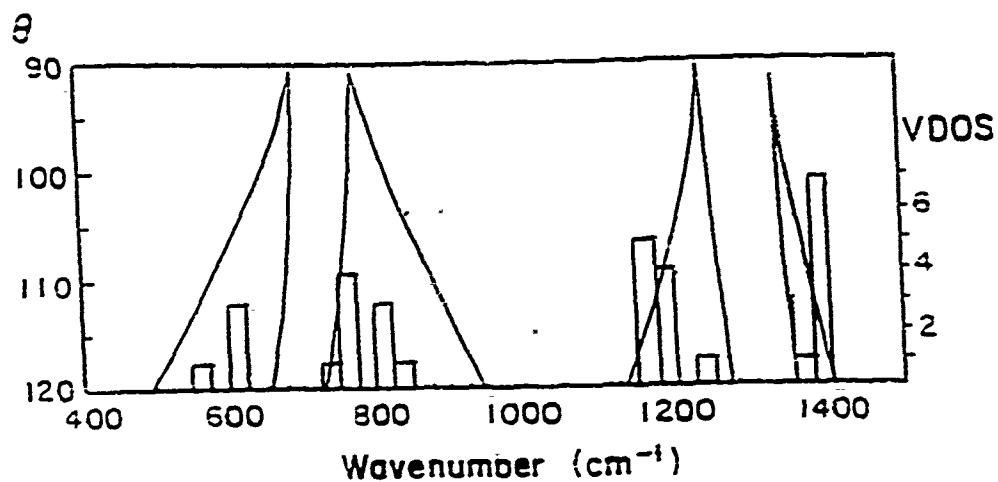


Fig. 9. Raman and infrared spectra, network dynamics and lattice dynamics results for  $B_2O_3-0.5Li_2O$ . The ratio of the force constants of *threefold*-coordinated B-O bonds to that of *fourfold*-coordinated B-O bonds is  $\beta/\alpha = 0.8$ . Histograms indicate the number of modes in the corresponding frequency band according to the lattice-dynamics calculation  $\theta = 120^\circ$ .

If we compare the results in Figs. 9 and 10 with the Raman spectra shown in Figs. 1 and 5, the agreement is quite striking. The results for  $\beta/\alpha = 0.9$  feature a large frequency gap which is in excellent agreement with the experimental data for  $x = 0$ . The  $\beta/\alpha = 0.8$  calculation results in more extended frequency bands which represents very closely the spectra displayed in Fig. 5 for  $B_2O_3-0.5Li_2O$ . The appearance of modes at 960 and 1120  $cm^{-1}$  in the formerly featureless mid-frequency band is "allowed" by the broadening of the bands predicted by the network-dynamics results. The peaks at 505 and 672  $cm^{-1}$  in the Raman spectra are basically unaffected by the addition of the modifier, and as expected the low- and high-frequency band edges of the first band are unchanged.

It is interesting to note that such simple calculations should yield results representing well the trends in the spectral distribution of different vibrational modes in the binary glass system as a function of modifier concentration. This result suggests that the force constants used are reasonable, and again underscores the importance of local order in understanding the vibrational response of covalently bonded glass.

#### 4. The Effect of Dopants

##### 4.1. Structural modifications induced by the Dopant

Two types of dopants which introduce additional free Li ions and increase the ionic conductivity of borate glasses are examined: the lithium halides  $LiX$  ( $X = F, Cl, Br, I$ ), and lithium sulfate  $Li_2SO_4$ . A general observation is that the dopants do not significantly modify the glass structure which simply localizes the anion leaving as the only mobile species the small lithium cation. The larger the anion, the stronger is its interaction with the host network.

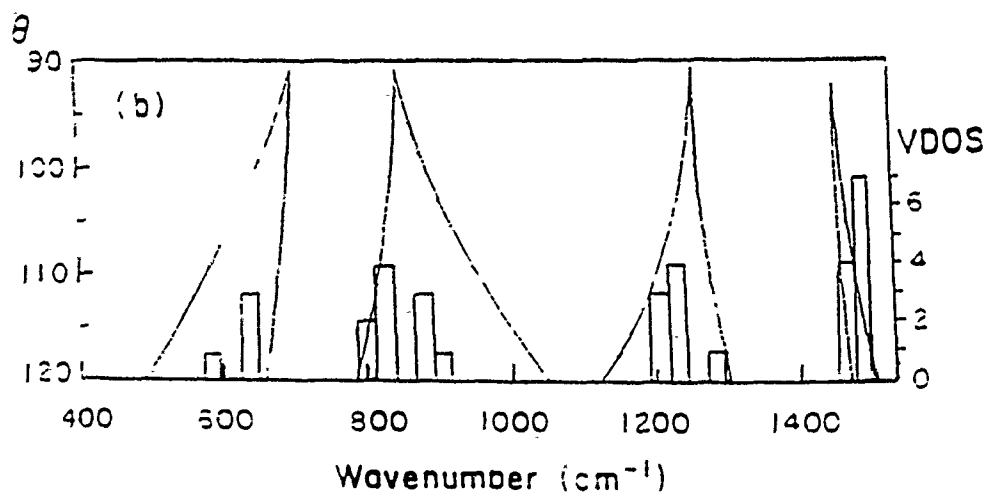
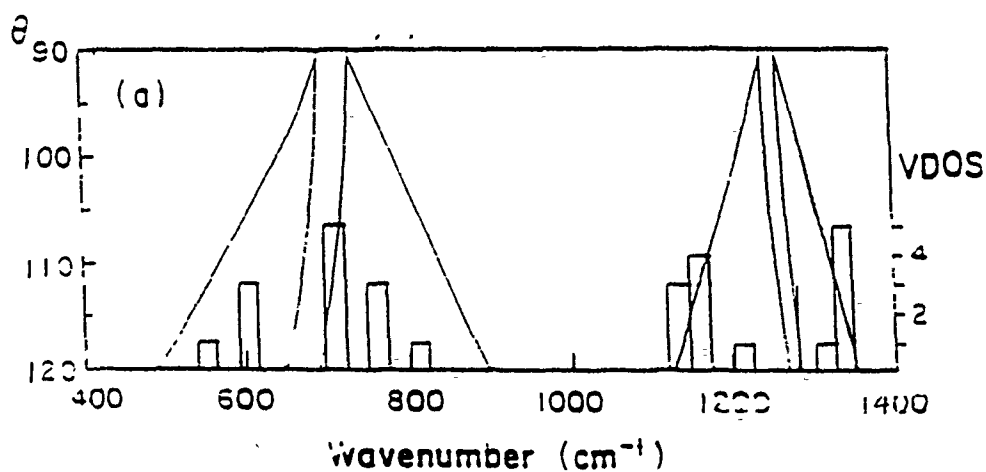


Fig. 10. Allowed frequency bands and histogram for  $B_2O_3-0.5Li_2O$  as a function of the intermolecular bridging angle  $\theta$  for  $\beta/\alpha = 0.9$ (a) and  $0.7$ (b). The histograms are for  $\theta = 120^\circ$ .

Raman and infrared spectra displayed in Figs. 11 and 12 show more pronounced changes in the spectra as one goes from F to Cl, Br, and finally I. The main effect is a decrease in the intensity of the peak at  $808\text{ cm}^{-1}$  measuring the relative abundance of trihedrally coordinated boron  $\text{B}^{\text{III}}$  atoms and an increase of the peak at  $734\text{ cm}^{-1}$  characteristic of the vibration of tetrahedrally coordinated boron  $\text{B}^{\text{IV}}$ . Analysis of the shape of the  $\text{BO}_4$  bands,  $784\text{ cm}^{-1}$  in Raman scattering and  $850\text{--}1100\text{ cm}^{-1}$  in infrared reflectivity, points toward the redistribution of these units into the network. For glass doped with LiF they are included preferentially in tetraborate groups [21], and the fluorine anions participate in the network forming  $\text{BO}_3\text{F}$  and  $\text{BO}_2\text{F}_2$  units [22]. Chlorine, bromine and iodine anions enter the network in interstitial positions [18]. Introduction of the dopant salt results in the breaking of B-O-B links and the formation of  $\text{BO}_4$  units. Their distribution in the network is conditioned by electrostatic interactions between the negative anion and the  $\text{BO}_4$  units. Modification of the boron-oxygen network conformation results in a less linked network facilitating free ion diffusion.

In the ternary glass  $\text{B}_2\text{O}_3\text{--}0.57\text{Li}_2\text{O--}\gamma\text{LiX}$ , in which the modifier concentration is such that the glass does not contain boroxol rings, the modification due to the introduction of dopant salts is characterized in the Raman spectrum by the appearance of a shoulder at about  $720\text{ cm}^{-1}$  on the  $770\text{ cm}^{-1}$  band due to the vibration of four-coordinated boron atoms. For a given halide anion this new line shifts toward lower frequencies and its intensity increases with increasing dopant salt concentration,  $\gamma$ , as shown in Figure 13. At the same time the frequency of the band at  $520\text{ cm}^{-1}$  due to

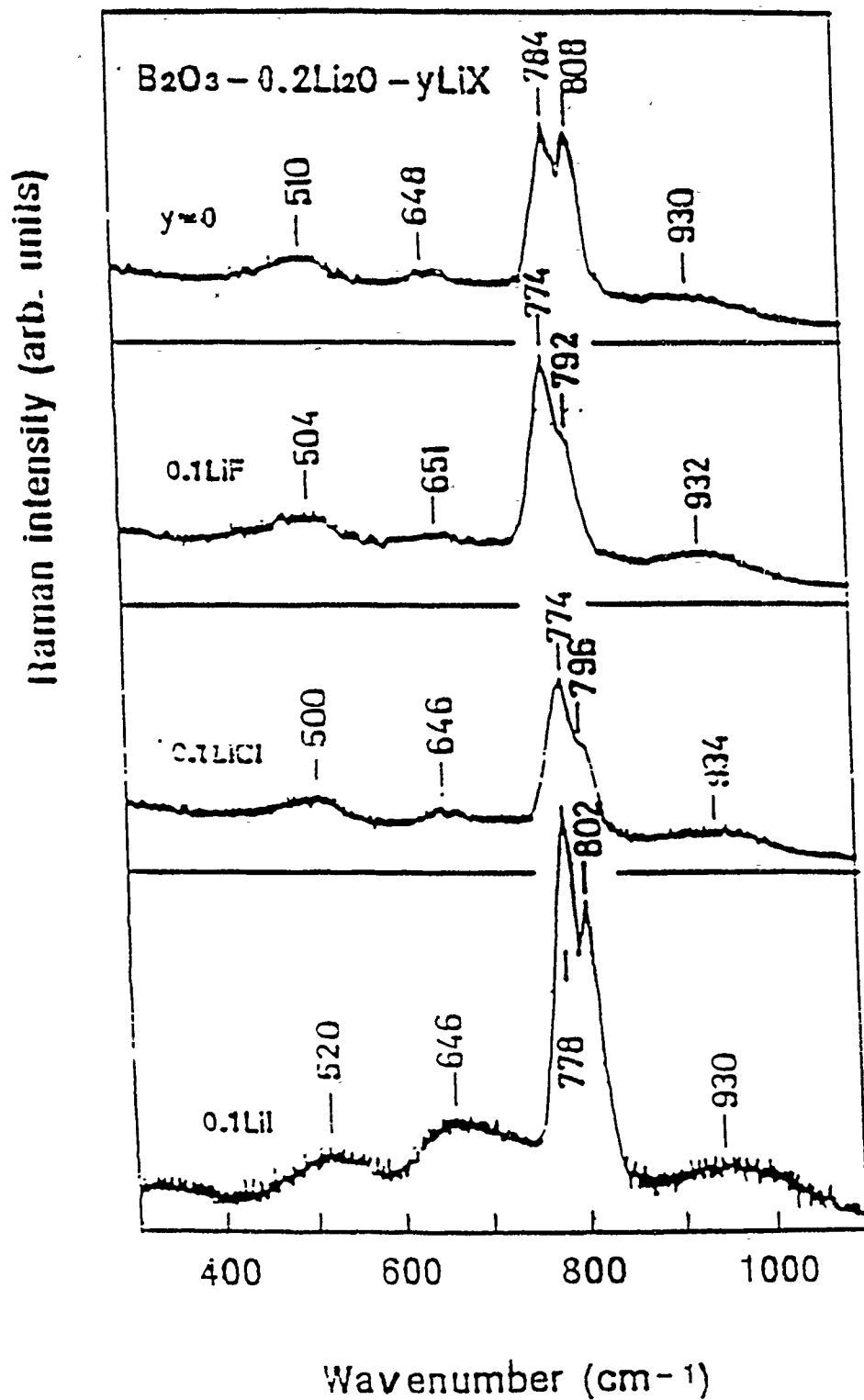


Fig. 11. Raman spectra of the ternary halogenoborate glasses  $B_2O_3 - 0.2Li_2O - yLiX$ .

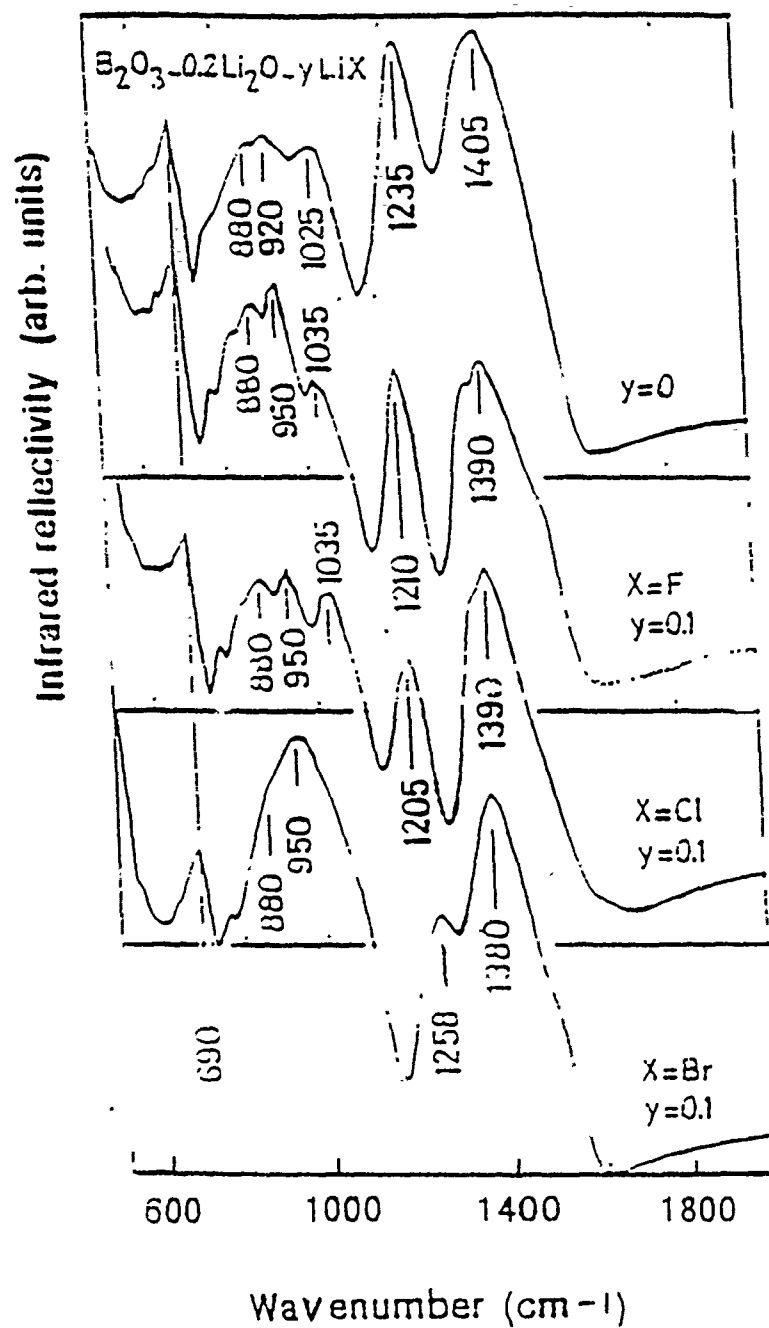


Fig. 12. Mid-infrared reflectivity of the ternary halogenoborate glasses  $\text{B}_2\text{O}_3-0.2\text{Li}_2\text{O}-y\text{LiX}$ .

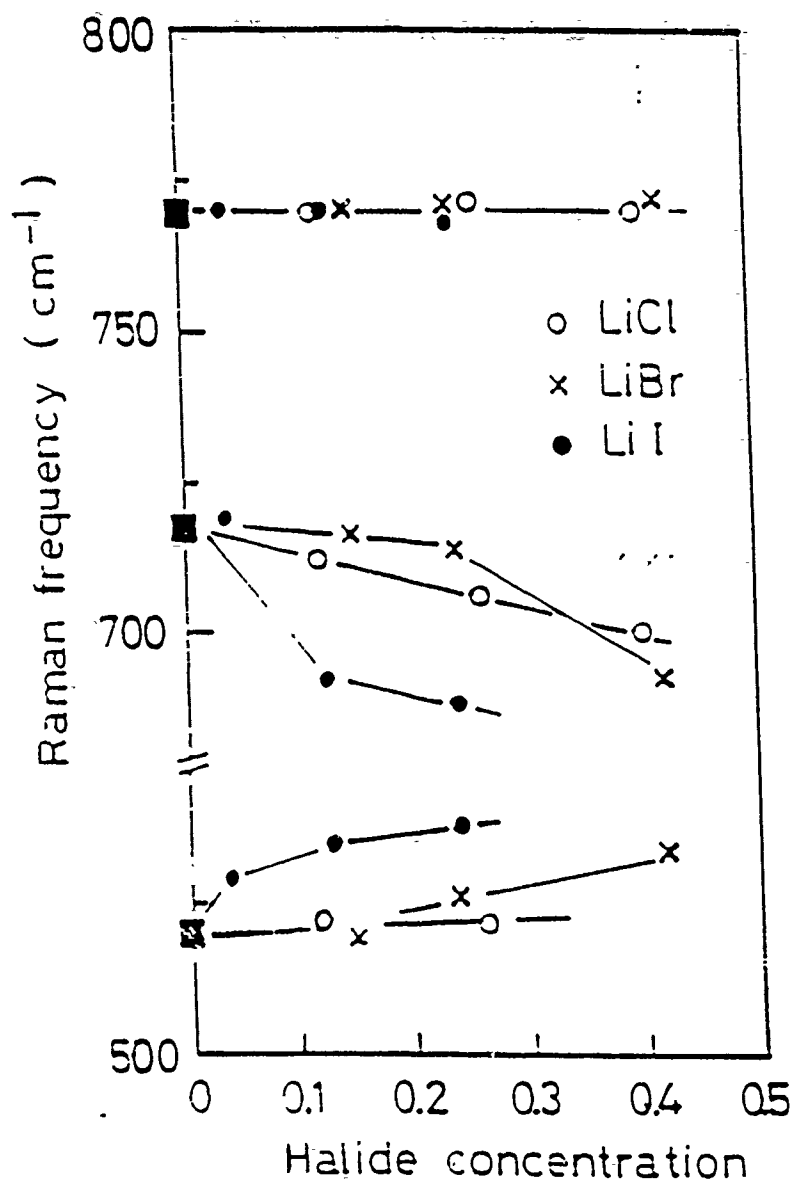


Fig. 13. The shift of the Raman frequencies versus the halide concentration.

the in-phase motion of the bridging oxygen and the boron atom increases. The stiffening of this mode, which is higher the larger the anion size, corresponds to a compression of the B-O-B band.

There is also an increase of intensity of the bands at 960 and  $1480\text{ cm}^{-1}$  attributed to the vibrations of groups with non-bridging oxygen atoms. Sharpening of these bands and a shift toward higher frequencies is observed when going from LiCl to LiI with the same concentration.

Infrared reflectivity data corroborate the general findings from Raman scattering as to the effect of the addition of a dopant salt to the borate glass. A new reflectivity band appears at  $1245\text{ cm}^{-1}$  when a dopant is added, as seen in Figure 14, which shifts toward lower frequencies when changing the dopant salt from LiF ( $1245\text{ cm}^{-1}$ ) to LiI ( $1220\text{ cm}^{-1}$ ). This is consistent with the formation of  $\text{BO}_3$  units with nonbridging oxygen atoms. This result points toward a decrease of the linkage of the network. When a doping salt is added, the network is expanded. The  $\text{BO}_4$  groups are transformed into  $\text{BO}_3$  triangles and  $\text{BO}_3$  with nonbridging oxygen atoms which can be connected into chains, a configuration which is consistent with the softening of the mode and which is favored when the size of the anion is increased.

These modifications of the boron-oxygen network of the ternary glasses have shown that in all the cases the lithium halide addition results in an expansion of the network, the effect being most pronounced with LiI. These results agree with density and glass transition temperature measurements.

These observations are of prime importance for the understanding of the ion transport properties of the borate glasses.

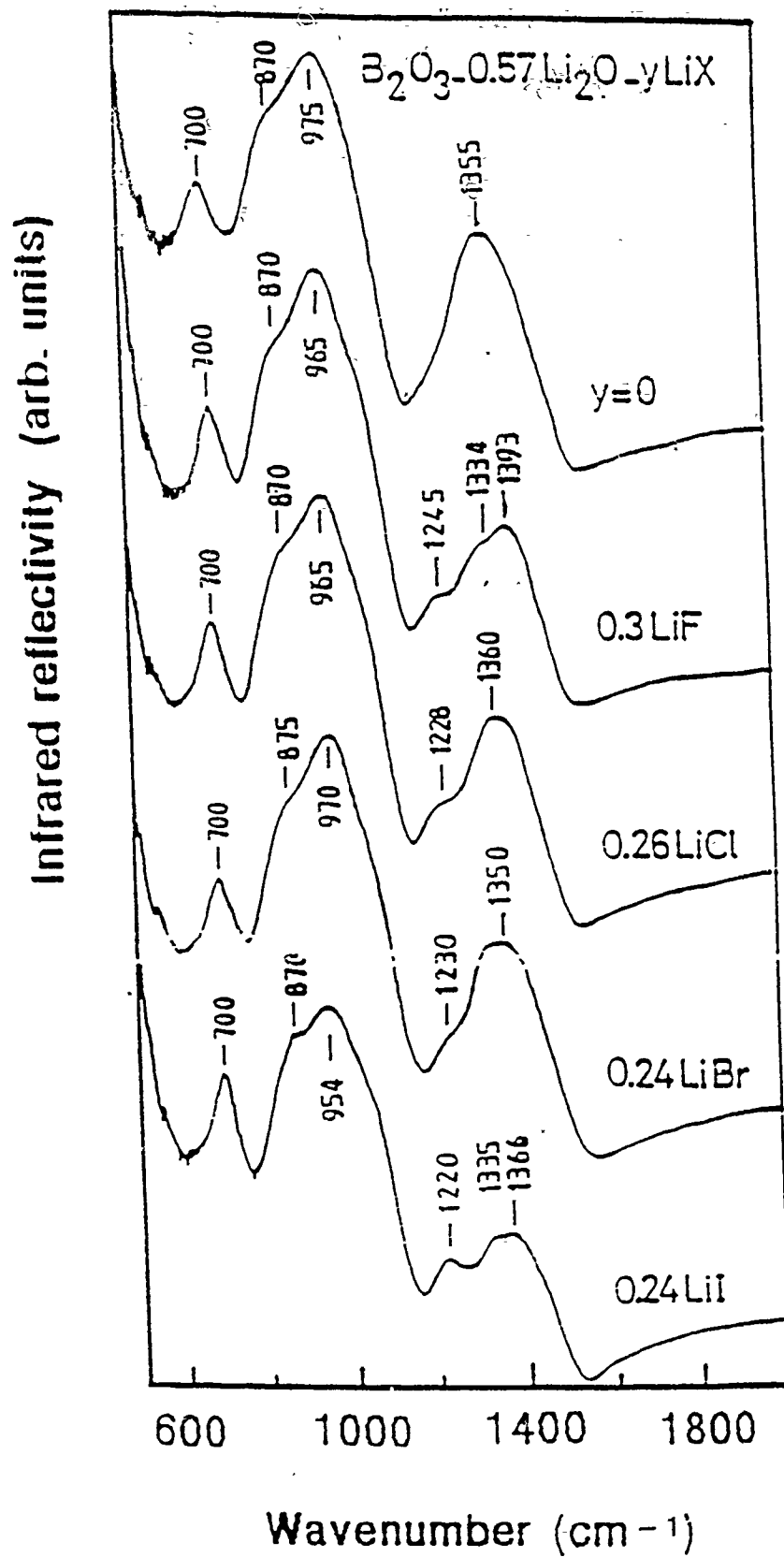


Fig. 14. Mid-infrared reflectivity of the ternary halogeno-borate glasses  $B_2O_3-0.57Li_2O-LiX$ .

The  $\text{BO}_4$  groups may be considered as negative ions with a large ionic radius which provide binding sites with small binding energy for the mobile lithium ions. At low modifier content the increase of ionic conductivity comes from the increase of the number of  $\text{BO}_4$  units and of the number of free lithium ions. But for higher oxide content there is competition between two competing mechanisms: an increase in the number of free lithium ions provided by the dissociation of the dopant salt and conversion of the  $\text{BO}_4$  units into  $\text{BO}_3$  units with nonbridging negatively charged oxygen atoms which trap the lithium ions. In the range of large  $\text{Li}_2\text{O}$  modifier content the conductivity is less sensitive to the addition of the doping salt.

#### 4.2. Effect of the dopant $\text{Li}_2\text{SO}_4$ : $\text{B}_2\text{O}_3\text{-xLi}_2\text{O-yLi}_2\text{SO}_4$

Comparison of the Raman scattering spectra of the binary  $\text{B}_2\text{O}_3\text{-0.7Li}_2\text{O}$  and ternary  $\text{B}_2\text{O}_3\text{-0.7Li}_2\text{O-0.42Li}_2\text{SO}_4$  systems, displayed in Figure 15, shows that the spectrum of the  $\text{Li}_2\text{SO}_4$  doped glass consists of the superposition of the spectra of  $\text{B}_2\text{O}_3\text{-0.7Li}_2\text{O}$  and  $\text{Li}_2\text{SO}_4$ . The peaks appearing at 456, 644, 1004 and  $1100\text{ cm}^{-1}$  correspond respectively to  $\nu_2$ ,  $\nu_4$ ,  $\nu_1$  and  $\nu_3$  vibrations of the sulfate ion [23].

Analysis of the infrared reflectivity spectra presented in Figure 16 reveals the disappearance of the band at  $1235\text{ cm}^{-1}$  due to rotations in the trigonal  $\text{BO}_3$  units with nonbridging oxygen atoms. Sulfate addition transforms these groups into  $\text{BO}_4$  units included in the tetraborate or diborate groups [24]. Formation of diborate groups preferentially indicates that there is an expansion of the network to accommodate the sulfate ions with a decrease of the degree of linkage of the network.

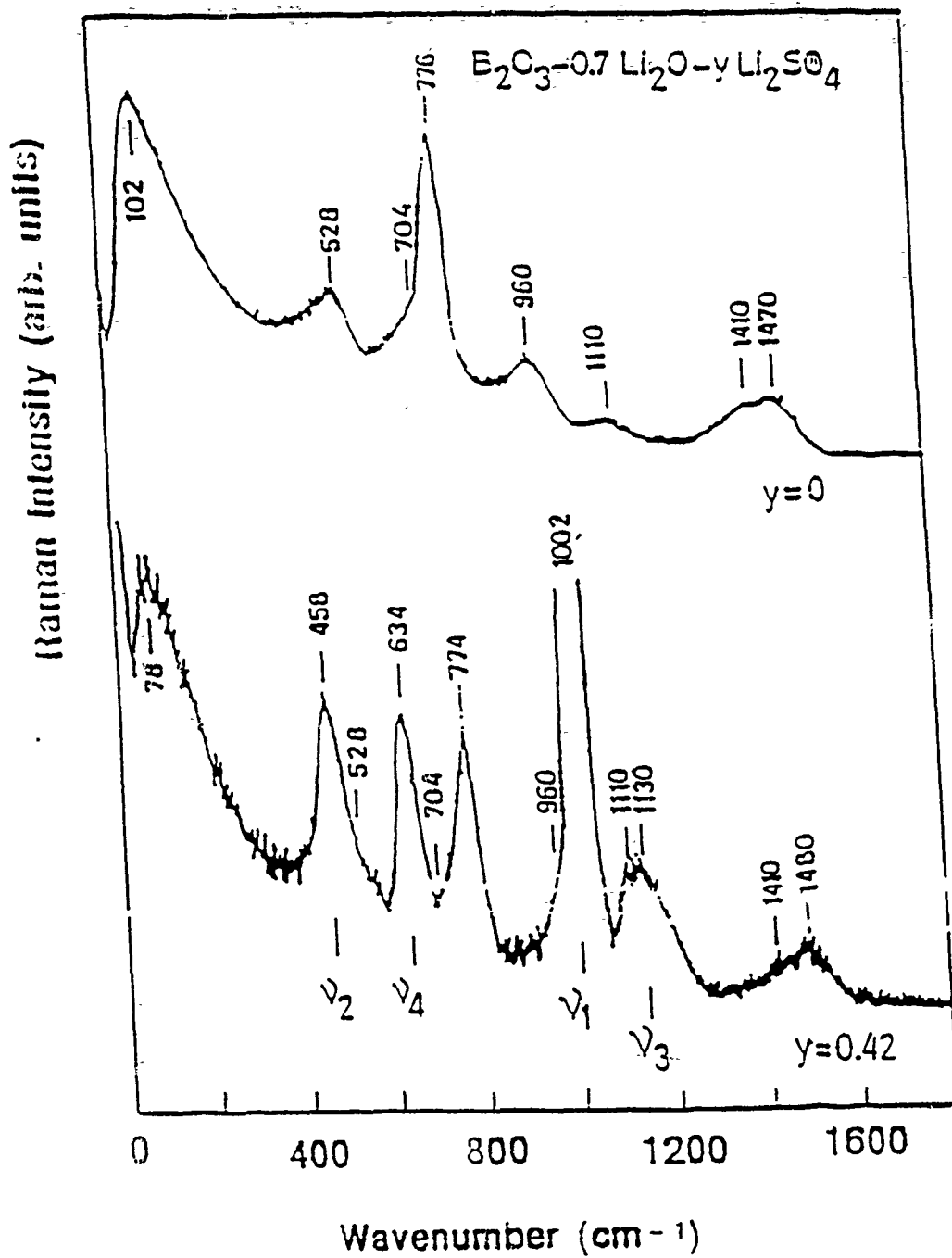


Fig. 15. Raman spectra of the ternary sulfoborate glasses  $\text{E}_2\text{O}_3-0.7\text{Li}_2\text{O}-y\text{Li}_2\text{SO}_4$  versus the lithium sulfate content.

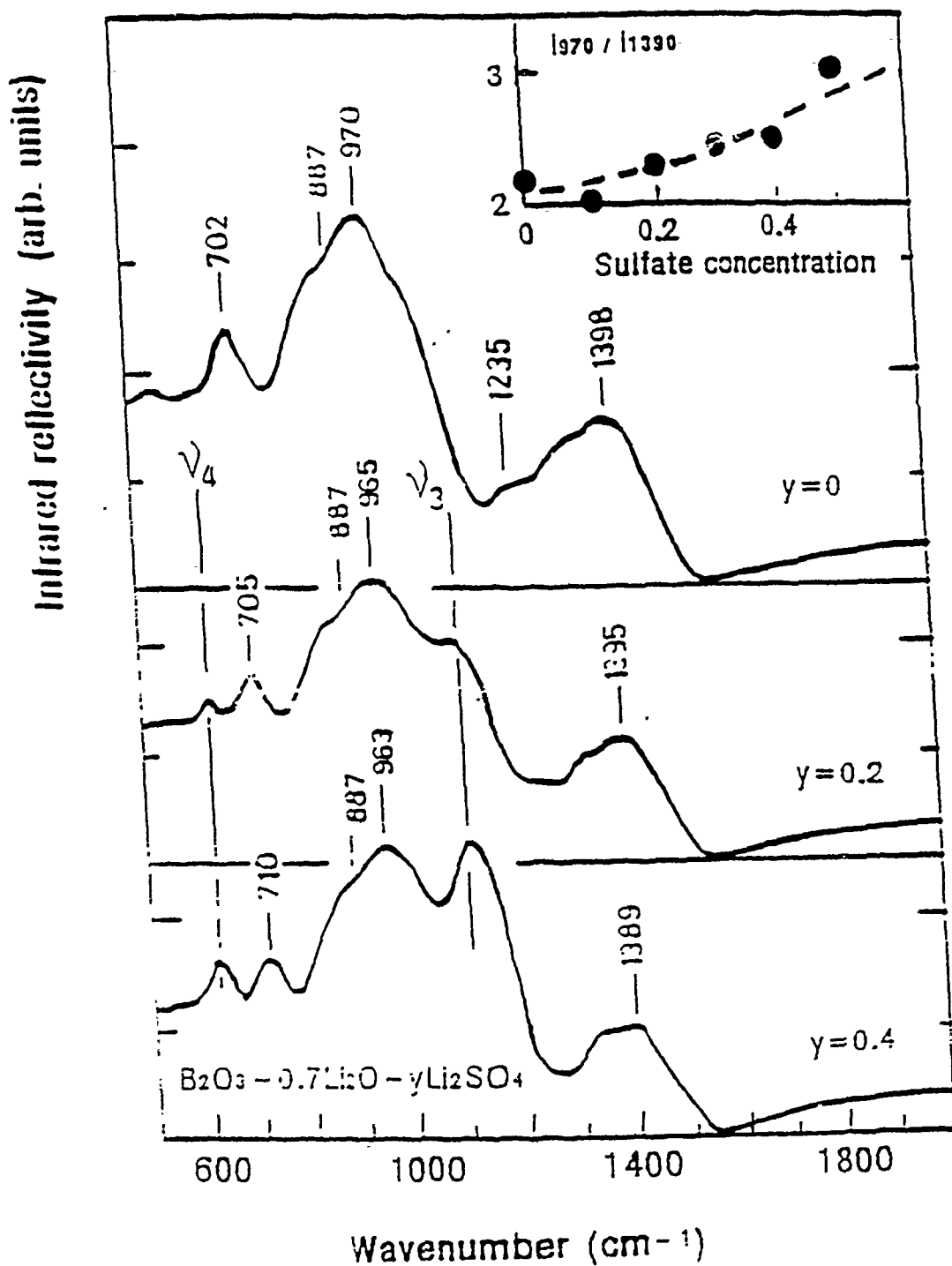


Fig. 16. Mid-infrared reflectivity of the ternary sulfo-borate glasses  $B_2O_3-0.7Li_2O-yLi_2SO_4$  versus the lithium sulfate content. The curve included in the inset shows the variation of the ratio of the intensity of the  $BO_4$  band to that of the  $SO_3$  band with sulfate concentration.

## 5. Ion conduction in lithium borate glasses.

### 5.1. Introduction

We have seen in the previous chapter that in this superionic conductor the dopant salt  $\text{LiCl}$  or  $\text{Li}_2\text{SO}_4$  is dissolved in a solid matrix consisting of the lithium borate glass  $\text{B}_2\text{O}_3\text{-xLi}_2\text{O}$ . The salt dissociates giving  $\text{Li}^+$  ions and  $\text{Cl}^-$  or  $\text{LiSO}_4^-$  and  $\text{SO}_4^{2-}$  ions. The  $\text{Li}^+$  ions are highly mobile and significantly increase the electrical conductivity of the system. The situation is quite analogous to the electrolytic solution where a salt is dissolved in a liquid solvent such as water. There is one significant difference, however, and that is that water has a dielectric constant of about 80 whereas borate glasses have a dielectric constant of about 8. This means that at room temperature a typical salt such as  $\text{LiCl}$  will be nearly fully dissociated in aqueous solution but will be only weakly dissociated in the borate glass. Furthermore, in the latter case, the concentration of lithium ions will increase rapidly as the temperature is increased above room temperature. Consequently, the electrical conductivity of the doped borate glasses should increase rapidly with increasing temperature as is well demonstrated experimentally.

The electrical properties of these glasses have been studied by the method of complex impedance in the range from 20 Hz to 1 MHz at temperatures ranging between 20 and  $400^\circ\text{C}$ . The activation energy  $E_a$  was calculated from the conductivity  $\sigma$  according to the formula

$$\sigma = \sigma_0 \exp \left( - \frac{E_a}{k_B T} \right)$$

The values obtained lie in the range 0.46-0.72 eV. At low concentrations  $x$  and  $y$ , the value of the activation energy decreases rapidly as either concentration is increased but changes only slowly at high concentrations.

### 5.2. Calculation of mobile $\text{Li}^+$ ion concentration [25]

The system that we are considering can be compared with that of an alkali halide such as NaCl doped with  $\text{CaCl}_2$  or  $\text{CdCl}_2$ , which has been discussed previously [26]. The  $\text{Ca}^{2+}$  or  $\text{Cd}^{2+}$  ions substitute for  $\text{Na}^+$  ions in the lattice and, to preserve electro-neutrality, positive ion vacancies must be introduced simultaneously with a concentration equal to that of  $\text{Ca}^{2+}$  or  $\text{Cd}^{2+}$ . Positive ion vacancies behave as negative charges which, when dissociated from the  $\text{Ca}^{2+}$  or  $\text{Cd}^{2+}$  ions, are mobile and can contribute to the electrical conductivity. The overall activation energy for the conductivity is the sum of a part connected with the dissociation of a positive ion vacancy from a divalent cation and another part connected with the diffusion of a positive ion vacancy under the influence of an applied electric field. In our system the mobile lithium ions are analogous to the positive ion vacancies. The concentration of lithium ions as a function of temperature and dopant concentration is calculated considering an ensemble of  $\text{Li}_2\text{SO}_4$  molecules dispersed in a borate glass that is assumed to be a continuous medium [25]. If the molecules are regarded as being isolated, and we assume that only one  $\text{Li}^+$  ion can be ionized per molecule (these assumptions being valid in the low concentration limit at temperatures which are not too high), the conductivity can be written as

$$\sigma = e \mu n_T^{1/2} \left\{ y n_\lambda \exp\left(-\frac{2E_{ad}}{k_B T}\right) + x n'_\lambda \exp\left(-\frac{2E'_{ad}}{k_B T}\right) \right\}^{1/2} .$$

where  $x = n'/n_T$ ,

$$E_{ad} = \frac{e^2}{2\epsilon r_0} ,$$

and

$$E'_{ad} = \frac{e^2}{2\epsilon r'_0} ,$$

$$n_\lambda = \frac{\lambda}{8\pi^{1/2} r_0^4} ,$$

$$n'_\lambda = \frac{\lambda}{8\pi^{1/2} (r'_0)^4} , \quad \lambda = e^2/\epsilon k_B T ,$$

where  $r'_0$  is the distance of closest approach of an  $\text{Li}^+$  ion to an  $\text{LiO}^-$  ion,  $r_0$  is the distance of closest approach of an  $\text{Li}^+$  ion to an  $\text{LiSO}_4^-$  ion,

The lower limit  $r_0$  can be estimated from Pauling's values [27] for the S-O distance and the radii for O and  $\text{Li}^+$ . Adding these values gives the result  $r_0 = 2.70\text{\AA}$ . From Pauling's radii [27] one obtains the value  $2.0\text{\AA}$  for  $r'_0$ .

Using the Einstein relation connecting the mobility  $\mu$  and the diffusion coefficient  $D$ , and recognizing that both quantities may have an activation energy  $E_{ah}$  associated with activated hopping, one can write

$$\begin{aligned} \mu &= \frac{eD}{k_B T} \\ &= \frac{eD_0}{k_B T} \exp\left(-\frac{E_{ah}}{k_B T}\right) . \end{aligned}$$

one sees that a plot of  $\ln(\sigma T^{3/2})$  vs.  $1/T$

for  $x = 0$  or  $y = 0$  should yield a straight line. Even when neither  $x$  nor  $y$  is zero, this plot should still be very close to a straight line. When the slope of the line is multiplied by  $-k_B$  the effective activation energy  $E_a$  for the conductivity is obtained.

In this case the parameter  $n_T$  is taken to be  $1.0 \times 10^{22} \text{ cm}^{-3}$  while the parameters  $D_0$ ,  $E_{ah}$  and  $\epsilon$  are varied to give the best least-squares fit to the experimental data. The mobility activation energy  $E_{ah}$  is determined from the  $y = 0$  data (with only  $\text{Li}_2\text{O}$  present) to be 0.38 eV and is kept at this same value for the  $y \neq 0$  data (with  $\text{Li}_2\text{SO}_4$  present). The parameters  $D_0$  and  $\epsilon$  are determined for each value of  $y$ . Calculations were carried out using both procedures. The results are as follows.

The quantity  $\ln(\sigma T^{3/2})$  is plotted against the reciprocal of the absolute temperature in Fig. 17 for each of the compositions  $y = 0.0, 0.05, 0.10$  and  $0.15$ . The theoretical curves are straight lines which fit the experimental data quite well except for some deviations at the two lowest temperatures. From the values of  $\epsilon$  determined by the fits to the data, the values of the dissociation activation energies  $E_{ad}$  and  $E'_{ad}$  were calculated

The overall activation energy  $E_a$  was determined from the slopes of the theoretical curves in Fig. 17. The results for  $D_0$ ,  $\epsilon$ ,  $E_{ad}$ ,  $E'_{ad}$  and the theoretical and experimental values of  $E_a$  are presented in Table 1. One can see that the four quantities  $D_0$ ,  $\epsilon$ ,  $E_{ad}$  and  $E'_{ad}$  show only a weak dependence upon the composition variable  $y$ , and that their magnitudes are physically reasonable. The magnitude of  $D_0$  agrees roughly with the relation [28]  $D_0 = \nu_+ r_h^2 / 6$  where  $\nu_+$  and  $r_h$  are the hopping frequency and

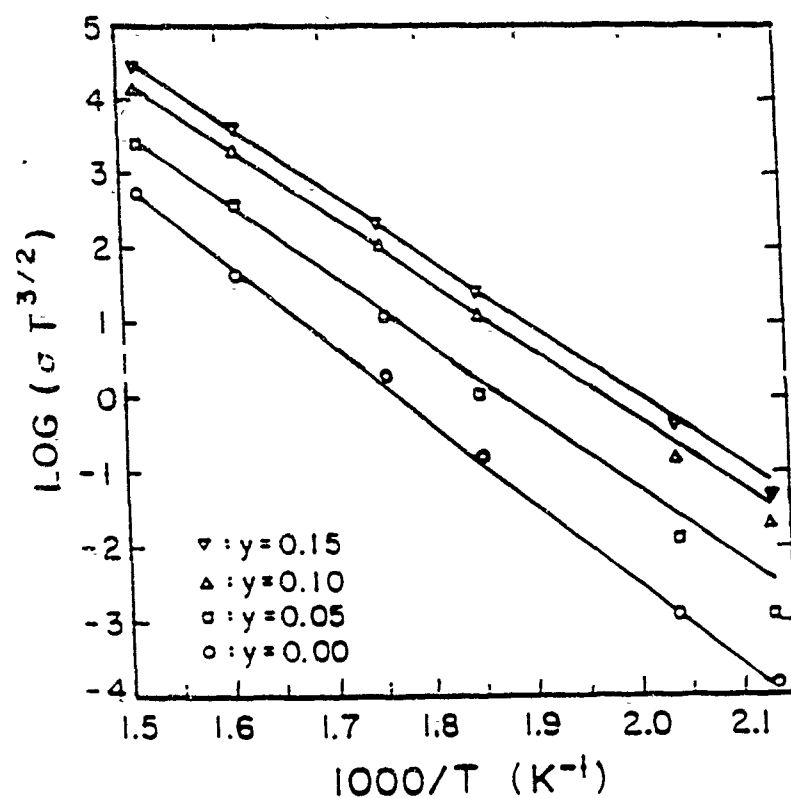


Fig. 17. Variations of  $\ln(\sigma T^{3/2})$  with the reciprocal absolute temperature for different concentrations  $\gamma$  of  $\text{Li}_2\text{SO}_4$  in  $\text{B}_2\text{O}_3$ -0.5 $\text{Li}_2\text{O}$ - $\text{Li}_2\text{SO}_4$ . The theoretical results are represented by the solid curves.

TABLE 1. Conductivity parameters for  $B_2O_3-xLi_2O-yLi_2SO_4$  without Debye-Hückel effects

$y$	$D_0$ ( $cm^2-s^{-1}$ )	$\epsilon$	$E_{ad}$ (eV)	$E'_{ad}$ (eV)	$E_a$ (theoretical) (eV)	$E_a$ (experimental) (eV)
0.00	0.14	8.1	--	0.44	1.02	0.93
0.05	0.16	8.2	0.32	0.44	0.86	0.90
0.10	0.22	8.4	0.31	0.43	0.83	0.83
0.15	0.24	8.5	0.30	0.42	0.81	0.82

TABLE 2. Conductivity parameters for  $B_2O_3-xLi_2O-yLi_2SO_4$  with Debye-Hückel effects

$y$	$D_0$ ( $cm^2-s^{-1}$ )	$\epsilon$	$E_{ad}$ (eV)	$E'_{ad}$ (eV)	$E_a$ (theoretical) (eV)	$E_a$ (experimental) (eV)
0.00	0.039	8.1	-	0.44	0.93	0.93
0.05	0.041	8.2	0.32	0.44	0.82	0.90
0.10	0.056	8.4	0.31	0.43	0.80	0.83
0.15	0.058	8.5	0.30	0.42	0.80	0.82

hopping distance respectively. Taking  $0.2 \text{ cm}^2\text{s}^{-1}$  as being a representative value of  $D_0$  from Table 1, and taking [28]  $\nu_{\pm} = 10^{14} \text{ s}^{-1}$ , we find that  $r_h \approx 11 \text{ \AA}$ ; a not unreasonable value.

The conductivity  $\sigma$  is plotted against  $y$  in Fig. 18(a) for the temperatures 469 and 489 K, in Fig. 18(b) for temperatures 539 and 569 K and in Fig. 18(c) for temperatures of 619 and 659 K. As in Fig. 17 there are appreciable deviations between the theoretical and the experimental results for the two lowest temperatures, but for the four highest temperatures the agreement is good. One can, of course, improve the agreement for the two lowest temperatures by making  $\epsilon$  temperature dependent.

The analysis which has been presented here differs significantly from the standard analysis<sup>(26,28)</sup> of the role of positive ion vacancies in the electrical conductivity of doped alkali halide crystals. In the standard treatment a positive ion vacancy is regarded as being completely free unless it occupies one of the 12 next-nearest-neighbor sites of a divalent cation. We make no such assumption in our treatment and take into account the Coulomb interaction at large separations of an  $\text{Li}^+$  ion from an  $\text{LiO}^-$  or  $\text{LiSO}_4^-$  ion.

The theory which we have developed for the dissociation of  $\text{Li}_2\text{SO}_4$  in lithium borate glasses  $\text{B}_2\text{O}_3\text{-Li}_2\text{O}$  gives a good representation of the dependence of the conductivity on the  $\text{Li}_2\text{SO}_4$  content and on the temperature. By comparing the experimentally determined conductivity with the theoretical results one obtains information concerning the activation energy associated with the mobility, the diffusion constant and the dielectric constant.

A closer examination of the experimental data would require

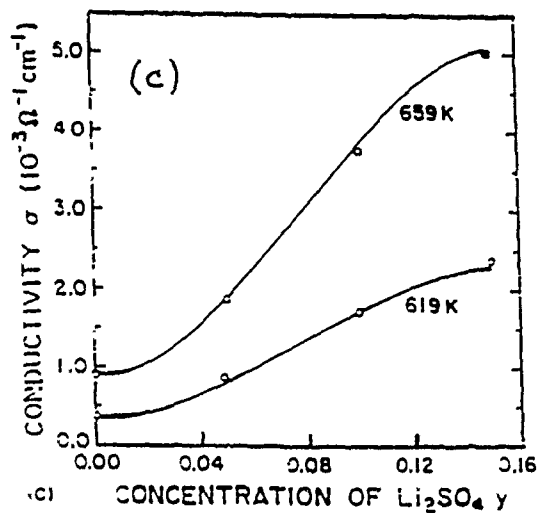
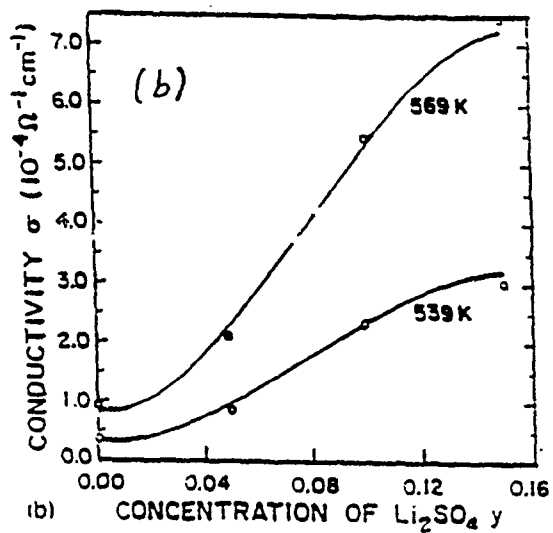
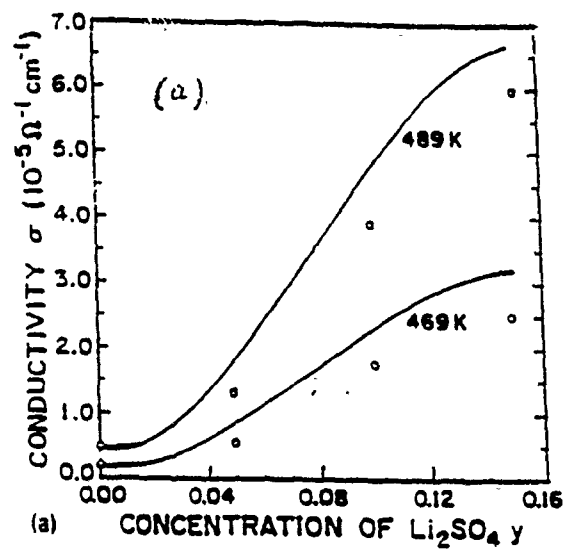


Fig. 13. Variation of the conductivity  $\sigma$  with  $\text{Li}_2\text{SO}_4$  concentration  $y$  for (a)  $T = 469$  K and  $489$  K, (b)  $T = 539$  and  $569$  K, and (c)  $T = 619$  and  $659$  K.

some discussion of the pre-exponential factor related to the relaxation time and of the effect of interactions between  $\text{Li}^+$  ions on the conductivity. A detailed examination of the latter effect would require a more elaborate theory taking into account the Debye-Hückel concentration dependence of the ionic atmosphere. Such a treatment is presented in the next section.

### 5.3. Effect of Coulomb Interactions

The effect of Coulomb interactions between free lithium ions on the electrical conductivity of borate glass modified by  $\text{Li}_2\text{O}$  and doped with  $\text{Li}_2\text{SO}_4$  has been examined [29]. The improved theory shows a distinct lowering of the conductivity, at least for relatively low temperatures, arising from the Coulomb interactions between free  $\text{Li}^+$  ions. At low temperatures a given  $\text{Li}^+$  ion is slowed by its interactions with its ion atmosphere.

The effect of the Coulomb interaction between free  $\text{Li}^+$  ions can be taken into account by using the Debye-Hückel theory in a form applied by Lidiard [26] to a similar problem. What has to be done is to replace the dissociation constants  $K(T)$  and  $K'(T)$  by  $K_{\text{D-H}}(T)$  and  $K'_{\text{D-H}}(T)$  given by

$$K_{\text{D-H}}(T) = \frac{1}{n_1} \exp\left[\frac{\lambda}{r_0} - \frac{1}{2}\left\{(2\lambda)^{3/2}(4\pi n_{\text{FT}})^{1/2} \frac{1}{1+\kappa r_1}\right\}\right]$$

$$K'_{\text{D-H}}(T) = \frac{1}{n_1'} \exp\left[-\frac{\lambda}{r_0'} - \frac{1}{2}\left\{(2\lambda)^{3/2}(4\pi n_{\text{FT}})^{1/2} \frac{1}{1+\kappa r_1'}\right\}\right],$$

where  $\kappa^2 = 8\pi n_{\text{FT}}\lambda$ . The quantities  $r_1$  and  $r_1'$  are the minimum distances of  $\text{Li}^+$  from  $\text{LiSO}_4^-$  and  $\text{LiO}^-$  respectively, for which the  $\text{Li}^+$  ion can be considered to be free. We do not know  $r_1$  and  $r_1'$  a priori, but we anticipate that  $r_1 > r_0$  and  $r_1' > r_0'$ . Their precise

specification will be given later. Since the new equilibrium constants involve  $n_{FT}$ , the mass action law equations are now transcendental equations for the determination of  $n_{FT}$  and must be solved self-consistently.

If we introduce the quantities  $n = n_0 + n_B$  and  $n' = n'_0 + n'_B$  which are respectively the total concentrations of  $Li_2SO_4$  and  $Li_2O$ , we can rewrite

$$n_0 = \frac{n}{1 + n_{FT} K_{D-H}(T)}$$

$$n'_0 = \frac{n'}{1 + n_{FT} K'_{D-H}(T)} .$$

Using conservation of lithium ions, we have

$$\begin{aligned} n_{FT} &= n_0 + n'_0 \\ &= \frac{n}{1 + n_{FT} K_{D-H}(T)} + \frac{n'}{1 + n_{FT} K'_{D-H}(T)} \end{aligned}$$

This is the equation that must be solved self-consistently to give the total free  $Li^+$  ion concentration  $n_{FT}$ .

Once  $n_{FT}$  is found, we can determine the conductivity  $\sigma$  using the relation

$$\sigma = e\mu n_{FT}$$

where  $\mu$  is the mobility. In the presence of the Coulomb interaction between the free  $Li^+$  ions, the mobility  $\mu_n$  for the non-interacting case must be multiplied by a factor  $\gamma$  given by

$$\zeta = \frac{nf}{n+n'} + \frac{n'f'}{n+n'} ,$$

where

$$f = 1 - \frac{\lambda \kappa}{3(2^{1/2}+1)(1+\kappa r_1)(2^{1/2}+\kappa r_1)} ,$$

$$f' = 1 - \frac{\lambda \kappa}{3(2^{1/2}+1)(1+\kappa r_1')(2^{1/2}+\kappa r_1')} .$$

The expression for the conductivity then takes the form

$$\sigma = e\mu_n \zeta n_{FT} .$$

Using the Einstein relation between the mobility  $\mu_n$  and the diffusion coefficient  $D$ , we can write

$$\begin{aligned} \mu_n &= \frac{eD}{k_B T} \\ &= \frac{eD_0}{k_B T} \exp\left(-\frac{E_{ah}}{k_B T}\right) , \end{aligned}$$

where  $E_{ah}$  is the mobility activation energy. Also contributing to the overall conductivity activation energy  $E_a$  are the dissociation activation energies  $E_{ad}$  and  $E_{ad}'$  for  $\text{Li}_2\text{SO}_4$  and  $\text{Li}_2\text{O}$  respectively

The values of the parameters  $r_0$  and  $r_0'$  were taken to be those given in section 5.2:  $r_0 = 2.7 \text{ \AA}$  and  $r_0' = 2.0 \text{ \AA}$ . The values of the other parameters were determined as follows. For the case  $y = 0$  (no  $\text{Li}_2\text{SO}_4$  present) with free-lithium-ion interactions neglected, the values of  $D_0$ ,  $\epsilon$  and  $E_{ah}$

were determined by making a best fit of the calculated conductivity to the experimental data. In the case of  $\epsilon$ , the value reflects additional experimental data not considered in section 5.2. The value of  $E_{ah}$  obtained, 0.48 eV, was used in all the subsequent calculations. For each case with  $y \neq 0$  and free-ion interactions neglected, we redetermined  $D_0$  and  $\epsilon$  to give the best fit to the data.

When the interactions between free  $\text{Li}^+$  ions were included, the values of  $D_0$ ,  $r_1$  and  $r'_1$  were obtained by a best fit to the data, but the values of  $\epsilon$  were maintained the same as in the non-interacting case. Using calculated values of the conductivity  $\sigma$ , the values of the activation energy  $E_a$  were found from the slope of the plot of  $\ln(\sigma T^{3/2})$  vs.  $1/T$ . The best values of  $r_1$  and  $r'_1$  were determined to be  $r_1 = 3r_0$  and  $r'_1 = 3r'_0$ . The values of the remaining parameters are presented in Table 2.

The results for the conductivity are presented in Figs. 19-21 for the various compositions and temperatures considered. Except for the highest temperatures and  $\text{Li}_2\text{SO}_4$  concentrations, there is a small but distinct lowering of the conductivity which arises from the Coulomb interaction between the free  $\text{Li}^+$  ions. Although the interaction leads to an increase in the free-ion concentration due to shielding of the negative ion potential, this effect is more than offset by a reduction in the mobility. A given ion is slowed by its interaction with its ion atmosphere. As the temperature increases, the lowering of the conductivity decreases and is hardly evident at the two highest temperatures. This behavior can be understood on the basis that an increase in temperature increases the random thermal motion of the free  $\text{Li}^+$

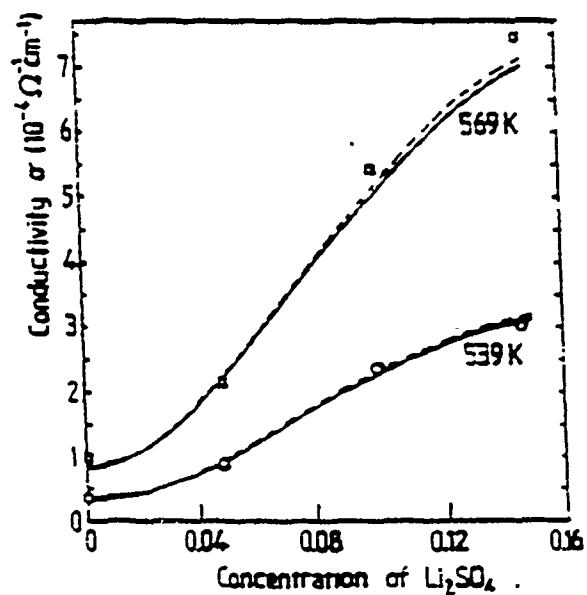


Fig. 20. Variation in the conductivity  $\sigma$  as a function of  $\text{Li}_2\text{SO}_4$  concentration  $\gamma$  for  $T = 539 \text{ K}$  and  $T = 569 \text{ K}$ : —, with inclusion of the interaction between free  $\text{Li}^+$  ions, - - -, without inclusion of the interaction between free  $\text{Li}^+$  ions.

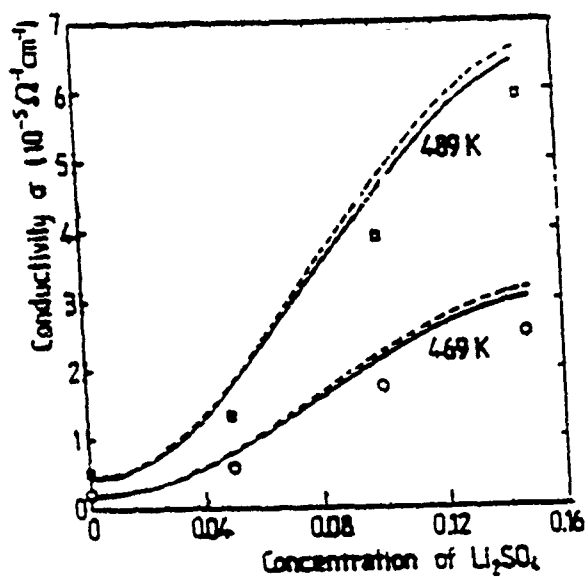


Fig. 19. Variation in the conductivity  $\sigma$  as a function of  $\text{Li}_2\text{SO}_4$  concentration  $y$  for  $T = 469\text{K}$  and  $T = 489\text{K}$ : —, with inclusion of the interaction between free  $\text{Li}^+$  ions; ---, without inclusion of the interaction between free  $\text{Li}^+$  ions.

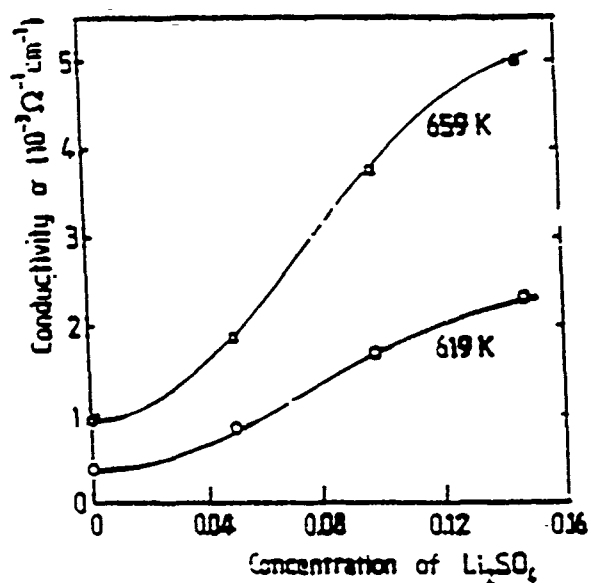


Fig. 21. Variation in the conductivity  $\sigma$  as a function of  $\text{Li}_2\text{SO}_4$  concentration  $y$  for  $T = 619 \text{ K}$  and  $T = 659 \text{ K}$ . The cases with and without inclusion of the interaction between free  $\text{Li}^+$  ions are indistinguishable.

ions and reduces the correlations which arise from the Coulomb interaction between them. These results are consistent with the picture that the lithium borate glasses behave as weak electrolytes with only a small fraction of the  $\text{Li}_2\text{O}$  and  $\text{Li}_2\text{SO}_4$  molecules ionized at the temperatures employed in the experiments.

#### 5.4. Summary

The fast ion conductivity in borate glasses such as  $\text{B}_2\text{O}_3\text{-xLi}_2\text{O-yLi}_2\text{SO}_4$  calculated from a statistical mechanical theory based on the assumption of a partial dissociation of the dopant salt,  $\text{Li}_2\text{SO}_4$ , and the modifier,  $\text{Li}_2\text{O}$ , compares well with the experimental results. The temperature dependence of the conductivity obtained experimentally is well reproduced by the theory. In the theoretical treatment given in section 5.2, the Coulomb interaction between free  $\text{Li}^+$  ions was not taken into account. This theory already gives the possibility of obtaining information concerning the activation energy associated with the mobility, the diffusion constant and the dielectric constant by comparing the experimentally determined conductivity with the theoretical result.

An improvement in our treatment is achieved by the calculations presented in section 5.3 which show that a distinct lowering of the conductivity, at least for relatively low temperatures, arises from the Coulomb interaction between free  $\text{Li}^+$  ions. At low temperatures a given  $\text{Li}^+$  ion is slowed by its interactions with its ion atmosphere. As the ion atmosphere becomes more diffuse at higher temperatures, the effective slowing of the motion of an individual ion by the Coulomb interaction with its neighbors decreases.

A further refinement in the theoretical treatment of fast ion conduction may come from the consideration that the  $\text{LiO}^-$  and  $\text{LiSO}_4^-$  ions fixed at given sites in the glass network may also have the possibility of dissociating to yield  $\text{Li}^+$  ions which will further contribute to the conductivity. This process is less probable than the first dissociation, because its activation energy is significantly larger than that for the first dissociation. At sufficiently high temperatures, the influence of the second dissociation would be indicated by an increase in the apparent activation energy.

## 6. Lithium motion in borate glasses

### 6.1. Introduction

The infrared spectrum of lithium borate glasses  $\text{B}_2\text{O}_3\text{-xLi}_2\text{O-yLi}_2\text{SO}_4$  can be regarded as consisting of two parts: the low frequency domain which concerns the charge carrier dynamics and the higher frequency region concerning the host dynamics.

In sections 2 and 3, the dynamical properties of the host network were examined. We shall now turn to free carrier dynamics.

Structural and dynamical properties are generally investigated by Raman spectroscopy [30] and the ionic conductivity is measured by means of complex impedance spectroscopy [25]. Infrared spectroscopy is a complementary method offering the possibility of deducing the frequency-dependent conductivity at low frequencies and the conduction ion dynamics.

The infrared reflectivity of  $\text{B}_2\text{O}_3\text{-xLi}_2\text{O-yLi}_2\text{SO}_4$  increases considerably at frequencies below  $500\text{ cm}^{-1}$ . This high reflectiv-

ity corresponds to the motion of the  $\text{Li}^+$  ions and allows us to deduce the frequency dependent ionic conductivity. Analysis based on a simple double well potential model leads to a picture in which the characteristic vibrational frequencies of the  $\text{Li}^+$  ion is distributed over a large frequency range corresponding to different site configurations. The extent of the frequency distribution is a function of the free ion concentration. A drastic increase of the damping coefficient is observed when the concentration increases.

The potential barrier regulating the motion of the  $\text{Li}^+$  ions between different site configurations also increases with increasing  $\text{Li}^+$  ion concentration which corresponds to a decrease of residence frequency and increase of residence relaxation time.

#### 6.2. Description of the Model

Infrared and Raman spectroscopy [30] as well as nuclear magnetic resonance measurements [31] indicate that with increasing modifier concentration  $x$  the amount of  $\text{BO}_4$  groups increases up to a maximum of 40% of boron atoms in tetrahedral coordination for  $x = 0.4$ . Above this concentration the amount of  $\text{BO}_4$  decreases. The relative abundance of the  $\text{BO}_4^-$  ions in the vitreous matrix suggests that the small  $\text{Li}^+$  ion spends a certain time oscillating against that radical. The motion of the  $\text{Li}^+$  ion at long distances through the glass medium can be characterized by an activation energy  $E_a$  much larger than the double-well potential  $\Delta$  (Fig. 22). The  $\text{Li}^+$  ion should overcome this potential when moving from one position in the neighborhood of  $\text{BO}_4^-$  to another. Thus, the dynamics of the  $\text{Li}^+$  ion could be schematically treated within the framework of a double potential well model.

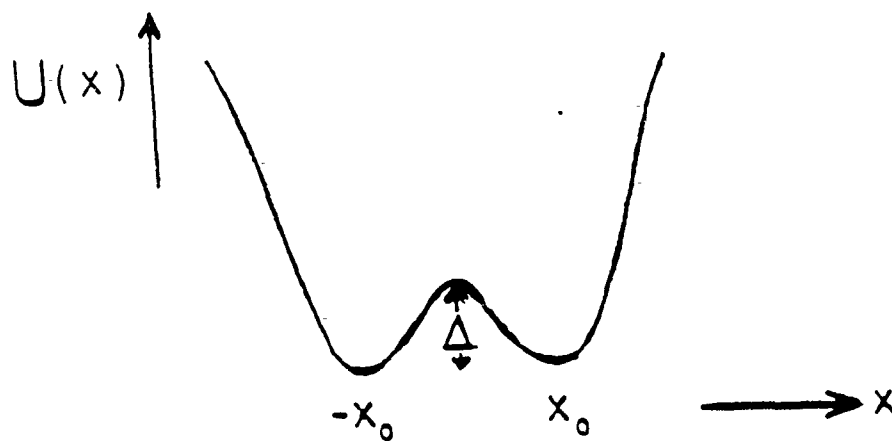


Fig. 22. Scheme of double potential well intervening in the motion of the  $\text{Li}^+$  ion through the barrier potential  $\Delta$ .

The equation for the oscillatory motion of the  $\text{Li}^+$  ion considered as a Brownian particle can be written as

$$m \ddot{x} - m\gamma \dot{x} + U'(x) = f(t) ,$$

with

$$U'(x) = \frac{\partial U(x)}{\partial x}$$

and

$$U(x) = \Delta \left[ \left( \frac{x}{x_0} \right)^4 - 2 \left( \frac{x}{x_0} \right)^2 \right] .$$

$U(x)$  describes the double potential well with minima situated at  $x = \pm x_0$ . The damping coefficient  $\gamma$  and the random force  $f(t)$  describe the interaction of the mobile ions with the thermal vibrations of the network.

Following the treatment given by Schneider et al. [32], frequency-dependent conductivity can be written in the form

$$\sigma(\omega) = f r(\omega) .$$

Here  $f$  is the oscillator strength defined as

$$f = \frac{N_{\text{Li}} e^2}{m_{\text{Li}}}$$

and  $r(\omega)$  is the frequency dependent scattering time defined by the expression

$$r(\omega) = [2 + \gamma + \chi(\omega)]^{-1} ,$$

with  $z = i\omega$ , and the memory function

$$\chi(z) = \tilde{\omega}_0^2 \left[ \frac{\alpha}{z} + \frac{1-\alpha}{z-b} \right] .$$

Here  $\tilde{\omega}_0^2 = \langle U'' \rangle / m$  ,

$$\alpha = (\beta \langle x^2 \rangle \langle U'' \rangle)^{-1} ,$$

$$b = \tilde{\omega}_0^2 (1-\alpha) / (\alpha \tilde{\omega}_0^2 \tau^{-\gamma}) ,$$

$\langle \dots \rangle$  is the thermal average, and  $\beta^{-1} = k_B T$ . The time  $\tau$  is related to the escape time by  $\tau = \frac{\tau_{esc}}{2}$ .

The adjustable parameters for comparison with experimental data are the oscillator strength  $f$ , the lithium vibrational frequency in the site  $\omega_0$ , the damping coefficient  $\gamma$ , and the dimensionless parameter  $\delta$  related to the height of the potential barrier  $\delta = 4\Delta\beta$ . With the frequency dependent conductivity  $\sigma(\omega)$  in hand we can calculate the dielectric function

$$\epsilon(\omega) = \epsilon_\infty + \frac{4\pi i \sigma(\omega)}{\omega} ,$$

and confront the reflectivity which is obtained experimentally

$$R = \left| \frac{\sqrt{\epsilon} - 1}{\sqrt{\epsilon} + 1} \right|^2 .$$

### 6.3. Comparison with Experimental Data

Infrared reflectivity measured with the Bruker type IFS113 vacuum infrared Fourier spectrometer give broad spectra over the range of 10 - 3000  $\text{cm}^{-1}$ . In Fig. 23 is shown the reflectivity spectrum of a glass with composition  $\text{B}_2\text{O}_3\text{-}0.7\text{Li}_2\text{O}$  taken at room

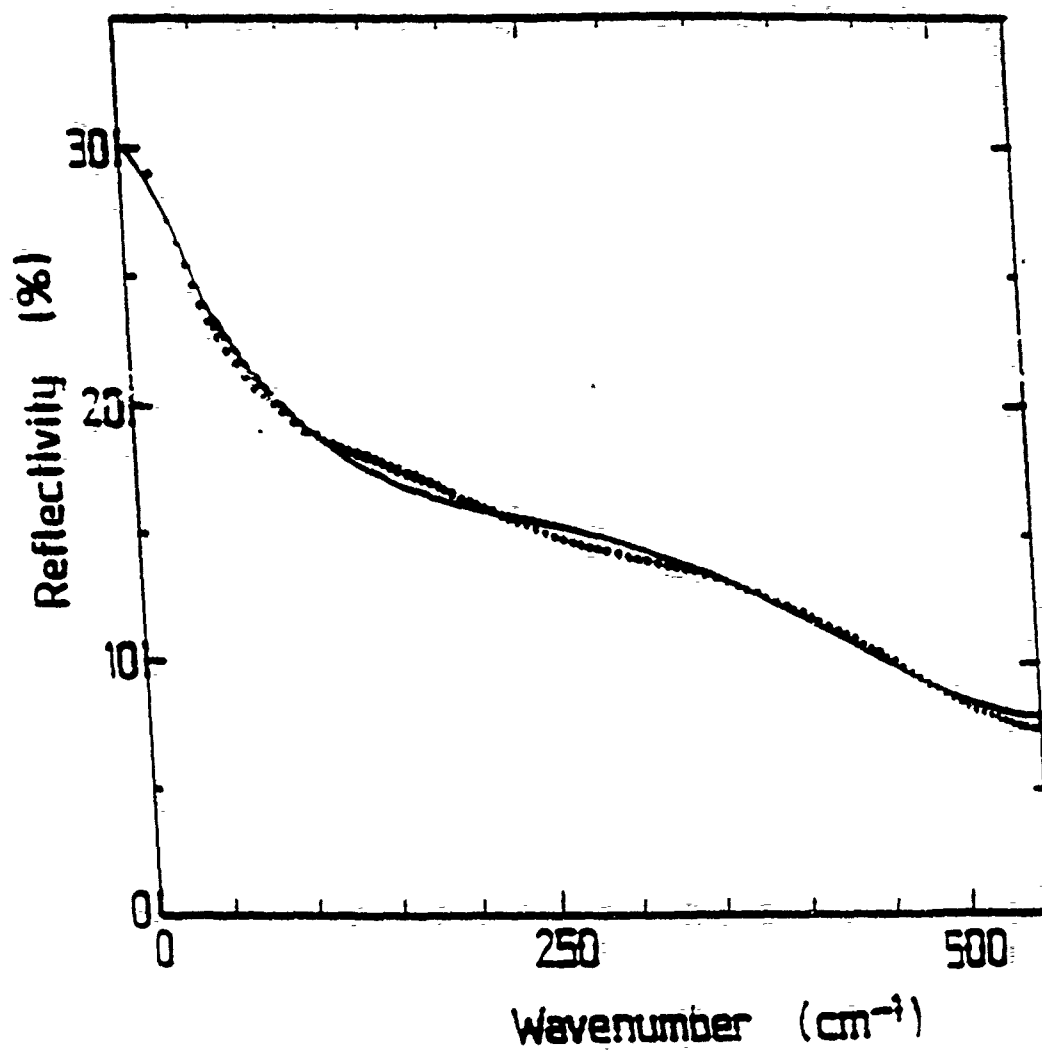


Fig. 23. Reflectivity spectrum of borate glass  $B_2O_3-0.7Li_2O$  at 300K. The full line is the calculated curve and the points are experimental data.

temperature. The dotted line represents the experimental points and the continuous line is the calculated curve.

Figure 24 shows the frequency dependent conductivity  $\sigma(\omega)$  for the same sample, the real and imaginary parts of the dielectric constants and the energy loss. The points represent the Kramers-Kronig inversion of the experimental reflectivity and the continuous line gives the calculated curves. The maximum of  $\text{Im}[\epsilon(\omega)]$  in Fig. 24 situated at  $\omega_2 = 40 \text{ cm}^{-1}$  determines the relaxation frequency of the  $\text{Li}^+$  ion jumping from one potential well to another through the barrier  $\Delta$ .

When a dopant, such as  $\text{Li}_2\text{SO}_4$ , is added to the borate glass the ionic conductivity increases. A series of doped borate glasses  $\text{B}_2\text{O}_3\text{-}0.7\text{Li}_2\text{O-}y\text{Li}_2\text{SO}_4$  in a broad concentration range of the dopant salt,  $0 \leq y \leq 0.5$  has been studied with the same experimental technique. The remarkable feature in this investigation is that whereas the frequency of the maximum of the broad band  $\omega_0$  does not change with concentration, one observes a significant change of the damping coefficient  $\gamma$ . The damping coefficient varies from  $\gamma = 240 \text{ cm}^{-1}$  when  $y = 0$  to  $\gamma = 62 \text{ cm}^{-1}$  for  $y = 0.5$ . From the conductivity  $\sigma(\omega)$ , the real and imaginary parts of the dielectric function,  $\text{Re}(\epsilon)$  and  $\text{Im}(\epsilon)$ , and  $\text{Im}(-1/\epsilon)$  deduced from the reflectivity spectra for different concentrations  $y$  of the dopant  $\text{Li}_2\text{SO}_4$ , one can deduce that the relaxation frequency  $\omega_2$  is now  $20 \text{ cm}^{-1}$ , a drastic decrease with increased doping.

From Fig. 25, which is a summary of the experimental results, one observes that while the characteristic frequency  $\omega_0$  remains constant, the damping decreases and the oscillator strength  $f$  increases with increasing dopant concentration  $y$ .

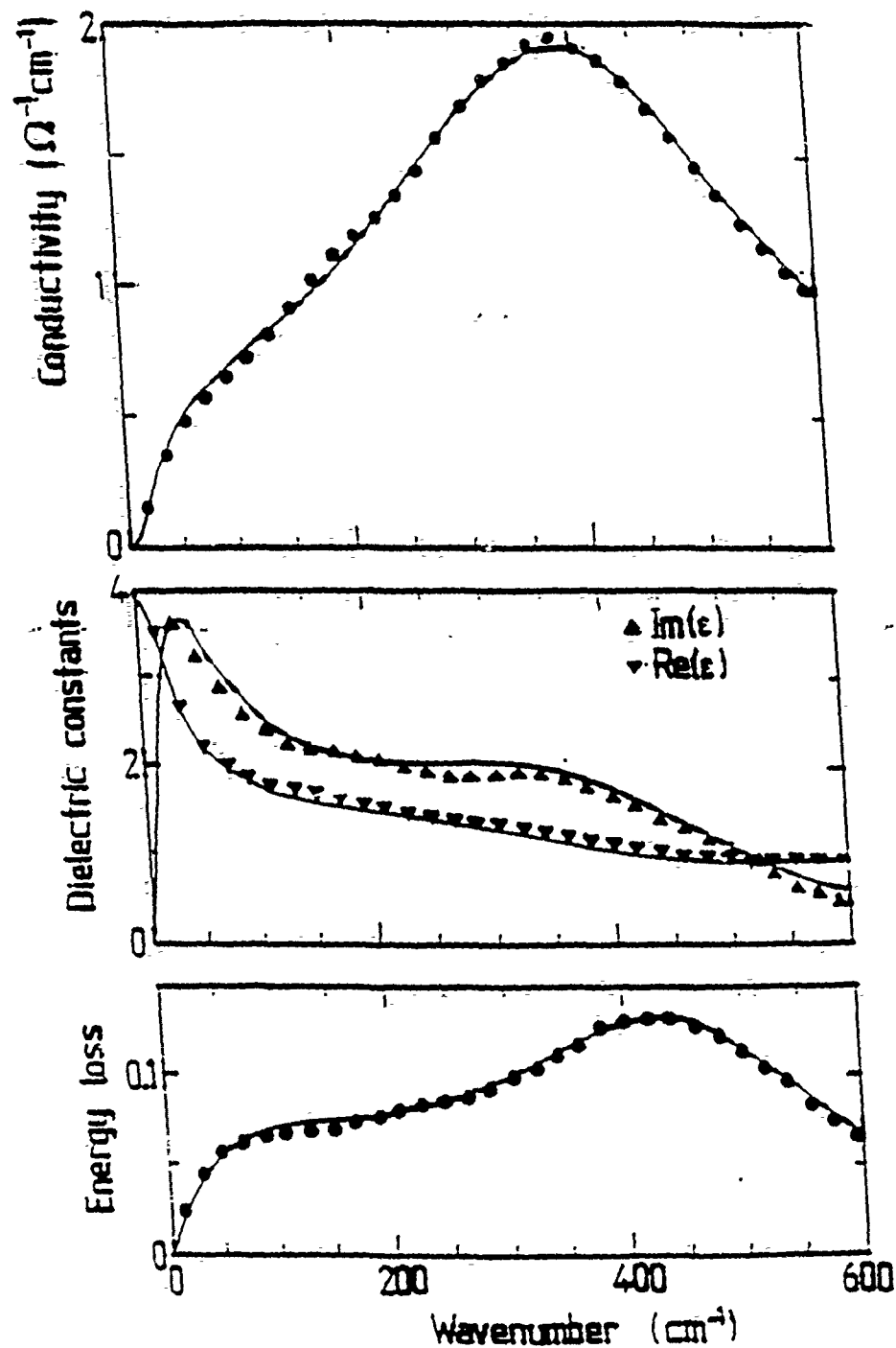


Fig. 24. Frequency dependent conductivity  $\sigma(\omega)$ , real  $\text{Re}(\epsilon)$  and imaginary  $\text{Im}(\epsilon)$  parts of the dielectric constant and the energy loss  $\text{Im}(-1/\epsilon)$  of the borate glass  $\text{B}_2\text{O}_3-0.7\text{Li}_2\text{O}$  at 300K. The points are the Kramers-Kronig inversion of the experimental reflectivity and the full line gives the calculated curve.

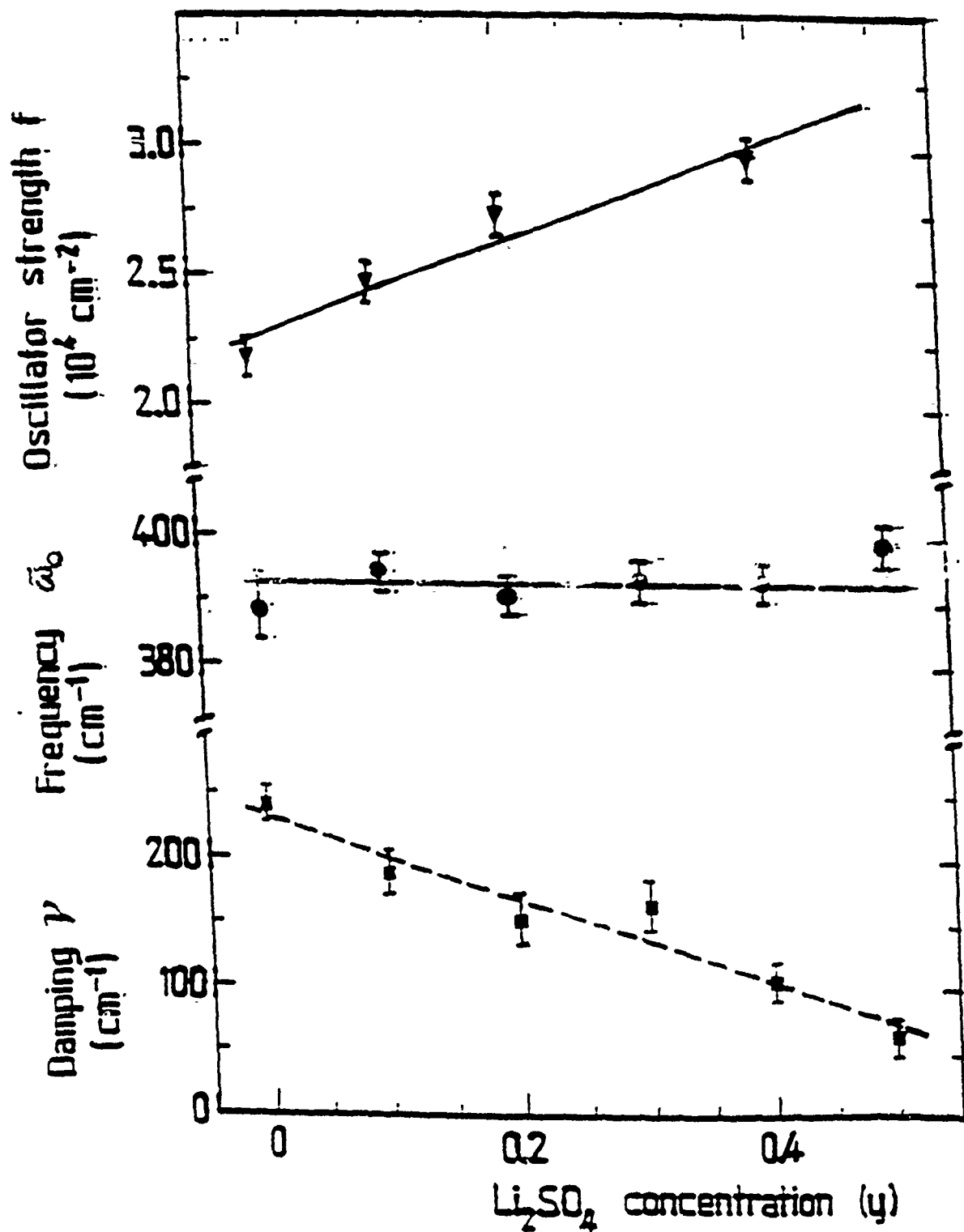


Fig. 25. Oscillator strength  $f$ , attempt frequency  $\omega_0$  and the damping factor  $\gamma$  as functions of the dopant concentration in borate glasses.

From the results shown in Fig. 24 one can see that the characteristic frequency for the  $\text{Li}^+$  ion vibration in a nondoped borate glass  $\text{B}_2\text{O}_3\text{-}0.7\text{Li}_2\text{O}$  is widely spread over a large frequency range from 120-600  $\text{cm}^{-1}$  but has a maximum at  $\omega_0 = 389 \text{ cm}^{-1}$ , and has the damping constant  $\gamma = 243 \text{ cm}^{-1}$ . The resonance centered at 389  $\text{cm}^{-1}$  is very broad which is an indication that the configuration of the  $\text{BO}_4^-$  site attracting the  $\text{Li}^+$  ion is not unique. This result suggests rather that  $\text{Li}^+$  is found in different sites in the borate glass at different space positions with regard to the  $\text{BO}_4^-$  ion. In each specific site,  $\text{Li}^+$  has a characteristic vibration but because of the large variety of site configurations, the characteristic frequencies are spread over a broad frequency range with a maximum in the distribution around 390  $\text{cm}^{-1}$ . At low  $\text{Li}^+$  concentration the whole spectrum of different sites is available for  $\text{Li}^+$  occupation and the distribution of occupied sites is quite broad. When the  $\text{Li}^+$  concentration is increased with the addition of the dopant  $\text{Li}_2\text{SO}_4$  into the borate glass  $\text{B}_2\text{O}_3\text{-}0.7\text{Li}_2\text{O}$ , the most frequent site configurations become more readily occupied, the occupancy density of closely resembling sites becomes greater, and the dispersion in the distribution decreases. The increasing  $\text{Li}^+\text{-Li}^+$  Coulomb interaction forces the  $\text{Li}^+$  ion into the most favorable configuration. Thus, the resonance sharpens significantly which is indicated by a considerable decrease of the damping constant, i.e., an increase of the relaxation time, the time the  $\text{Li}^+$  spends in a site of given configuration. The oscillator strength  $f$  increases, of course, with the increase of the dopant concentration because the number of  $\text{Li}^+$  ions increases. The relaxation frequency of  $\text{Li}^+$ ,  $\omega_2 = 2\omega_{\text{esc}}$ , given by the maximum

of  $\text{Im}(\epsilon)$  is  $\omega_2 = 40 \text{ cm}^{-1}$  for the nondoped borate glass. This gives a potential barrier  $\Delta = 21.7 \text{ meV}$ . For the doped glasses we obtain  $\omega_2 = 20 \text{ cm}^{-1}$  and  $\Delta = 40 \text{ meV}$ . The most probable or the most abundant potential wells are twice as deep for high  $\text{Li}^+$  concentration. This is compatible with a larger residence time and smaller damping constants, i.e., small escape frequency. From the definition of the oscillator strength one should expect a linear relation between  $N_{\text{Li}}$  and  $f$  with a given slope ( $e^2/m_{\text{Li}}$ ). Comparison of the values of  $f$  obtained from the fit with the experimental data,  $f_{\text{exp}}$ , and that calculated with eq. (6.5),  $f_{\text{cal}}$ , we see a considerable difference. Considering the values listed in Table 3, one observes that  $f_{\text{exp}}$  is practically double  $f_{\text{cal}}$ . This suggests that  $e$  and  $m_{\text{Li}}$  are not the charge and mass of the free  $\text{Li}^+$  ion but are instead the effective charge ( $e^*$ ) and effective mass ( $m^*$ ) as modified by the polarization induced in the medium. The sites in which  $\text{Li}^+$  vibrates are polarizable, which must be taken into account when calculating  $f$ .

The frequency dependent conductivity sum rule is different for a rigid and for a polarizable medium. For a rigid medium we have

$$\int_0^{\infty} \sigma(\omega) d\omega = \frac{\pi}{2} \frac{N_{\text{Li}} e^2}{m_{\text{Li}}} ,$$

whereas for a polarizable medium the sum rule is

$$\int_0^{\infty} \sigma(\omega) d\omega = \frac{\pi}{2} \frac{N_{\text{Li}} e^{*2}}{m^*} \left( \frac{\epsilon_{\infty} + 2}{3} \right)^2 .$$

Here  $e^*$  is the Szigeti effective charge and  $m^*$  the reduced mass which for a tetrahedral oxygen environment of the  $\text{Li}^+$  will be given, for example, by

TABLE 3. Values of lithium concentration, dielectric constant, and oscillator strength for various concentrations  $y$  of the dopant

$y$	$N_{Li} (cm^{-3})$	$\epsilon_{\infty}$	$f_{exp} (cm^{-2})$	$f_{cal} (cm^{-2})$	$f_{exp}/f_{cal}$
0.0	$2.2 \cdot 10^{22}$	2.06	21774	12204	1.784
0.1	$2.28 \cdot 10^{22}$	2.06	24704	12648	1.953
0.2	$2.32 \cdot 10^{22}$	2.18	27369	12869	2.127
0.4	$2.38 \cdot 10^{22}$	2.13	29512	13202	2.235

$$m^* = \frac{m_{Li} m_O}{m_{Li} + 4m_O} = 0.68 m_{Li} .$$

The ratio  $e^*/e$  is given by

$$e^*/e = \left[ \frac{f_{exp}}{f_{col}} \frac{m^*}{m_{Li}} \frac{\epsilon_{\infty} + 2}{3} \right]^{1/2} .$$

For different dopant concentrations  $y$  we obtain the values given in Table 4.

This result shows that, in fact, the polarizability of the  $B_2O_3-0.7Li_2O-Li_2SO_4$  network does not affect considerably the  $Li^+$  oscillatory motion because the effective charge  $e^*$  is not very different from the free  $Li^+$  charge  $e$ .

TABLE 4. Effective charge of  $\text{Li}^+$  for various concentrations  $y$  of the dopant.

$y$	$e^*/e$
0	0.81
0.1	0.85
0.2	0.86
0.4	0.89

## 7. Conclusions

After long discussions in the literature it now seems established that the  $\nu\text{-B}_2\text{O}_3$  network is mainly formed by boroxol rings connected with B-O-B bonds and  $\text{BO}_3$  triangles. Direct calculation of the vibration of boron oxide glass, using the Bethe lattice approximation, show that the boroxol ring vibration at  $800\text{ cm}^{-1}$  remains sharp even when an infinite network is formed.

The effect of the addition of the modifier  $\text{Li}_2\text{O}$ , was investigated experimentally by Raman and infrared spectroscopy and theoretically by network dynamics and lattice dynamics calculation. The modifier was found to increase the number of free lithium ions which act as charge carriers, and also to significantly modify the host structure through the transformation of trihedrally coordinated boron atoms into tetrahedrally coordinated boron. The concentration dependence shows that this second effect goes through a maximum for  $x = 0.4$  and then decreases as a result of

the formation of  $\text{BO}_3$  groups with non-bridging oxygen atoms which carry a negative charge. Compared with the experimental data, the results of network and lattice dynamics calculations seems to give an adequate picture of the structure and vibrational response of lithium doped borate glasses.

Introduction of dopants in the form of alkali halide salts produces by dissociation an additional free lithium concentration and also a modification of the host configuration dependent on the size of the anion. Flourine enters in the network in substitutional positions forming  $\text{BO}_3\text{F}$  and  $\text{BO}_2\text{F}_2$  units. Chlorine, bromine and iodine enter interstitial positions which produces breaking of B-O-B links and formation of  $\text{BO}_4$  units. This modification of the boron oxygen network results in a less linked network facilitating the free ion diffusion. The effect is more pronounced for LiI and decreases with the anion size.

Doping with  $\text{Li}_2\text{SO}_4$  leads to analogous effects. The effect of  $\text{Li}_2\text{SO}_4$  on the Raman spectra can be understood as simply a superposition of the vibrations of the host network and that of the  $\text{SO}_4$  groups. The modifications of the host network with preferential formation of diborate groups tends to produce an expansion of the network in order to accommodate the sulfate ions and facilitate the lithium mobility.

The ion conductivity of lithium borate glasses has been addressed by developing a statistical mechanical theory of conductivity based on the assumption that the dopant behaves as a weak electrolyte which dissociates to provide free  $\text{Li}^+$  ions and high ionic conductivity. The agreement between the theoretical results and the experimental data is good for physically reason-

able values of the parameters that characterize the theory.

Taking into account the Coulomb interactions between free  $\text{Li}^+$  ions shows a distinct lowering of the conductivity, at least for relatively low temperatures. This result arises from the Coulomb interaction between free  $\text{Li}^+$  ions and the fact that at low temperatures a given  $\text{Li}^+$  ion is slowed by its interaction with its ion atmosphere.

Lithium motion in borate glasses has also been investigated by far infrared spectroscopy and analyzed on the basis of a double well model. This analysis shows that the characteristic vibrational frequencies of the  $\text{Li}^+$  ion is distributed over a large frequency range corresponding to different site configurations. The extent of the frequency distribution is a function of the free ion concentration. A drastic decrease of the damping coefficient is observed when the concentration increases.

The potential barrier regulating the motion of  $\text{Li}^+$  ions between different site configurations also increases with increasing  $\text{Li}^+$  ion concentration which corresponds to a decrease of residence frequency and increase of residence relaxation time.

In summary the experimental and theoretical results presented here gives a fairly broad and clear picture of the main features of both the matrix dynamics and the lithium free ion dynamics of lithium doped borate glasses.

## References

\*Permanent address: Laboratoire de Physique des Solides,  
Universite Pierre et Marie Curie, 4 place Jussieu, 75252  
Paris Cedex 05, FRANCE.

1. M. Balkanski, R. F. Wallis, I. Darianian and J. Deppe, Mater. Sci. Engin. B1, 15 (1988).
2. M. Massot and M. Balkanski in Festschrift for Sir R. J. Elliott edited by J. A. Blackman, Oxford University Press.
3. R. L. Mozzi and B. E. Warren, J. Appl. Crystallogr., 3 (1970) 251.
4. J. Goubeau and H. Keller, Z. Anorg. Chem. 272 (1953) 303.
5. J. Krogh-Moe, Phys. Chem. Glasses, 6 (1965) 46.
6. G. E. Jellison, Jr., L. W. Panek, P. J. Bray and G. B. Rouse, Jr., J. Chem Phys., 66 (1977) 802.
7. R. N. Sinclair, J. A. E. Desa, G. Etherington, P. A. V. Johnson and A. C. Wright, J. Non-Cryst. Solids, 42 (1980) 107.
8. F. L. Galeener, G. Lucovsky and J. C. Mikkelsen, Jr., Phys. Rev. B, 22 (1980) 3983.
9. M. H. Brodsky, in M. Cardona (ed.), Light Scattering in Solids, Springer, Berlin, 1975, p. 205.
10. L. A. Kristiansen and J. Krogh-Moe, Phys. Chem. Glasses, 10 (1968) 96.
11. F. L. Galeener, R. A. Barrio, E. Martinez and R. J. Elliott, Phys. Rev. Lett., 53 (1984) 2429.
12. F. L. Galeener and M. F. Thorpe, Phys. Rev. B23, 5802 (1983).

13. M. A. Kanehisa and R. J. Elliott, Mater. Sci. Eng. B3 163 (1989).
14. P. N. Sen and M. F. Thorpe, Phys. Rev. B15, 4030 (1977).
15. M. F. Thorpe and F. L. Galeener, Phys. Rev. B22, 3078 (1980).
16. J. Deppe, M. Balkanski and R. F. Wallis, Phys. Rev. B41, 7767 (1990).
17. W. M. Risen, Jr., J. Non-Cryst. Sol. 77-27, 97 (1985).
18. M. Massot, E. Haro, M. Oueslati and M. Balkanski, MRS Symposium Proceedings (ed. by G. Nazri, R. A. Huggins and D. F. Shriver) 135, 207, (1989).
19. P. J. Bray, S. A. Feller, J. E. Jellison, Jr. and Y. H. Yun, J. Non-Cryst. Sol. 52, 45 (1982).
20. T. W. Brill, Phillips Research Rep., Suppl. 2 (1976).
21. M. Massot, C. Julien and M. Balkanski, Infrared Phys., 25, 775 (1989).
22. D. Kline and J. P. Bray, Physics and Chemistry of Glasses 7, 41 (1966).
23. E. Cazanelli and R. Fresh, J. Chem. Phys. 79, 2615 (1983).
24. C. Julien, M. Massot, M. Balkanski, A. Krol and W. Nazarewicz, Mater. Sci. Engin. B3, 307 (1990).
25. M. Balkanski, R. F. Wallis, I. Darianian and J. Deppe, Mater. Sci. Eng. B1, 15 (1988).
26. A. B. Lidiard, Phys. Rev. 94 (1954) 29.
27. L. Pauling, The Nature of the Chemical Bond, Cornell University Press, Ithaca, NY, 2nd edn., 1940.
28. F. Seitz, Rev. Mod. Phys.. 26, 7 (1954).
29. M. Balkanski, R. F. Wallis and J. Deppe, Mater. Sci. Eng. B3,

65 (1989).

30. M. Balkanski, Spectroscopic investigations of glasses in "Science and Technology of Fast Ion Conduction," ed by H. L. Tuller and M. Balkanski, NATO ASI series (Plenum 1988).
31. P. J. Bray, J. Noncryst. Solids 73, 19 (1985).
32. W. R. Schneider and S. Strässler, Z. Phys. B27, 357 (1977).

B. Effect of Intercalated Lithium on the Direct Band  
Gaps of Indium Selenide

P. Gomes da Costa, M. Balkanski\* and R. F. Wallis

Physics Department, University of California, Irvine, CA 92717

Abstract

The effect of intercalated lithium on the  $\beta$ - and  $\gamma$ -polytypes of InSe has been investigated using a tight-binding method. The energy bands of the pure polytypes were calculated and the results compared with previous work. The tight-binding parameters associated with intercalated lithium atoms were obtained using tabulated atomic functions. The modifications of the energy bands and Fermi level produced by the introduction of one lithium atom per unit cell were calculated for the lowest potential energy position of the lithium atom in the Van der Waals gap between layers. The intercalation induced changes in the smallest and next-to-smallest direct band gaps were determined and compared with experimental data.

## 1. Introduction

The insertion of lithium into layered materials has attracted significant interest as a consequence of the possible use of such materials as electron exchange electrodes in solid state batteries. Such an application is related to the intercalation capacity and the modifications of the electronic properties of the bulk material. Intercalated InSe<sup>(1)</sup> gives a voltage of 2.6V against a lithium anode and exhibits a change in conductivity of up to two orders of magnitude.<sup>(2)</sup>

InSe is a layered material consisting of two-dimensional Se-In-In-Se layers between which the binding is weak due to the Van der Waals forces. The space between successive layers is known as a Van der Waals gap. The stacking of the layers is always compact, but there are four possible stacking arrangements leading to the four polytypes  $\beta$ ,  $\epsilon$ ,  $\gamma$ , and  $\delta$ . Only three of these polytypes ( $\beta$ ,  $\epsilon$ ,  $\gamma$ ) have been observed for InSe. Bridgeman grown crystals are generally of the type  $\gamma$ . The difference in total energy between the various polytypes is so small that one practically always finds a high density of stacking faults in a given sample.

Although most of the experimental results that have been obtained are for  $\gamma$ -InSe, no band structure calculations are available in the literature for this polytype. All existing calculations are for the  $\beta$  and  $\epsilon$  polytypes which have a simpler first Brillouin zone. The first band structure calculation for this family of materials was made for GaSe.<sup>(3)</sup> A calculation for InSe within a tight-binding model has been carried out in a two-

dimensional approximation.<sup>(4)</sup> Extensions to the three-dimensional case have been developed using the pseudopotential method<sup>(5)</sup> and the tight-binding method.<sup>(6)</sup> Including the spin-orbit interaction in the tight-binding calculation<sup>(7)</sup> has a non-negligible effect on the InSe band structure. Pseudopotential calculations for  $\epsilon$ -InSe are also available,<sup>(8)</sup> but without spin-orbit interaction.

Lithium insertion<sup>(9,10)</sup> in InSe has been shown to affect both the electronic and optical properties. Possible interstitial sites for Li atoms in  $\gamma$ -InSe have been discussed and their relative energies determined.<sup>(11)</sup> Lithium diffusion paths<sup>(12)</sup> in  $\gamma$ -InSe have also been determined by ab initio calculations.

Lithium insertion<sup>(9,10)</sup> in InSe has been shown to affect both the electronic and optical properties. Possible interstitial sites for Li atoms in  $\gamma$ -InSe have been discussed and their relative energies determined.<sup>(11)</sup> Lithium diffusion paths<sup>(12)</sup> in  $\gamma$ -InSe have also been determined by ab initio calculations.

The optical properties near the band edges of pure InSe have been investigated and compared with the calculated band structure.<sup>(7)</sup> Sharp excitonic peaks are observed in the absorption spectrum at low temperature corresponding to the three absorption thresholds. The first threshold at 1.3 eV is related to the direct absorption between the  $s$ ,  $p_z$  valence band states and  $s$  conduction band states. The second at 2.5 eV is related to transitions from  $p_x$ ,  $p_y$  valence band states to  $s$  conduction band

states, and the third at 2.9 eV is related to transitions from the spin-orbit split-off valence band to the s conduction band. More recent results<sup>(13)</sup> on pure InSe at 10K with the electric vector of the radiation perpendicular to the c-axis allow one to distinguish the  $n=1$  and  $n=2$  excitonic transitions as well as the LO phonon replicas of the  $n=1$  excitonic state.

The effect of Li insertion on the interband optical absorption peaks is rather weak, but nevertheless, clearly observable. In Fig. 1 are shown the shifts in frequency of the smallest direct band gap  $E_1$  and the next-to-smallest band gap  $E_2$  as functions of the lithium content.<sup>(10)</sup> We see that the  $E_1$  gap increases in frequency as the Li concentration increases, whereas the  $E_2$  gap decreases in frequency.

The excitonic transitions persist after Li insertion, which suggests that all of the Li 2s electrons do not transfer to the conduction band and thus transform the semiconducting InSe into a metal.<sup>(14,15)</sup> If we had a metallic transition, the Coulomb interaction between the electron and hole of the exciton would be screened and the excitonic state would be washed out. The persistence of the excitonic transitions in highly intercalated InSe suggests that the Li 2s electrons form a low mobility impurity band or are efficiently trapped into localized states.

The photoluminescence spectrum of InSe is significantly modified by the intercalation of Li. A new photoluminescence peak appears at a photon energy somewhat less than that of the fundamental exciton peak of pure InSe as shown in Fig. 2. This new peak may be associated with the Li-2s band lying in the

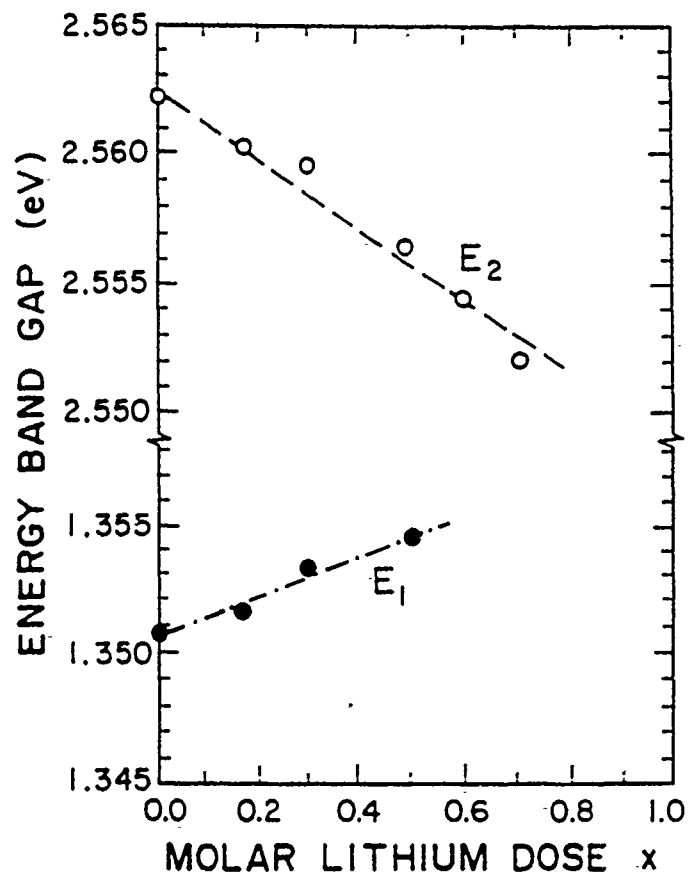


FIG. 1. Energy gap vs lithium content  $x$  in  $\text{Li}_x\text{InSe}$  for the smallest and next-to-smallest energy gaps  $E_1$  and  $E_2$  at 5 K.

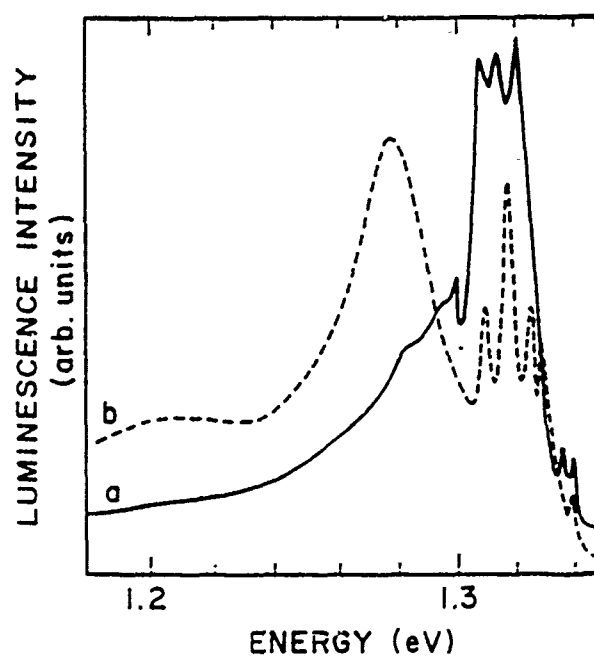


FIG. 2. Photoluminescence spectra for  $\gamma$ -InSe before (a) and after (b) lithium intercalation at 5 K under 1.916 eV excitation by a  $\text{Kr}^+$  laser.

fundamental gap of InSe.

### Theoretical Development

We have developed a tight-binding scheme for calculating the electronic band structure of both  $\beta$ - and  $\gamma$ -InSe. Our procedure is based on the overlap-reduced semi-empirical tight-binding method of Doni et al.<sup>(16)</sup> who considered the case of  $\beta$ -InSe. The Slater-Koster procedure<sup>(17)</sup> was used to express the overlap and interaction integrals of the tight binding method in terms of the basic overlap integrals  $S_{ij}$  and interaction integrals  $V_{ij}$ . Only two-center integrals were considered.

For  $\beta$ -InSe we took the values of the parameters  $S_{ij}$  and  $V_{ij}$  from the tabulation in Doni et al. for the nearest-neighbor In-In, In-Se, and Se-Se interactions both parallel and perpendicular to the c-axis. The atomic states considered are Se 4s and 4p and In 5s and 5p whose energies were taken from Doni et al. We also used the crystal field parameters K tabulated by Doni et al. Interactions beyond nearest neighbors were included by scaling the Doni parameters with a factor  $d^{-2}$  where d is the interatomic distance of the interacting atoms. The interactions were cut off at  $d=8.77\text{\AA}$ .

The structure of  $\gamma$ -InSe is simpler than that of  $\beta$ -InSe, because the former has only four atoms per unit cell, whereas the latter has eight atoms. The difference in structure arises from the difference in stacking of successive layers; the interatomic distances within a layer are essentially the same in both polytypes. In view of these similarities, we have taken the basic overlap and interaction parameters for  $\gamma$ -InSe to be the same as

those given by Doni et al. with the exception of the interlayer parameters  $S_{\text{Se-Se}}(\text{pp}\sigma)$  and  $\bar{V}_{\text{Se-Se}}(\text{pp}\sigma)$ . These parameters together with the crystal field parameters  $K(\text{In } 5s)$ ,  $K(\text{Se } p_x)$ ,  $K(\text{Se } p_y)$ , and  $K(\text{Se } p_z)$  were varied in order to reproduce the experimental values of the smallest band gap  $E_1$  and the next-to-smallest band gap  $E_2$ . The values thus obtained are tabulated in Table I.

Having established the tight-binding scheme for the pure  $\beta$ - and  $\gamma$ -polytypes of InSe, we then proceeded to generalize the scheme to include the presence of intercalated Li atoms. We assume that the Li atoms occupy the sites of lowest potential energy<sup>(12)</sup> (the  $A_{3-2}$  sites) in the Van der Waals gap between layers. Since intercalation of lithium leads to only a very small increase in the interlayer spacing, we have neglected any change in the tight-binding parameters of InSe itself. The overlap and interaction parameter for the interaction of a Li atom with the nearest Se and In atoms were calculated using the tabulated atomic functions of Clementi and Roetti.<sup>(18)</sup> The electronic band structure of the intercalated InSe was then obtained by diagonalizing the Hamiltonian matrix. The changes in the  $E_1$  and  $E_2$  gaps thus obtained turned out to be large. The Li parameters were then varied until agreement was achieved between the theoretical and experimental gaps. The resultant values for the Li parameters are listed in Table II.

### Numerical Results

The electronic band structure of pure  $\gamma$ -InSe which we have obtained is shown in Fig. 3 for various directions in the first

TABLE I. Values of the tight-binding parameters for  $\gamma$ -InSe. The notation is that of Ref. 16.  $\bar{V}$  and  $J$  are in Rydbergs.

Se-Se interlayer parameters		crystal field parameters	
$S(pp\sigma)$	-0.010	$K(\text{Se } 4p_x)$	0.0203
$\bar{V}(pp\sigma)$	0.002	$K(\text{Se } 4p_z)$	0.1143
		$K(\text{In } 5s)$	-0.0373

TABLE II. Values of the tight-binding parameters for lithium-intercalated  $\gamma$ -InSe.  $\bar{V}$  and  $K$  are in Rydbergs.

	$S$	$\bar{V}$	$K$
Li-Se ( $ss\sigma$ )	0.02636	-0.000318	
Li-Se ( $sp\sigma$ )	-0.0077	0.0027	
Li-In ( $ss\sigma$ )	0.004143	-0.000313	
Li-In ( $sp\sigma$ )	-0.04665	0.000669	
Li ( $2s$ )			-0.066

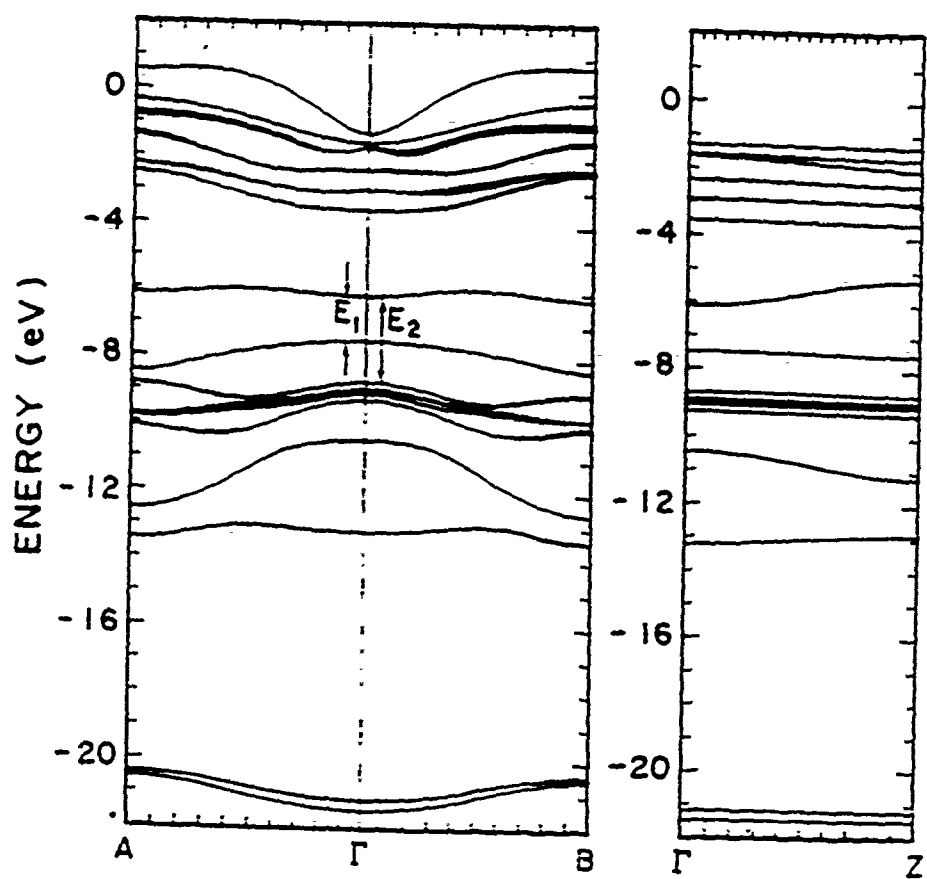


FIG. 3. Energy bands for pure  $\gamma$ -InSe.

Brillouin zone. The smallest direct gap ( $E_1$ ) occurs at  $\Gamma$  between the  $s$ ,  $p_z$  valence band and the  $s$  conduction band. The next lower direct gap ( $E_2$ ) occurs at  $\Gamma$  between the  $p_x$ ,  $p_y$  valence band and the  $s$  conduction band.

For the case of pure  $\beta$ -InSe, we plot our results for the band structure in Fig. 4.: These results are very similar to those of Doni et al. In particular, both sets of results give an indirect gap between  $\Gamma$  and M that is somewhat smaller than the direct  $E_1$  gap at  $\Gamma$ .

In Fig. 5 we present the band structure for lithium-intercalated  $\gamma$ -InSe with the composition  $\text{Li}_{0.5}\text{InSe}$  and the Li atoms occupying the  $A_{3-2}$  sites in the Van der Waals gap between layers. The band associated with the Li 2s state is seen to lie just below the conduction band edge. The effect of the intercalated lithium on the InSe bands is too small to be observable on the scale of the figure. However, the effects on the  $E_1$  and  $E_2$  gaps are revealed by the numerical results given in Table III. The excellent agreement between the experimental and theoretical values is a direct consequence of the choice of the Li parameters.

The occurrence of the Li-2s band in the fundamental gap of InSe provides a natural explanation for the new photoluminescence peak produced by Li insertion. Excitation with photons having energy greater than the band gap creates electron-hole pairs. An

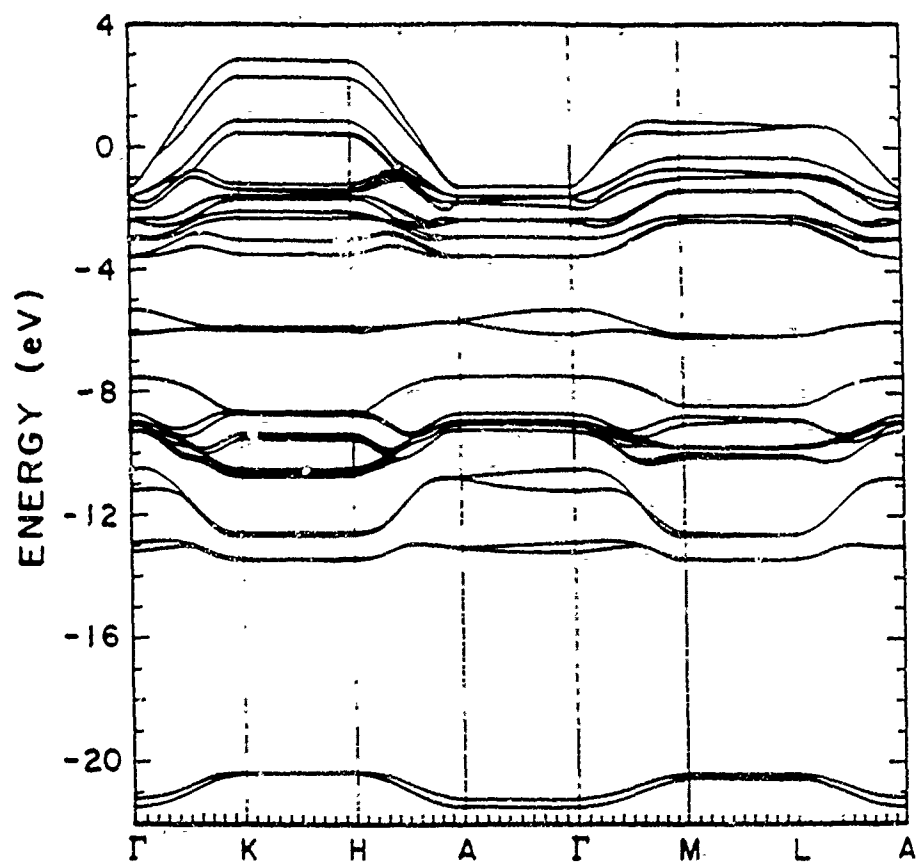


FIG. 4. Energy bands for pure  $\beta$ -InSe.

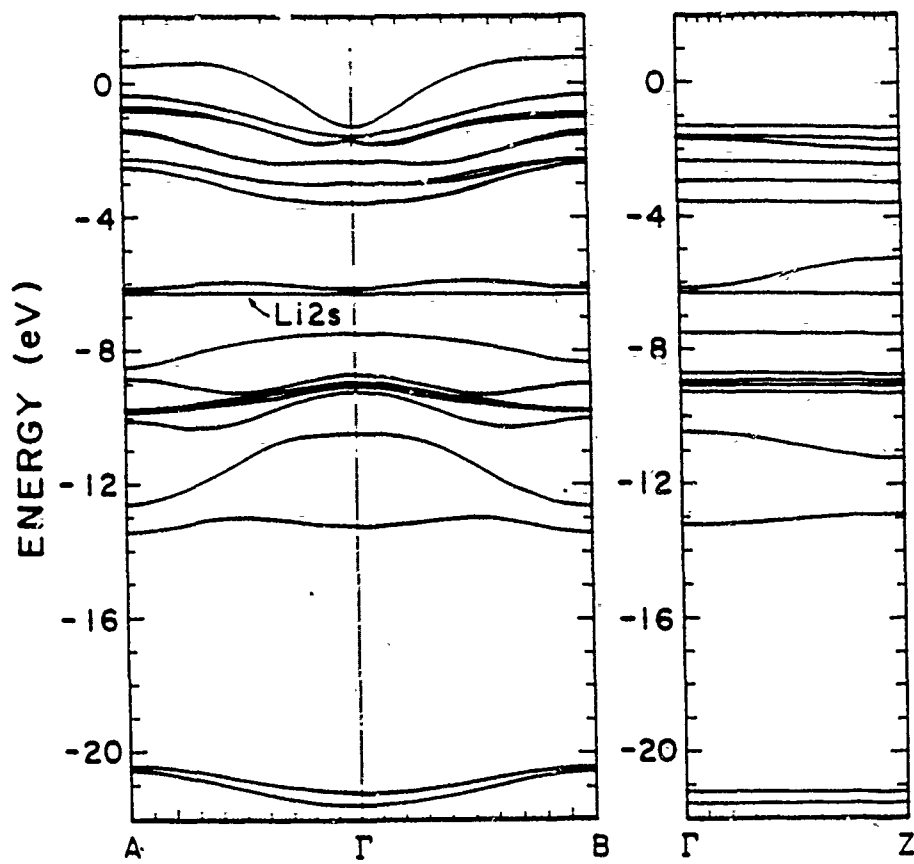


FIG. 5. Energy bands for lithium-intercalated  $\gamma$ -InSe with the composition  $\text{Li}_{0.5}\text{InSe}$ . The gap between the Li 2s band and the conduction band just above it is 0.036 eV at  $\Gamma$ , but is exaggerated for clarity.

Table III. Values of the  $E_1$  and  $E_2$  energy gaps with and without lithium intercalation in  $\gamma$ -InSe.

	pure $\gamma$ -InSe	lithium-intercalated $\gamma$ -InSe
$E_1$	1.3335 eV	1.3368 eV
$E_2$	2.5451	2.539

electron in the Li-2s band can then recombine with a hole accompanied by the emission of a photon whose energy is equal to the difference between the valence band edge and the lower edge of the Li-2s band.

### Conclusions

A tight-binding scheme has been developed for pure  $\beta$ -InSe and  $\gamma$ -InSe using the overlap-reduced semi-empirical method the procedure satisfactorily accounts for the direct energy gaps of the two polytypes. The tight-binding scheme has been generalized to include the effect of intercalated lithium atoms. The shifts in the direct gaps and the appearance of a new peak in the photoluminescence spectrum predicted by the calculations are in agreement with experimental optical data.

### References

1. M. Balkanski, C. Julien, and J. Y. Emery, J. Power Sources 26, 615 (1989).
2. E. Hatzikraniotis, C. Julien, and M. Balkanski, NATO ASI Series E101, Martimes Nijhoff Publ., Amsterdam, 1985.
3. M. Schlüter, Il Nuovo Cimento B13(2), 313 (1973).
4. J. V. McCanny and R. B. Murray, J. Phys. C10, 1211 (1977).
5. A. Bourdon, A. Chevy, and J. M. Besson, Inst. Phys. Conf. Ser. N43, 1371 (1979).
6. J. Robertson, J. Phys. C12 4777 (1979).
7. M. Placentini, E. Doni, R. Girlanda, V. Grasso, and A. Balzarotti, Il Nuovo Cimento B54(1) 269 (1979).
8. Y. Depeursinge, Il Nuovo Cimento B64(1), 111 (1982).

9. C. Julien, E. Hatzikraniotis, K. M. Paraskevopoulos, A. Chevy, and M. Balkanski, Solid State Ionics 18-19, 859 (1986).
10. M. Balkanski, C. Julien, and M. Jouanne, J. Power Sources 20, 213 (1987).
11. K. Kunc, R. Zeyher, and E. Molinari, Proc. 19th Int. Conf. Phys. Semiconductors, Warsaw, 1988.
12. K. Kunc and R. Zeyher, Europhys. Lett. 7, 611 (1988).
13. P. A. Burret, Thesis, Paris, 1989.
14. C. Julien, M. Jouanne, P. A. Burret, and M. Balkanski, Solid State Ionics, 28-30, 1167 (1988).
15. M. Jouanne, C. Julien, R. Beserman, and M. Balkanski, Phys. Scripta 38, 471 (1988).
16. E. Doni, R. Girlanda, V. Grasso, A. Balzarotti, and M. Piacentini, Il Nuovo Cimento B51 (1), 154 (1979).
17. J. C. Slater and G. F. Koster, Phys. Rev. 94, 1498 (1954).
18. E. Clementi and C. Roetti, Atomic Data and Nuclear Data bles 14, 177 (1974).

C. Lattice Dynamics of  $\gamma$ -InSe Containing  
Intercalated Lithium

P. Gomes da Costa, M. Balkanski,\* and R. F. Wallis  
Department of Physics and Institute for Surface and  
Interface Science  
University of California, Irvine, CA 92717

ABSTRACT

The lattice dynamics of the  $\gamma$ -polytype of the layer compound InSe has been investigated using a model containing short-range central forces and long-range Coulomb interactions. The normal mode frequencies and eigenvectors were determined by diagonalizing the dynamical matrix. The results have been correlated with the infrared and Raman spectra of  $\gamma$ -InSe. The effect of intercalated lithium atoms on the vibrational modes has been investigated both theoretically and with the aid of Raman spectra.

1. INTRODUCTION

In a number of solid state batteries currently under investigation, layered materials are used as electron exchange electrodes, since they can accommodate considerable amounts of intercalated lithium. For such an application it is essential that the electrode material have a sufficiently high ionic as well as electronic conductivity. A material that satisfies these requirements is InSe which can intercalate relatively large amounts of lithium with only a slight expansion of its lattice [1,2].

InSe is a layered compound having complex layers in which atomic layers of Se, In, In, and Se are bound together

by covalent bonds with some ionic character. These complex layers are themselves bound to one another by weak Van der Waals interactions with a so-called Van der Waals gap between layers. There are four possible stacking arrangements of the complex layers leading to four polytypes designated  $\beta, \epsilon, \gamma$ , and  $\delta$ . Since the experimental results to be discussed are for the  $\gamma$ -polytype, we shall focus our attention on this polytype.

A microscopic understanding of both the electronic and ionic conductivity of lithium-intercalated  $\gamma$ -InSe requires a knowledge of the lattice dynamics of this system. Of particular importance is information concerning the forces of interaction between intercalated lithium atoms and nearby selenium and indium atoms.

In this paper we present the results of a theoretical investigation of the lattice dynamics of  $\gamma$ -InSe both with and without intercalated lithium. We develop the lattice dynamical model in section 2. The values of the force constants and calculated phonon dispersion curves for pure  $\gamma$ -InSe are presented in section 3. Similar results are presented in section 4 for lithium intercalated  $\gamma$ -InSe. Conclusions are presented in section 5.

## 2. LATTICE DYNAMICAL MODEL

The first step in setting up the lattice dynamical model is to summarize the pertinent information concerning the structure of InSe. The  $\gamma$ -polytype belongs to the trigonal system, and its space group is  $C_{3v}^5$ . The primitive translation vectors can be written as [3]

$$\vec{t}_1 = (\sqrt{3}/3)a_0\vec{i} + c_0\vec{k} \quad (1a)$$

$$\vec{i}_2 = -(\sqrt{3}/6)a_0\vec{i} + (1/2)a_0\vec{j} + c_0\vec{k} \quad (1b)$$

$$\vec{i}_3 = -(\sqrt{3}/6)a_0\vec{i} - (1/2)a_0\vec{j} + c_0\vec{k} \quad (1c)$$

where  $a_0$  is the lattice constant parallel to the layers,  $c_0$  is the lattice constant perpendicular to the layers, and  $\vec{i}, \vec{j}, \vec{k}$  are unit vectors in the  $x, y, z$  directions, respectively. The values of  $a_0$  and  $c_0$  are [4] 4.00 Å and 8.44 Å respectively.

The primitive translation vectors of the reciprocal lattice can be obtained from  $\vec{i}_1, \vec{i}_2, \vec{i}_3$  and are found to be

$$\vec{b}_1 = 2\pi[(2/\sqrt{3}a_0)\vec{i} + (1/3c_0)\vec{k}] \quad (2a)$$

$$\vec{b}_2 = 2\pi[-(1/\sqrt{3}a_0)\vec{i} + (1/a_0)\vec{j} + (1/3c_0)\vec{k}] \quad (2b)$$

$$\vec{b}_3 = 2\pi[-(1/\sqrt{3}a_0)\vec{i} - (1/a_0)\vec{j} + (1/3c_0)\vec{k}] \quad (2c)$$

Diagrams of the stacking of the layers of  $\gamma$ -InSe and its first Brillouin zone are shown in Fig. 1.

Since InSe is a polar semiconductor, the chemical bonds which bind neighboring atoms together have both covalent and ionic character. The interatomic forces should, therefore, have a short-range part associated with the covalent character of the bonds and a long-range Coulomb part associated with the ionic character of the bonds. We therefore write an element of the force constant matrix  $\Phi_{\alpha\beta}(l\kappa; l'\kappa')$  as the sum of two contributions,

$$\Phi_{\alpha\beta}(l\kappa; l'\kappa') = \Phi_{\alpha\beta}^C(l\kappa; l'\kappa') + \Phi_{\alpha\beta}^N(l\kappa; l'\kappa') \quad (3)$$

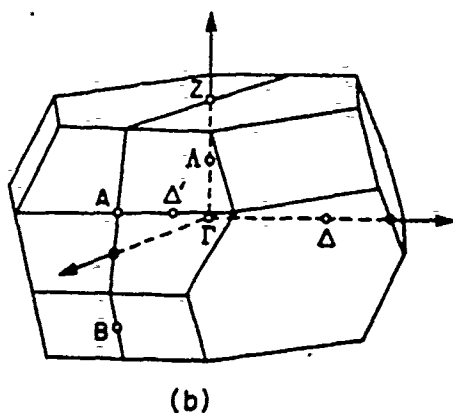
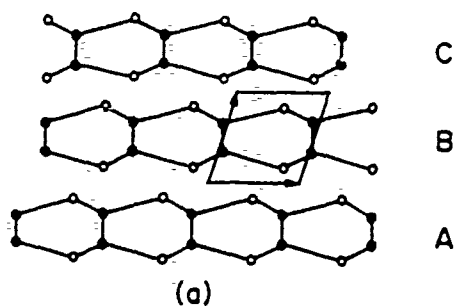


Fig. 1 (a) Stacking of layers and (b) first Brillouin zone of  $\gamma$ -InSe. In (a) the open circles are Se atoms and the closed circles are In atoms.

where  $\Phi_{\alpha\beta}^C(lk;l'\kappa')$  is the contribution from the long-range Coulomb interactions,  $\Phi_{\alpha\beta}^N(lk;l'\kappa')$  is the contribution from short-range non-Coulomb interactions, the index pair  $lk$  designates the  $\kappa$ th atom in the  $l$ th unit cell, and  $\alpha, \beta$  denote Cartesian coordinate components.

For the non-Coulomb interactions we adopted the central-potential model which Polian [5] found satisfactory for the related material GaS. With a central potential  $\varphi(r)$  dependent only on the distance  $r$  between the interacting atoms, one can write the contribution to  $\Phi_{\alpha\beta}^N(lk;l'\kappa')$  for  $lk \neq l'\kappa'$  in the form

$$\Phi_{\alpha\beta}^N(l\kappa; l'\kappa') = -\varphi_{\alpha\beta}(l\kappa; l'\kappa') \quad (4)$$

where

$$\varphi_{\alpha\beta}(l\kappa; l'\kappa') = \left\{ \frac{x_\alpha x_\beta}{r^2} \varphi''_{\kappa\kappa'}(r) - \frac{1}{r} \varphi'_{\kappa\kappa'}(r) \right\} + \frac{\delta_{\alpha\beta}}{r} \varphi'_{\kappa\kappa'}(r) \Big|_{r=|\bar{x}(l\kappa; l'\kappa')|} \quad (5)$$

$$\bar{x}(l\kappa; l'\kappa') = \bar{x}(l\kappa) - \bar{x}(l'\kappa') \quad (6)$$

$\bar{x}(l\kappa)$  is the position vector of atom  $l\kappa$  in the equilibrium configuration, and primes denote differentiation with respect to argument. A given interaction consequently involves two force constant parameters,  $\varphi''_{\kappa\kappa'}(r)$  and  $\varphi'_{\kappa\kappa'}(r)/r$ , which will henceforth be designated by A and B, respectively.

The short-range model employed includes the following interactions:

1. In-In first neighbors
2. In-Se first neighbors
3. Se-Se interlayer
4. In-In second neighbors
5. In-Se second neighbors

The corresponding values of A and B are designated by  $A_i$ ,  $B_i$  with  $i = 1, 2, 3, 4, 5$ .

The long-range Coulomb interactions are characterized by the effective charges of the In and Se ions. Since the In-Se bond is partly ionic and partly covalent, we expect the magnitudes of the effective charges to be less than the magnitude of the electron charge. From the symmetry and stoichiometry of  $\gamma$ -InSe and electroneutrality, we conclude that the effective charges of the In and Se ions are equal in magnitude and opposite in sign. The large anisotropy of

the crystal leads us to introduce a tensorial effective charge of the form [5]

$$z^*e = \begin{bmatrix} z_1^* & 0 & 0 \\ 0 & z_1^* & 0 \\ 0 & 0 & z_2^* \end{bmatrix} e \quad (7)$$

This form for the effective charge accounts for the fact that the polarization produced by displacements parallel to the layers is different from that produced by displacements perpendicular to the layers.

The contribution of the long-range Coulomb interactions to the force constant matrix was evaluated using the Ewald technique by expressing the elements of this matrix in terms of a sum over the direct lattice and a sum over the reciprocal lattice. The elements of the Coulomb contribution to the dynamical matrix  $D_{\alpha\beta}^C(\vec{k}; \kappa\kappa')$  were then obtained using the relation

$$D_{\alpha\beta}^C(\vec{k}; \kappa\kappa') = \frac{1}{\sqrt{M_\kappa M_{\kappa'}}} \sum_l \Phi_{\alpha\beta}^C(l\kappa, l'\kappa') e^{-i\vec{k} \cdot [\vec{z}(l\kappa) - \vec{z}(l'\kappa')]} \quad (8)$$

where  $M_\kappa$  is the mass of atom  $\kappa$ . The contribution of the sum over the direct lattice to  $D_{\alpha\beta}^C(\vec{k}; \kappa\kappa')$  is given by

$$D_{\alpha\beta}^C(\vec{k}; \kappa\kappa')_d = -\frac{e_{\kappa\alpha} e_{\kappa'\beta}}{\sqrt{M_\kappa M_{\kappa'}}} \eta^3 \sum_l e^{-i\vec{k} \cdot [\vec{z}(l\kappa) - \vec{z}(l'\kappa')]} H_{\alpha\beta}[\zeta(l; \kappa\kappa')] \\ + \frac{\delta_{\kappa\kappa'}}{M_\kappa} \eta^3 \sum_{\kappa''} e_{\kappa''} e_{\kappa'} \sum_l H_{\alpha\beta}[\zeta(l; \kappa\kappa'')] \quad (9)$$

where  $e_{\kappa\alpha}$  is the effective charge component of ion  $\kappa$  given by  $z_{\kappa\alpha}^* e$ ,  $\eta$  was taken to have the value  $\sqrt{\pi}/r_0$ ,  $r_0$  is the equilibrium nearest-neighbor separation,

$$\zeta(l; \kappa\kappa') = \eta |\bar{x}(\kappa) - \bar{x}(l\kappa')| \quad (10)$$

and

$$H_{\alpha\beta}[\zeta(l; \kappa\kappa')] \equiv H_{\alpha\beta}(\zeta)$$

$$= \frac{\zeta_\alpha \zeta_\beta}{\zeta^2} \left[ \frac{3}{\zeta^3} \text{Erfc}(\zeta) + \frac{2}{\sqrt{\pi}} \left( \frac{3}{\zeta^2} + 2 \right) e^{-\zeta^2} \right]$$

$$- \delta_{\alpha\beta} \left[ \frac{1}{\zeta^3} \text{Erfc}(\zeta) + \frac{2}{\sqrt{\pi} \zeta^2} e^{-\zeta^2} \right] \quad (11)$$

The reduced effective charge components  $z_{I\alpha\alpha}^*$  and  $z_{Se\alpha}^*$  satisfy  $z_{Se\alpha}^* = -z_{I\alpha\alpha}^* = z_\alpha^*$  with  $z_\alpha^*$  specified by Eq. (7) -- i.e.,  $z_x^* = z_y^* = z_1^*$  and  $z_z^* = z_2^*$ .

The contribution of the sum over the reciprocal lattice to  $D_{\alpha\beta}^c(\vec{k}; \kappa\kappa')$  is given by

$$D_{\alpha\beta}^c(\vec{k}; \kappa\kappa')_r = \frac{4\pi}{v_a} \left\{ \frac{e_{\kappa\alpha} e_{\kappa'\beta}}{\sqrt{M_\kappa M_{\kappa'}}} \left[ \frac{k_\alpha k_\beta}{k^2} e^{-k^2/4\eta^2} \right. \right. \\ \left. \left. + \sum_{\vec{G} \neq 0} \frac{(G_\alpha + k_\alpha)(G_\beta + k_\beta)}{|\vec{G} + \vec{k}|^2} e^{-|\vec{G} + \vec{k}|^2/4\eta^2} e^{i\vec{G} \cdot [\bar{x}(\kappa) - \bar{x}(\kappa')]} \right] \right\}$$

$$-\delta_{\kappa\kappa'} \frac{e_{\kappa\kappa'}}{M_{\kappa}} \sum_{\beta} e_{\kappa'\beta} \sum_{\vec{G} \neq 0} \frac{G_{\alpha} G_{\beta}}{|\vec{G}|^2} e^{-|\vec{G}|^2/4\eta^2} e^{i\vec{G} \cdot [\vec{z}(\kappa) - \vec{z}(\kappa')]} \quad (12)$$

where the reciprocal lattice vectors  $\vec{G}$  are given by

$$\vec{G} = m_1 \vec{b}_1 + m_2 \vec{b}_2 + m_3 \vec{b}_3 \quad (13)$$

and  $m_1, m_2, m_3$  are integers.

The full Coulomb contribution to the dynamical matrix is given by

$$D_{\alpha\beta}^C(\vec{k}; \kappa\kappa') = D_{\alpha\beta}^C(\vec{k}; \kappa\kappa')_d + D_{\alpha\beta}^C(\vec{k}; \kappa\kappa')_l \quad (14)$$

Adding this result to the short-range contribution to the dynamical matrix  $D_{\alpha\beta}^N(\vec{k}; \kappa\kappa')$ , where

$$D_{\alpha\beta}^N(\vec{k}; \kappa\kappa') = \frac{1}{\sqrt{M_{\kappa} M_{\kappa'}}} \sum_{\vec{r}} \Phi_{\alpha\beta}^N(l\kappa, l'\kappa') e^{-i\vec{k} \cdot [\vec{z}(l\kappa) - \vec{z}(l'\kappa')]} \quad (15)$$

yields the full dynamical matrix  $D_{\alpha\beta}(\vec{k}; \kappa\kappa')$ :

$$D_{\alpha\beta}(\vec{k}; \kappa\kappa') = D_{\alpha\beta}^C(\vec{k}; \kappa\kappa') + D_{\alpha\beta}^N(\vec{k}; \kappa\kappa') \quad (16)$$

The normal mode frequencies and eigenvectors were obtained by diagonalizing the full dynamical matrix.

### 3. MODEL PARAMETERS AND PHONON DISPERSION CURVES FOR PURE $\gamma$ -InSe

The central potential model which we employ contains twelve parameters to be determined:  $A_1, \dots, A_5, B_1, \dots, B_5, z_1, z_2$ . The experimental data that are available for  $\gamma$ -InSe,

namely, infrared and Raman spectra, are insufficient to make a unique determination of these parameters. We have

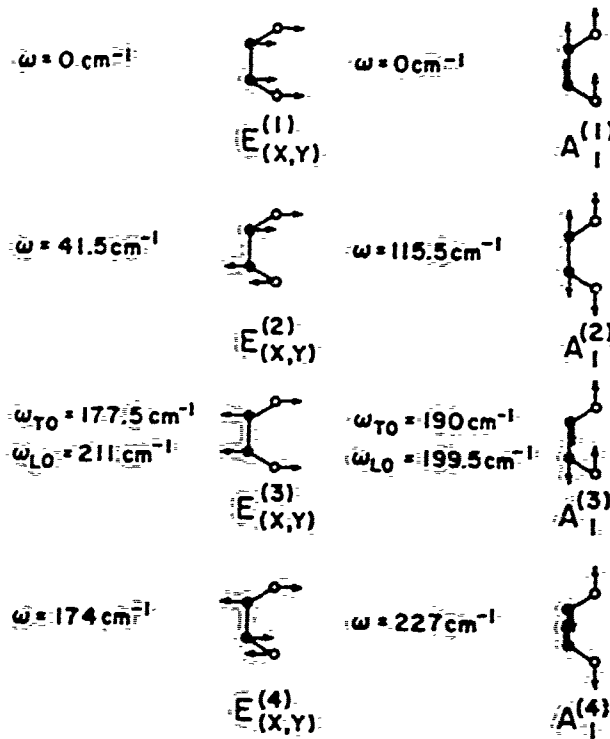


Fig. 2 Zone center normal modes and their corresponding frequencies for pure  $\gamma$ -InSe.

therefore taken as a starting point the values of the corresponding parameters for GaS obtained by Polian [5] by fitting phonon dispersion curves (determined by inelastic neutron scattering), elastic constants, and infrared and Raman data. We then fine-tuned the values of the parameters by adjusting them to reproduce the frequencies and polarizations of the optical modes of long wavelength derived from infrared and Raman data for  $\gamma$ -InSe [6] which are presented in Fig. 2. The values of the model parameters thus determined are given in Table 1.

Table 1. Short-range and Coulomb parameters for  $\gamma$ -InSe.  
The units for the A and B parameters are N/m.

i	1	2	3	4	5
A <sub>i</sub>	78.35	32.17	0.5	7.0	3.4
B <sub>i</sub>	4.65	31.0	-0.196	-8.584	0.9
z <sub>i</sub> <sup>*</sup>	0.71	0.43	---	---	---

The elements of the dynamical matrix were next evaluated using the tabulated values of the model parameters. Diagonalization of the dynamical matrix for various values of the wave vector  $\vec{k}$  yielded the normal mode frequencies and eigenvectors. The dispersion curves were constructed for several high symmetry directions in the Brillouin zone and are presented in Fig. 3. Since there are four atoms per primitive unit cell in  $\gamma$ -InSe, there are

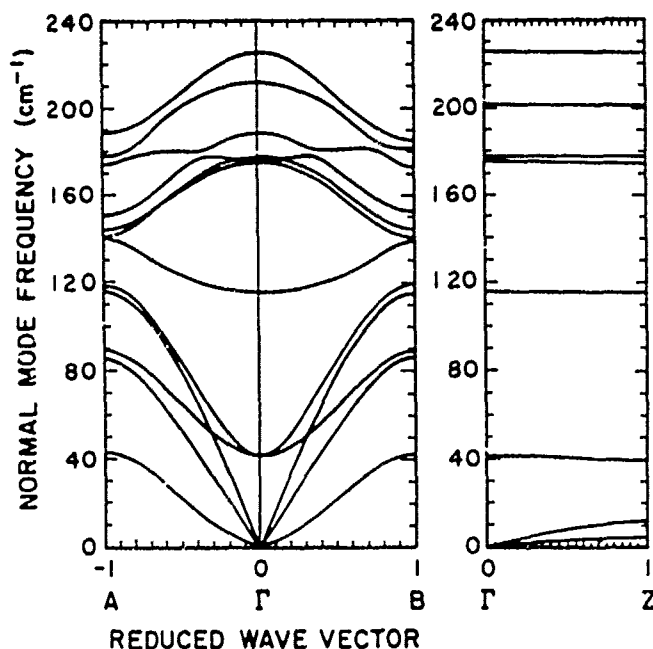


Fig. 3 Phonon dispersion curves for pure  $\gamma$ -InSe.

twelve normal modes for a given value of  $\vec{k}$ . There is considerable dispersion of the normal modes propagating in directions not perpendicular to the layers as a consequence of the strong intra-layer binding of the atoms. However, the weak interlayer binding (note the small values of  $A_3$  and  $B_3$  in Table 1) leads to nearly flat dispersion curves in the direction perpendicular to the layers, as evident in Fig. 3 for the  $\Gamma Z$  direction.

#### 4. MODEL PARAMETERS AND PHONON DISPERSION CURVES FOR LITHIUM INTERCALATED $\gamma$ -InSe

The intercalation of lithium into  $\gamma$ -InSe leads to new peaks [6] in the Raman spectrum at  $92 \text{ cm}^{-1}$  and  $388 \text{ cm}^{-1}$ . In addition, peaks associated with pure  $\gamma$ -InSe are modified by plasmon-phonon coupling [6]. We have made a theoretical investigation of the case in which there is one lithium atom per primitive unit cell and that atom occupies a site of lowest potential energy (A3-2 site [7]) in the Van der Waals gap between layers. We assume that there are central potential interactions between the lithium atom and the nearest selenium and indium atoms with interaction parameters  $A_6, B_6$  and  $A_7, B_7$ , respectively. Since we have only two new normal mode frequencies and since  $B$  is typically small compared to  $A$ , we have neglected  $B_6$  and  $B_7$  and determined  $A_6$  and  $A_7$  by associating the frequencies  $92 \text{ cm}^{-1}$  and  $388 \text{ cm}^{-1}$  with normal modes dominated by lithium atom motion parallel and perpendicular to the layers, respectively. The resulting values for  $A_6$  and  $A_7$  are  $1.61 \text{ N/m}$  and  $54.8 \text{ N/m}$ , respectively. The large value of  $A_7$  relative to that of  $A_6$  is consistent with the facts that the indium atomic radius ( $0.76\text{\AA}$ ) is larger than that of selenium ( $0.60\text{\AA}$ ) [8] and that a lithium atom in the A3-2 site lies

directly above the indium atom to which it is coupled. The restoring force on the lithium atom is therefore dominated by  $A_7$  in the mode in which the lithium atom moves perpendicular to the layers ( $\omega=388 \text{ cm}^{-1}$ ) and by  $A_6$  in the mode in which the lithium atom moves parallel to the layers ( $\omega=92 \text{ cm}^{-1}$ .)

After incorporating the force constants  $A_6$  and  $A_7$  into the dynamical matrix, we calculated the normal mode frequencies and eigenvectors as functions of the wave vector  $\vec{k}$  for  $\text{Li}_{0.5} \text{InSe}$ . The dispersion curves thus obtained are plotted in Fig. 4. We note that the normal modes primarily

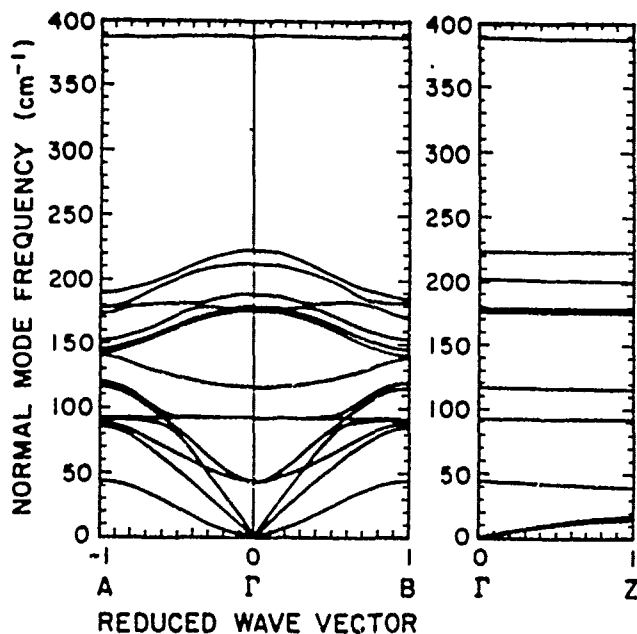


Fig. 4 Phonon dispersion curves for lithium intercalated  $\gamma$ -InSe.

associated with the InSe lattice are little affected by the presence of the lithium, since the mass of a lithium atom is much smaller than those of indium and selenium atoms. The normal modes primarily associated with lithium atom motion at  $92\text{ cm}^{-1}$  and  $388\text{ cm}^{-1}$  are essentially flat as a result of the weak Li-Se coupling and the lack of coupling between lithium atoms in different unit cells.

## 5. CONCLUSIONS

A lattice dynamical model has been developed for both pure and lithium-doped  $\gamma$ -InSe. The model contains short-range and Coulomb interactions. Phonon dispersion curves have been calculated for both the intercalated and non-intercalated cases. The results are consistent with observed infrared and Raman data.

## REFERENCES

\*Permanent address: Laboratoire de Physique des Solides,  
Université Pierre et Marie Curie, 4 place Jussieu, 75252  
Paris Cédex 05, France.

1. Julien, C. Hatzikraniotis, E. Paraskevopoulos, K. M.,  
Chevy, A. and Balkanski, M., Solid State Ionics 18/19,  
859 (1986).
2. Balkanski, M., Julien, C. and Emery, J. Y., J. Power  
Sources 26, 615 (1989).
3. Slater, J. C., "Quantum Theory of Molecules and Solids"  
(McGraw-Hill, New York, 1965).
4. Doni, E., Girlanda, R., Grasso, V., Balzaroti, A. and  
Piacentini, M., Il Nuovo Cimento 51 B(1), 154 (1979).
5. Polian, A., Thèse de Doctorat d'Etat, Université Pierre  
et Marie Curie, Paris, 1981.
6. Burret, P. A., Thèse de Doctorat de l'Université Pierre  
et Marie Curie, Paris, 1989.
7. Kunc, K. and Zeyher, R., Europhys. Lett. 7, 611 (1988).
8. Pauling, L., "The Nature of the Chemical Bond" (Cornell  
University Press, Ithaca, 1940).

d. Molecular Dynamics Study of the Lattice Vibration  
Contribution to the Frequency-Dependent Dielectric Constant  
of Lithium Iodide

J. Deppe\*, M. Balkanski\*\*, R. F. Wallis and A. R. McGurn†  
Physics Department, University of California, Irvine  
Irvine, California 92717

**Abstract**

A molecular dynamics simulation has been performed on the crystal lithium iodide, *LiI*. A rigid ion potential is used with parameters fit to thermal expansion, isothermal compressibility, lattice energy and the frequency of the transverse optical mode at the zone center. The current-current correlation function has been calculated at  $T = 200K$  and  $400K$ , and from this the absorption and dispersion have been obtained. Anharmonic broadening is observed at the higher temperature. In addition, the mean square displacements of the two ions, and the radial distribution function are calculated.

## 1. Introduction

Lattice dynamics calculations on ionic crystals are beset by a number of interesting theoretical problems. The most evident problems which distinguish the study of ionic crystals involve the proper treatment of the long range Coulomb interactions between ions. This difficulty has been studied over a period of many decades and significant advances in the handling of the long range Coulomb interaction have been made by Ewald<sup>1</sup>, Born<sup>2</sup> and other workers as we shall detail below. In addition to these long range electrostatic effects, atomic polarization effects in ionic solids have been treated by Dick and Overhauser<sup>3</sup>, Hardy<sup>4</sup>, and Karo and Hardy<sup>5</sup> using shell and deformation dipole models, respectively. The successful description of the lattice dynamics of the lithium halides, however, is still hampered by problems peculiar to these particular ionic compounds. These problems include: 1) the large non-central interactions which are inferred from deviations from the Cauchy relation,  $c_{12} = c_{44}$ , and which in  $LiF$ <sup>6</sup>, has the value of  $c_{12} - c_{44} = -2.25 \times 10^{11} \text{ dyn/cm}^2$ , the largest of all the alkali halides; 2) the importance of next nearest neighbor short-range interactions due to the small size of the lithium atom; and 3) the large anharmonic contributions, especially for the heavier halide salts. In an attempt to address a solution to 1) through 3) above, Verma and Singh<sup>7</sup> found it necessary to employ a modified shell model which included 3-body interactions<sup>8</sup> to calculate the phonon dispersion relations of the lithium halides. Along the lines of Ref. 7, Rastogi et al<sup>9</sup> used a similar model to calculate the phonon dispersion relations and the anharmonic properties of the lithium halides. Their calculation of the real and imaginary parts of the self-energy shift at  $\omega = 0$  and  $\omega = \omega_{TO}$  indicates that

the anharmonic contributions increase substantially with increasing halide size. An important conclusion of their work was that the perturbation approach employed was legitimate for lithium iodide up to 150K, which we believe (see below) is comparable to or less than  $\theta_D(\text{LiI})$ .

In this paper, we investigate the temperature dependence of the infrared lattice vibration absorption of crystalline lithium iodide. We have modified a rigid ion model first proposed by Michielsen et al.<sup>10</sup> Although computer resources have now reached the stage such that more sophisticated potentials, i.e. 3-body interactions<sup>11</sup> and explicit polarization terms<sup>12</sup>, can be employed, the use of a central force interaction potential is justified in this case by the extremely small deviation from Cauchy behavior for lithium iodide<sup>13</sup>;  $(c_{12} - c_{44})/(c_{12} + c_{44}) = 0.005$ . In addition, although polarization certainly affects the dynamical properties of this crystal, the transverse optical mode at  $\vec{k} = 0$ , which is the mode we will be probing, is not affected to a large extent. We are left with the large anharmonicity, which can be handled nonperturbatively by the molecular dynamics method. The molecular dynamics simulation is suitable for investigating thermodynamic and dynamic properties of materials. It has been successfully applied to fast ion conduction and defect diffusion in crystalline solids<sup>14,15</sup>, structural investigations<sup>16,17</sup> and vibrational studies<sup>18</sup> of amorphous solids, and studies of correlated motion of atoms in liquids<sup>19</sup>. One of the main reasons the use of this method has become so widespread is the ease with which results may be compared with experimental data. In principle, any experimentally measurable quantity can also be extracted from the molecular dynamics results. In the present treatment, the frequency

and temperature dependent conductivity (which is measured in the laboratory), and from this the dielectric function, is directly obtained from the current-current correlation function. We have calculated these quantities at two temperatures,  $200K$  which we argue is on the order of the Debye temperature for this material, and  $400K$ , at which we see large anharmonic broadening in the correlation functions. Lowndes<sup>20</sup> has measured the transverse optical frequency  $\omega_{TO}$  using far infrared transmission through ultra thin films at  $T = 5K$  and  $T = T_{room}$ . However, we have not uncovered a measurement of the temperature dependent broadening with which we can compare our results. Other properties that we have calculated are the radial distribution function and mean square displacements of the ions.

The remainder of the paper follows the following outline. In section 2, the crystal structure and relevant properties of  $LiI$  are reviewed. In section 3 we give the potential to be used in this simulation, a variation on one first used by Michielsen et al<sup>10</sup>. The assumptions and constraints inherent in the model will be enumerated. The equations of motion and simulation parameters, such as the timestep, numerical tolerances and temperatures investigated are also given. In addition the determination of the correlation functions, radial distribution function and mean square displacement function is discussed. In section 4, results are presented for two different temperatures, allowing an estimation of the magnitude of anharmonic effects. Finally, in the last section are presented conclusions and suggestions for future study.

## 2. Properties of *LiI*

Lithium iodide crystallizes in the *NaCl* structure. The bravais lattice is face-centered cubic; the basis consists of one *Li* atom and one *I* atom separated by one-half the body diagonal of the conventional unit cell. Each atom has six nearest neighbors of the opposite species. The reciprocal lattice vectors for an fcc lattice are given by the primitive translation vectors of a body-centered cubic lattice. The nearest neighbor distance is  $r_{nn} = 3.00\text{\AA}$  at room temperature<sup>21</sup>, and the cube edge has length  $a = 2r_{nn}$ . There is a relative lack of experimental and theoretical work on this crystal; the former is possibly due to the fact that the solid is extremely hygroscopic. We have uncovered experimental data on the melting temperature<sup>10</sup>, thermal expansion and isothermal compressibility<sup>22</sup>, the high frequency dielectric constant<sup>20</sup>, and lattice energy<sup>10</sup>. The transverse optical frequency at the zone center<sup>20</sup> has been determined using far infrared transmission measurements through ultra thin films; however, the variation of the absorption peak with temperature has not been discussed to our knowledge. A measurement of the elastic constants<sup>13</sup> has yielded  $c_{12} \approx c_{44}$ , indicating that a central force approximation may be a very good one. The other lithium halides, in contrast, show large deviations between  $c_{12}$  and  $c_{44}$ ; the difference for *LiF* is the largest of all the alkali halides. There has also been a measurement of the ionic conductivity of *LiI*.<sup>23</sup> The study of ionic conductivity in the alkali halides has a long history and is known to occur almost exclusively through the diffusion of positive ion vacancies<sup>24</sup>. These vacancies arise either through thermal activation, leading to pairs of positive and negative ion vacancies known as Schottky pairs, or as a result of doping. In our case, there are no defects due to doping, and

TABLE I: Value of the Debye temperature for some alkali iodide compounds.

Substance	$\theta_D$
NaI	164K
KI	132K
RbI	103K

diffusion would be due entirely to Schottky pairs. However, it can be expected that, although ionic diffusion will be quite small in the solid phase of *LiI* without the introduction of impurities or defects, at temperatures not too far below the melting point the lithium may indeed be able to diffuse through interstitial hopping. The iodine ion is huge in comparison to the lithium ion, and may, in effect, leave large channels through which the lithium can move. In the former case of diffusion by Schottky defects, the mobility activation energy and defect formation activation energy have been measured by Jackson and Young<sup>23</sup> to be 0.43 and 1.06eV respectively.

The crystal is single phased throughout the temperature range up to its melting point, which is 742K. Although we have been unable to find a value for its Debye temperature, it can perhaps be estimated by considering the value of this quantity for the other alkali halides. In Table I, we list the Debye temperature for three alkali-iodides<sup>25,26</sup>. By simply extrapolating this data to lithium iodide, we might therefore expect that the value of  $\theta_D$  is of the order of 200K. An analysis which takes into account the variation in sound speed and lattice spacing indicates that  $\theta_D(\text{LiI})$  may be somewhat lower, on the order of 160K.

### 3. Theory

#### 3.1 Interatomic potential

In this work, we have chosen a modified version of an interatomic potential proposed by Michielsen et al<sup>10</sup>. The largest term in the potential, in terms of its contribution to the ground state energy, is unambiguously defined, since *LiI* is an ionic crystal. The Coulomb energy for this solid is found to account for  $\approx 90\%$  of the total potential energy, as is typical for all the alkali halides. A modified Born-Mayer term is used for the short range repulsive term. In addition, dipole-dipole and quadrupole-dipole attractive terms and a hard core repulsive term are included. The pair potential is given by,

$$\phi(r_{ij}) = \frac{z_i z_j e^2}{4\pi\epsilon_0 r_{ij}} + \frac{b}{r_{ij}^4} \exp(-k(r_{ij} - r_{ij0})) - \frac{c_{ij}}{r_{ij}^6} - \frac{d_{ij}}{r_{ij}^8} + \frac{e_{ij}}{r_{ij}^9}, \quad (1)$$

where

$r_{ij}$  = separation of atoms *i* and *j*,

$z_i$  = valence of atom *i*,

$r_{ij0}$  = sum of ionic radii<sup>27</sup>,

$c_{ij}$  = coefficient of dipole-dipole interaction,

$d_{ij}$  = coefficient of dipole-quadrupole interaction,

$e_{ij}$  = coefficient of hard core repulsion,

$b, k$  = parameters fit to thermal expansion and isothermal compressibility.

We can express the total potential energy  $V(r)$  as

$$\frac{V(r)}{N} = -\frac{Ae^2}{4\pi\epsilon_0 r} + \sum_{ij} \left[ \frac{b}{r_{ij}^4} \exp(-k(r_{ij} - r_{ij0})) - \frac{c_{ij}}{r_{ij}^6} - \frac{d_{ij}}{r_{ij}^8} + \frac{e_{ij}}{r_{ij}^9} \right], \quad (2)$$

where  $A$  is the Madelung constant,  $N$  is the number of unit cells,  $r$  is the nearest neighbor distance, and it is understood that the sum does not include the term  $i = j$ . We have used the method of Sangster and Dixon<sup>28</sup> in the evaluation of the long-range Coulomb term with the Ewald summation technique.

There are two parameters in this potential, both in the modified Born-Mayer term, which are fit to experimental data: the prefactor  $b$ , and the inverse decay length  $k$ . We may determine these parameters by considering the following two expressions<sup>29</sup> which relate derivatives of the potential at non-zero temperature to thermodynamic quantities,

$$r_0 \frac{d\Phi}{dr} \Big|_{r_0} = 3T \frac{\alpha V_M}{\beta}, \quad (3)$$

$$r_0^2 \frac{d^2\Phi}{dr^2} \Big|_{r_0} = \frac{9V_M}{\beta} \left( 1 + \frac{T}{\beta} \left( \frac{\partial\beta}{\partial T} \right)_P + \frac{T\alpha}{\beta^2} \left( \frac{\partial\beta}{\partial p} \right)_T + \frac{2}{3} T\alpha \right), \quad (4)$$

where  $\Phi$  is the energy density,  $r_0$  is the equilibrium lattice constant,  $\alpha$  is the thermal expansion coefficient,  $\beta$  is the isothermal compressibility and  $V_M$  is the volume per molecule.

The following are experimental values for the lattice energy  $U$ , thermal expansion coefficient, the isothermal compressibility and two of its derivatives,

$$-U = 754.3 kJ,^{10} \quad (5)$$

$$\alpha = 16.7 \times 10^{-5} K^{-1},^{22}$$

$$\beta = 5.83 \times 10^{-11} m^2 N^{-1},^{22}$$

$$\frac{1}{\beta} \left( \frac{\partial\beta}{\partial p} \right)_T = 37.3 \times 10^{-11} m^2 / N,^{30}$$

$$\frac{1}{\beta} \left( \frac{\partial \beta}{\partial T} \right)_P = 5 \times 10^{-4} K^{-1},^{30}$$

$$\omega_{TO} = 2.7 \times 10^{13} rad s^{-1}.^{20}$$

We desire that the potential energy satisfy the following objectives: reproduce the lattice energy of the crystal; reproduce the frequency of the TO mode at the zone center; lead to the satisfaction of Eqs. (3) and (4). In addition, we of course require that the ions be repulsed as they approach each other, and this sets rather stringent limits on the hard core term  $e_{ij}/r_{ij}^9$ .

We fit the quantities listed above with the following parameters: the magnitude of the prefactor to the Pauli repulsion,  $b$ ; the decay constant  $k$ ; and the magnitudes of the dipole interactions. The strength of the hard core repulsion between the atoms  $e_{ij}$  is in effect fixed. This last statement is true because the repulsion must be strong enough to prevent a double well from developing between ions (these arising from the Coulomb attraction and possibly the dipole interactions), and must be small enough to keep the hard core deep. We have chosen to vary the strength of the dipole interactions from the values given by Ladd<sup>31</sup> because the frequency of the TO mode at  $\vec{q} = 0$  is considerably less than what this model predicts, and the very large coefficients of the dipole interactions are the only parameters which can be varied without adversely affecting the lattice energy and/or the two thermodynamic relations, Eqs. (3) and (4).

The procedure is the following; first the lattice spacing is set to  $3\text{\AA}$  at room temperature, then we adjusted the  $b$  and  $k$  to satisfy the thermodynamic relations given in Eqs. (3) and (4). It should be noted that these relations are not very sensitive to the  $c_{ij}$  and  $d_{ij}$ . The TO frequency is then calculated, we then adjust the  $c_{ij}$  and  $d_{ij}$ ,

TABLE II: Values of the parameters used in LiI calculations, in addition.  $k = 1.1 \times 10^{10} m^{-1}$ ,  $b = 2.8 \times 10^{-58} J m^4$

	Li-I	Li-Li	I-I
$r_{ij0}(\text{\AA})$	3.00	0.95	2.05
$c_{ij}/10^{-79}(J - m^6)$	25.0	8.54	266.0
$d_{ij}/10^{-99}(J - m^8)$	114.	36.8	1000.0
$e_{ij}/10^{-109}(J - m^9)$	6.5	10.0	400.0

re-determine  $b$  and  $k$ , following the same steps until the TO frequency is close to the experimental value  $2.7 \times 10^{13} rad - s^{-1}$ . Finally, the  $e_{ij}$  are adjusted to ensure that there is no attraction between the ions as they approach closer than  $3\text{\AA}$ .

We find the lattice energy to be  $U = 725 kJ$ , within 5% of the experimental value of  $754 kJ$ , Eq. (5). In addition the calculated TO frequency is  $\approx 3.1 \times 10^{13} rad - s^{-1}$ , within 10% of the experimental value of  $2.7 \times 10^{13} rad - s^{-1}$ . The expressions involving the first and second derivatives of the potential are fit exactly at room temperature, and within 5% error at all others. We have varied only the lattice constant as a function of temperature, leaving one parameter and two equations to be fit. This has been done by splitting the difference between the results from the two equations.

We have found that restricting the short range interactions to the second nearest neighbors, as has been done often in the past, is insufficient here. Neglecting terms beyond second neighbors was found to result in a 5% discrepancy compared to the result including their contribution. Therefore, all atoms out to the tenth neighbors are included in this part of the calculation. The values of the parameters used are listed in Table II.

There are certain defects inherent in such a model. Among them are:

1) Tunneling effects, which may well be important considering how small the lithium ion is, and the importance of interstitial diffusion in this system, are neglected.

2) The potential is that of a rigid ion model, so there are no polarization effects present. We are interested in the response at the transverse optical (TO) frequency, however, which is not affected to the same extent that the longitudinal optical (LO) mode is. Although simulations have been successfully performed using rigid ion models for extremely polarizable materials in the past<sup>32,33</sup>, (*AgI*), it would be very desirable to do a molecular dynamics simulation using a shell model potential on this system.

3) Since the parameters of the potential are fit to low temperature experimental data for which the harmonic approximation gives a complete description of the system dynamics, the potential is only accurate near the minimum of the potential energy; we therefore might expect problems at very high temperatures, i.e. in the liquid phase.

We note here that the original potential used in Ref. 10 did not have the hard wall repulsion and therefore did not prohibit pairs of ions from collapsing on themselves. This difficulty is only critical at very high temperatures, where the model crystal is entirely unstable. The absence of a repulsive term in the potential that can counterbalance the Van der Waals terms at small separations leads to a collapse of the pair.

### 3.2 Equations of Motion

We treat a crystal supercell in the form of a cube containing 216 atoms. Periodic boundary conditions are imposed. The classical system of equations to be solved consists of  $216 \times 3 = 648$  coupled differential equations, 3 (corresponding to the cartesian directions) for each of the 216 atoms. The long-range Coulomb force couples atoms at

all distances and is handled by the Ewald<sup>1</sup> method. The reciprocal space summation effectively accounts for the interactions of atoms which are separated by more than one supercell distance, which in our case is  $18\text{\AA}$ . We have solved this system of equations, which include anharmonic contributions exactly, to a numerical accuracy of 1 part in  $10^7$ .

We begin with Newton's equation, a second order differential equation,

$$F_\alpha = m\ddot{x}_\alpha, \quad (6)$$

and express this as two first order coupled ordinary differential equations, (we now drop the cartesian subscript for convenience)

$$\mathbf{F} = \frac{d\mathbf{p}}{dt}, \quad (7)$$

$$\mathbf{p} = m\frac{d\mathbf{x}}{dt}. \quad (8)$$

The force arises from interactions involving all atoms in the supercell and beyond, and is in addition a vector quantity. We indicate a vector quantity with boldface.

Now let us make the following change in scale:

$$m = m'm_0, \quad (9)$$

$$\mathbf{x} = \mathbf{x}'x_0,$$

$$\mathbf{F} = \mathbf{F}'F_0,$$

where  $m_0 = m_p$  is the proton mass,  $x_0 = 10^{-10}m$ , and  $F_0 = 10^{-8}N$ . We also write  $c_{ij} = c_{ij}^0 \times 10^{-79}(J - m^6)$ ,  $d_{ij} = d_{ij}^0 \times 10^{-99}(J - m^8)$ ,  $e_{ij} = e_{ij}^0 \times 10^{-109}(J - m^9)$  and  $b = b^0 \times 10^{-58}(J - m^4)$ . Using  $\mathbf{p}' = \mathbf{p}/\sqrt{m_0x_0F_0}$ , and  $t' = t\sqrt{F_0/x_0m_0}$ , the equations

of motion can be expressed in terms of quantities which are all of order unity, which is necessary from a computational standpoint. We have

$$\mathbf{F}' = \frac{d\mathbf{p}'}{dt'}, \quad (10)$$

$$\mathbf{p}' = m' \frac{d\mathbf{x}'}{dt'}. \quad (11)$$

If these scales are combined, we find that the "real" time is related to the scaled time by  $t' = 2.42 \times 10^{14}t$ . We have employed a scaled timestep of 1 in all simulations presented here, which corresponds to 4.1 femtoseconds.

Now that the time scales are established, it will be necessary to scale the velocities, or momenta, in order to set the effective temperature  $T_{eff}$  of the crystal. We have that  $E_K = \frac{3}{2}Nk_B T_{eff}$ , where

$$E_K = \sum_i p_i^2 / (2m_i). \quad (12)$$

In terms of the scaled, or primed variables, this becomes,

$$\begin{aligned} E_K &= \sum_i \frac{\sqrt{(m_0 F_0 x_0)} p'_i{}^2}{2m'_i m_o}, \\ &= 10^{-18} \sum_i \frac{(p'_i)^2}{2m'_i}, \\ &= 10^{-18} E'_K. \end{aligned} \quad (13)$$

We can solve for  $T_{eff}$ , using  $k_B = 1.38 \times 10^{-23} JK^{-1}$ , and find

$$T_{eff} = \frac{2E_K}{3Nk_B} = 223.6 E'_K. \quad (14)$$

### 3.3 Connections with experimental data

We now turn attention to the current-current correlation function, which will be shown to be related to the conductivity and dielectric constant. First, we define the frequency dependent current density-current density correlation function as

$$\Pi_{\alpha}(\omega) = \int_{-\infty}^{\infty} dt e^{i\omega t} \langle j_{\alpha}(t) j_{\alpha}(0) \rangle, \quad (15)$$

where  $j_{\alpha}(t)$  is the  $\vec{q} = 0$  fourier component of the current density vector and the angular brackets denote an ensemble average. We will refer to the current density-current density correlation function as simply the current-current correlation function. We can express this as<sup>34</sup>

$$\Pi_{\alpha}(\omega) = \lim_{t \rightarrow \infty} \frac{1}{t} \int_0^t dt' e^{i\omega t'} j_{\alpha}(t') \int_0^t dt'' e^{-i\omega t''} j_{\alpha}(t'').$$

These integrations cannot be performed exactly as they extend to  $\infty$ ; however, cutting off the summation at  $t = \tau$  will give the resulting correlation function a width,  $\Delta\omega \approx 2\pi/\tau$ , which can be compared with the actual width.

Many advanced texts on many-body physics discuss the connection between this correlation function and the frequency dependent conductivity. The real part of the conductivity at  $\vec{q} = 0$  can be expressed in terms of the velocity-velocity correlation function as<sup>35</sup>

$$\text{Re}[\sigma_{\alpha\gamma}(\omega)] = \frac{Q^2}{2\hbar\omega V} (1 - e^{-\beta\hbar\omega}) \int_{-\infty}^{\infty} dt e^{i\omega t} \langle v_{\alpha}(t) v_{\gamma}(0) \rangle_G, \quad (16)$$

where the subscript  $G$  indicates an average over a grand canonical ensemble,  $\beta = 1/k_B T$ ,  $Q$  is the particle charge,  $V$  is the crystal volume and  $\hbar$  = Planck's constant divided by

$2\pi$ . Presently, we are only considering the diagonal component of this tensor, we have therefore used the average of the three cartesian components to improve our statistics. All results presented here have been averaged in this way. We can move the factors of  $Q$  and  $V$  into the grand canonical ensemble average to obtain the conductivity in terms of the current density-current density correlation function. Comparing Eqs. (15) and (16), we find that the function we are calculating is related to the frequency dependent conductivity by

$$\Pi(\omega)_\alpha(1 - e^{-\beta\hbar\omega})V/(2\hbar\omega) = \text{Re}[\sigma_{\alpha,\alpha}(\omega)]. \quad (17)$$

We can also relate these expressions to the real and imaginary parts of the dielectric function, which are more amenable to experimental determination.

We have

$$\epsilon(\omega) = (\epsilon_\infty + i\frac{4\pi\sigma}{\omega}); \quad (18)$$

therefore,

$$\text{Im}(\epsilon(\omega)) = 2\pi\Pi(\omega)(1 - e^{-\beta\hbar\omega})V/\hbar\omega^2. \quad (19)$$

We can then find the real part of  $\epsilon(\omega)$  using the Kramers-Kronig relations.

One final observation concerning the calculation of the current-current correlation function is the following: Many quantities derived from molecular dynamics simulations have within them some fluctuations, either from small temperature variations, round-off error, or a lack of suitably long time averaging. This effect is particularly pronounced in correlation functions, which sample over long distances in the crystal. It has therefore

become commonplace<sup>36</sup>, if not standard, to smooth correlation functions with a gaussian which is centered on each data point and whose width is nominally some small quantity. In the results to follow, we have employed such a smoothing procedure using the function

$$\frac{1}{\sqrt{\pi}\delta} \int_{-\infty}^{\infty} d\omega \Pi(\omega) e^{-(\omega-\omega_0)^2/\delta^2}, \quad (20)$$

where  $\omega_0$  is the frequency of interest and  $\delta = 5.7 \times 10^{11} \text{ rad} - \text{s}^{-1}$  which is 3/500 of the full frequency width over which the correlation functions are calculated.

Next we define the mean square displacement as a function of time,  $MSD(t)$ , which is related to the self diffusion of the two ion types in this case,

$$MSD(t) = \langle (r_i(t_0 + t) - r_i(t_0))^2 \rangle. \quad (21)$$

The angular brackets indicate an average over all atoms or ions of type  $i$ .

The direct connection between the mean square displacement and the diffusion coefficient  $D$  for that particular particle is given by<sup>37</sup>,

$$\langle r(t)^2 \rangle = 6Dt, \quad (22)$$

where  $t$  is the time.

We also calculate the radial distribution function, RDF. This quantity simply expresses the average number of atoms within some distance,  $r$ , of some particular atom.

#### 4. Molecular Dynamics Simulation

In this section we give results from molecular dynamics calculations on  $LiI$  at two temperatures. We have calculated the current-current correlation function, the mean

square displacements for the two atoms, and the radial distribution function. The current-current correlation function is related to the ionic conductivity through a factor of  $(1 - e^{\beta\hbar\omega})/\omega$ . We then use the relation between the ionic conductivity and the imaginary part of the dielectric function to find the absorption. The real, or dispersive part of the dielectric function is then calculated from the imaginary part using the Kramers-Kronig relations. We have obtained these quantities at the temperatures 200K and 400K, the first being well below the melting temperature  $T_m$ , which is 742K, and of the same order of magnitude as the Debye temperature ( $\theta_D$ ). The second temperature is still well below  $T_m$  but presumably almost  $2\theta_D$  and should exhibit large anharmonic effects. We account for the thermal expansion of the crystal using Eqs. (3) and (4).

The thermal expansion produces a decrease in the TO frequency as a function of increasing temperature. This is simply understood as a consequence of the atoms moving further from the absolute minimum of their potential energy positions as the temperature increases. In addition to this "static" frequency shift, there is also to be expected a dynamic downward shift in frequency with increasing temperature due to the vibrating atoms reaching into regions of the potential with decreasing curvature.

It is not at all clear that the initial positions and momenta represent an equilibrium configuration; therefore, we integrate the equations of motion ahead for some thermalization time,  $t_{TH}$ . One criterion for determining when this thermalization time has been reached, and the one to be used here, is that the effective temperature  $T_{eff} = E_k/(\frac{3}{2}k_B)$ , varies by less than a couple of percent across the sample, and that it not vary with time. We have tricked the system into quickly achieving this thermal equilibrium in the fol-

lowing way; at the beginning of the simulation, the potential and kinetic energies are calculated, the momenta are scaled to correspond to the desired temperature, then the positions are adjusted so that the kinetic and potential energies have roughly the same value, as they should according to the equipartition theorem. Although this does not result in perfect thermal equilibrium, it decreases the computer time necessary to reach this stage. We used 18,000 timesteps to reach a good thermal equilibrium at 200K and 400K.

#### 4.1 Results and Discussion

We performed simulations on a 216 atom cube with periodic boundary conditions. The cutoff parameter in the Madelung sum was set to 0.35, and we sum over reciprocal lattice vectors up to relative magnitude  $|\vec{h}|^2 = 48$ . The energy and temperature fluctuated less than 4% over the entire simulation time for all the cases presented here. The timestep was 4.1 femtoseconds. This timestep is somewhat arbitrary as the differential equation solver uses as many timesteps as is necessary to meet the tolerance requirements as set by the user, which was set to 1 part in  $10^7$ . We have performed an ensemble average over two sets of different, but random, initial conditions. All of the results presented below have been averaged over these two separate simulations.

We first present results for  $T = 200K$ , for which 18000 timesteps were required for thermalization. The lattice spacing and TO frequency at the zone center for this temperature are  $2.99\text{\AA}$  and  $3.4 \times 10^{13} \text{rad} - \text{s}^{-1}$ , respectively. The correlation functions were calculated over 8000 timesteps and averaged over two sets of random initial conditions. These numbers correspond to  $73.8 \times 10^{-12}$  seconds of thermalization time

and  $32.8 \times 10^{-12}$  seconds of data gathering time. This is indeed a rather short time, however, the correlation functions show little or no change after 6000 steps. We first present in Fig. 1 the imaginary part of the dielectric constant, or the absorption peak from the current-current correlation function at  $T = 200K$ , in arbitrary units. Note the small oscillations superimposed on the main peak; these could be smoothed by widening the width of the smoothing gaussian as described in the previous section. We will encounter these features in the data for  $T = 400K$  as well, and will take up their possible causes and solutions then. The function peaks at the TO frequency at  $\vec{q} = 0$ ,  $3.4 \times 10^{13} \text{rad} - \text{s}^{-1}$  as expected, and shows a small tail, as seen in Fig. 1.

Using the Kramers-Kronig relations<sup>38</sup>, we have calculated the dispersion, or real part of the dielectric function, with the results for 8000 timesteps at  $T = 200K$  also shown in Fig. 1. As is typical, the region of anomalous dispersion coincides with the region of strong absorption.

In Fig. 2 is plotted the radial distribution function for 1500 timesteps. The results for longer run times and for  $T = 400K$  are indistinguishable. It is interesting to note the extremely sharp and well defined peaks corresponding to the various neighbor positions. In Table III we give the number of neighbors and their distances for the rock-salt structure with the nearest neighbor distance normalized to unity. We can identify up to the  $10^{\text{th}}$  neighbor from the graph and see that the area under each peak reproduces the number of the various neighbors very precisely.

Next, in Fig. 3 are given the mean square displacements for  $Li^+$  and  $I^-$  ions at 200K. We note immediately that there is no diffusion, as is expected at this low temperature.

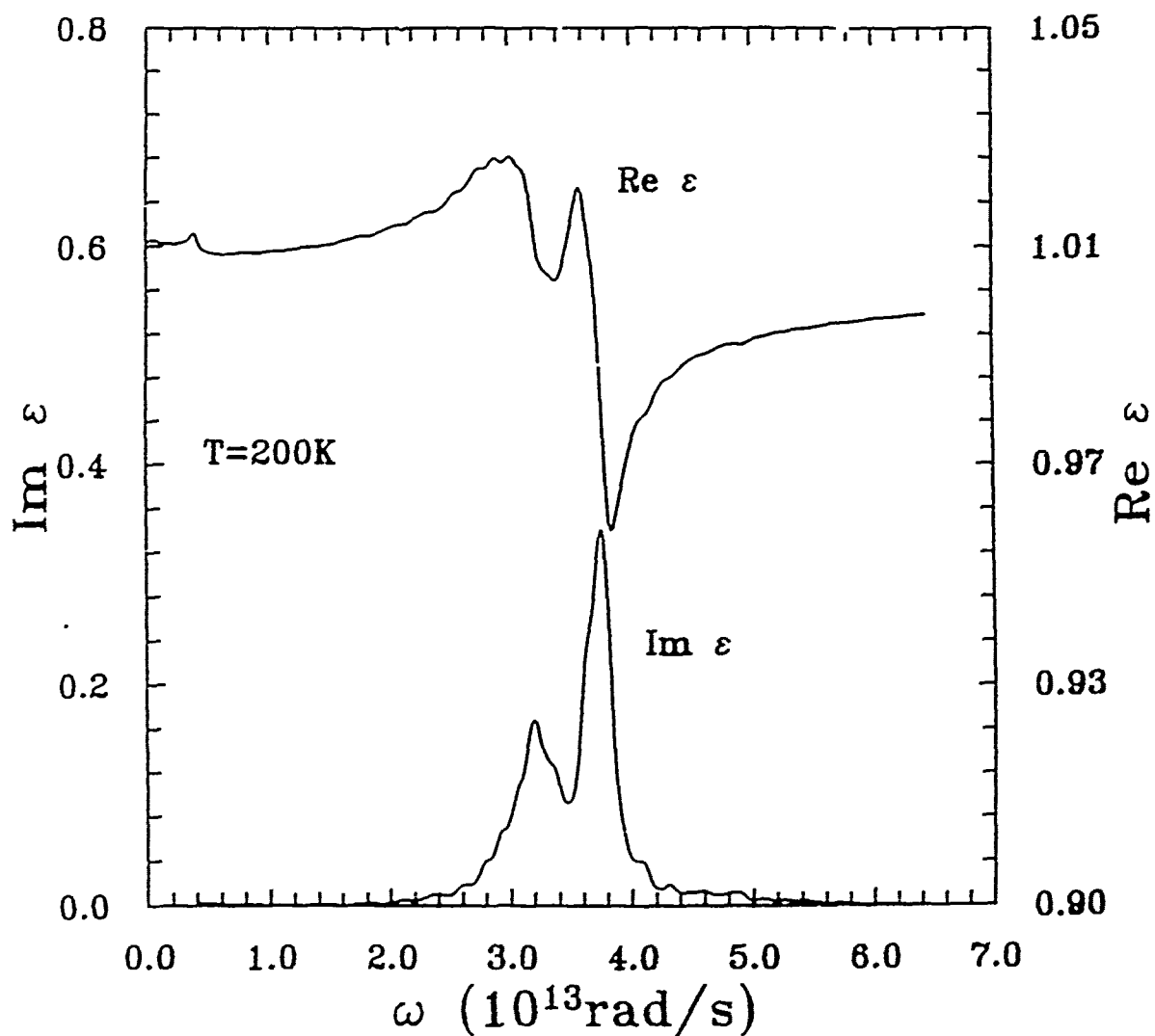


Figure 1: Real and imaginary parts of the dielectric function of *LiI* (in arbitrary units) calculated over 8000 timesteps. This data represents an average over two sets of random initial conditions calculated at a temperature of 200K. The lattice spacing and TO frequency at the zone center are 2.99Å and  $3.4 \times 10^{13} \text{ rad} - \text{s}^{-1}$  respectively.

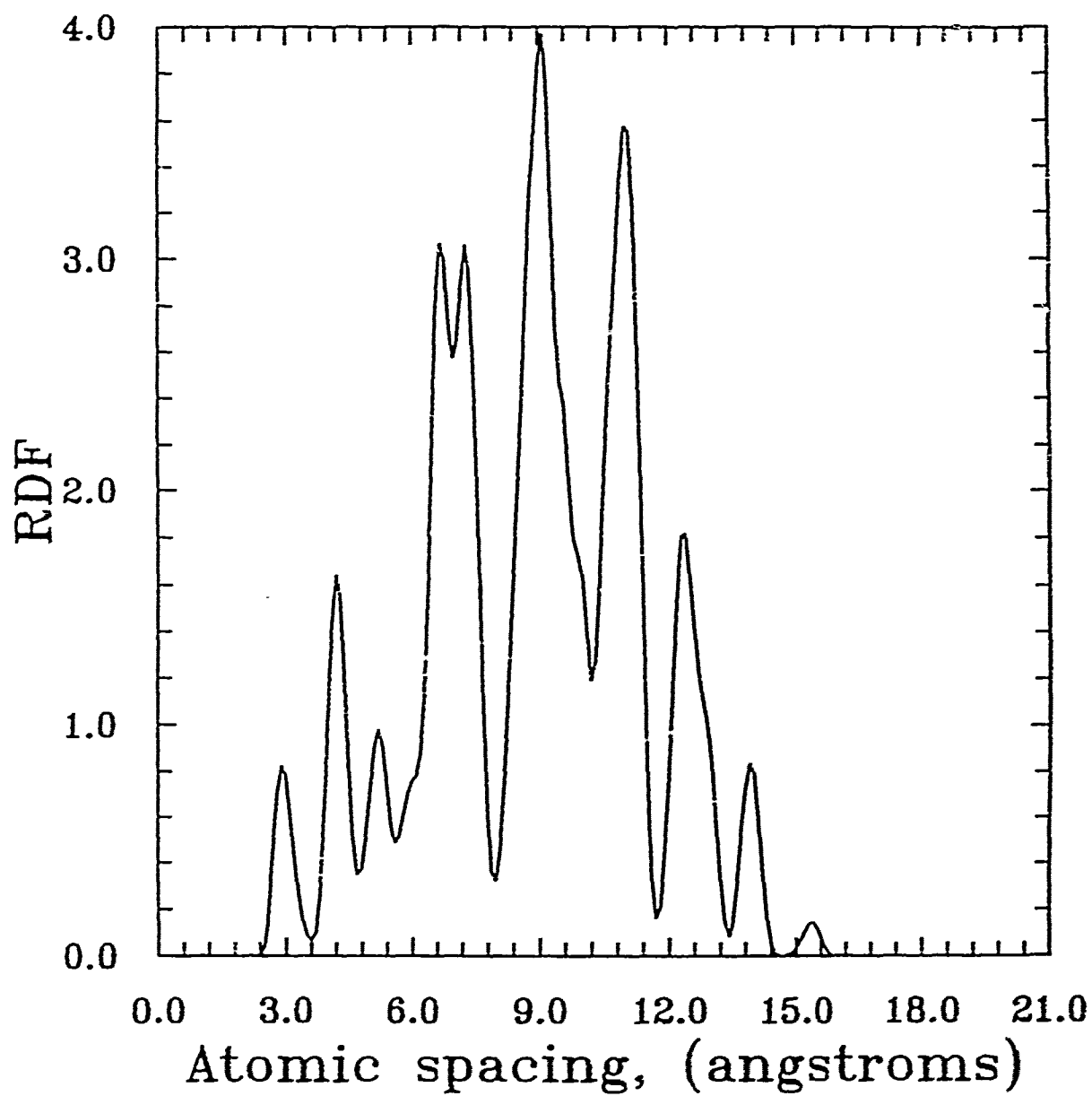


Figure 2: Radial distribution function for *LiI* at 200K. Note that the areas under these extremely well defined peaks correspond to the relevant number of neighbors listed in Table III.

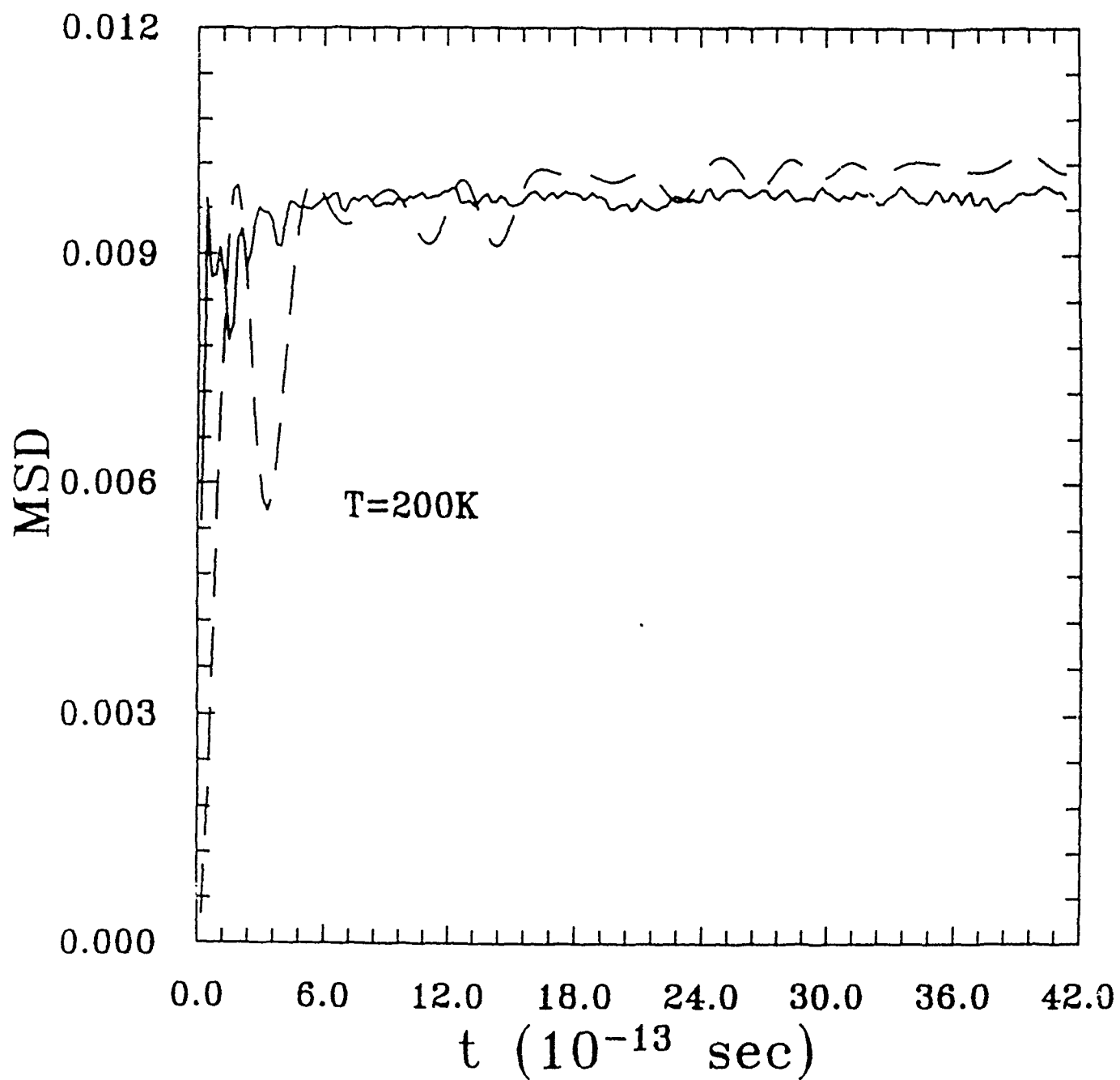


Figure 3: Mean square displacement as a function of time at  $T = 200K$  for iodine, solid line, and lithium dashed line.

TABLE III: Numbers of various neighbors and their distances for *LiI*

Neighbor number	number of neighbors	normalized distance
1	6	1
2	12	$\sqrt{2} \approx 1.41$
3	8	$\sqrt{3} \approx 1.73$
4	6	2
5	24	$\sqrt{5} \approx 2.23$
6	24	$\sqrt{6} \approx 2.45$
7	12	$\sqrt{8} \approx 2.83$
8	27	3
9	12	$\sqrt{10} \approx 3.16$
10	12	$\sqrt{11} \approx 3.32$

If self diffusion were taking place, we would see the mean square displacement increase linearly with time, as indicated in Eq. (22). We can estimate the frequency of oscillation of the lithium using the spacing of the peaks, which is 150 femtoseconds for the lithium and 600 femtoseconds for the iodine. The frequency of the iodine motion is close to one-quarter that of the lithium, which corresponds very closely to the square root of the ratio of their masses, which is  $\sqrt{m_{Li}/m_I} = 0.23$ .

We now turn attention to a simulation on the same system but at 400K. One advantage of performing these calculations at a temperature larger than the Debye temperature is that any inhomogeneities in the initial conditions should be evened out quickly due to the large anharmonicities at work. We have used the same initial positions and momenta as in the previous simulation, but scaled to correspond to this temperature. The interatomic spacing and TO frequency at 400K are  $\approx 3.02\text{\AA}$  and  $2.99 \times 10^{13} \text{rad} - \text{s}^{-1}$  respectively. 18,000 timesteps were used for thermalization, and the same timestep of 4.1 femtoseconds was used throughout.

In Fig. 4 are plotted the absorption and dispersion after 8000 timesteps at 400K. The gross structure of these plots exhibits the following features. The middle of the three maxima occurs very near the TO frequency of  $2.99 \times 10^{13} \text{rad} - \text{s}^{-1}$ , although its exact position cannot be pinned down. The width of the function has increased noticeably, from a full width at half maximum of  $\approx 0.2 \times 10^{13} \text{rad} - \text{s}^{-1}$ , at  $T = 200\text{K}$ , in Fig. 1, to  $\approx 1.2 \times 10^{13} \text{rad} - \text{s}^{-1}$  in Fig. 4. In addition, the length of the high frequency tail is greatly increased at the higher temperature.

One disturbing feature of these correlation functions is the persistence of the periodic maxima and minima. It is found that temporal and ensemble averaging decreases the magnitude of these oscillations. Therefore, we believe this small scale structure to be unphysical and a consequence of the finite time averaging.

Finally in Fig. 5 is plotted the mean square displacement calculated after 8000 timesteps. The magnitude of the displacements for the two species is the same indicating that the temperatures of the two sublattices are the same.

## 5. Conclusion

We have calculated the frequency dependent dielectric function, the radial distribution function and mean square displacements, all as functions of temperature, for crystalline lithium iodide. A rigid ion model was used for the interatomic potential. The various parameters in this potential were fit to the thermal expansion, the isothermal compressibility, the lattice energy and the frequency of the TO mode at the zone center. We have also included a term which acts as a hard core repulsion, preventing the solid from

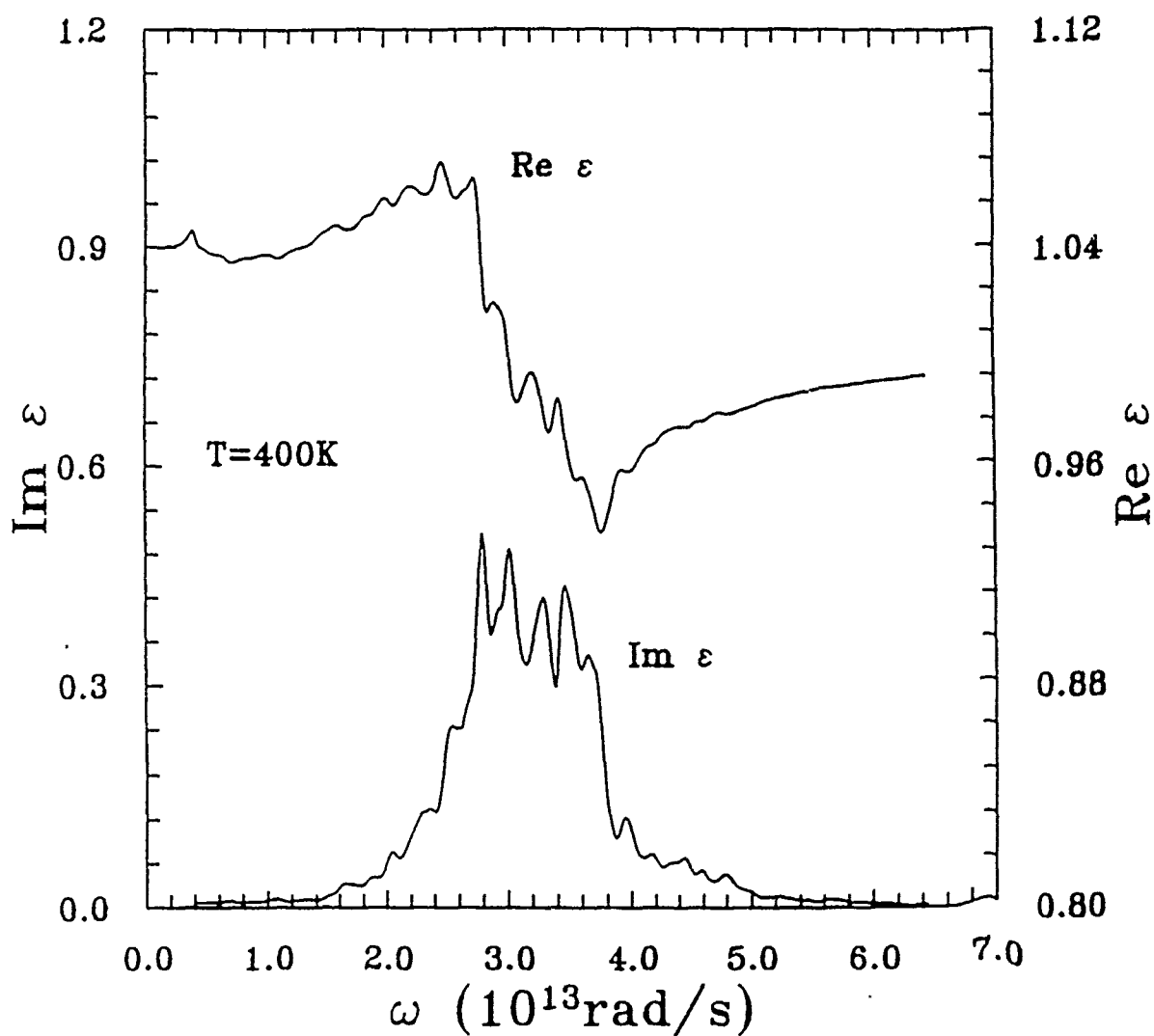


Figure 4: Real and imaginary parts of the dielectric function at  $T = 400K$  after 8000 timesteps of data taking. The lattice spacing at this temperature is  $3.02\text{\AA}$ . This absorption peaks near the TO frequency of  $2.99 \times 10^{13}\text{rad} \cdot \text{s}^{-1}$ , however, the broadness inhibits an exact determination of the peak position.

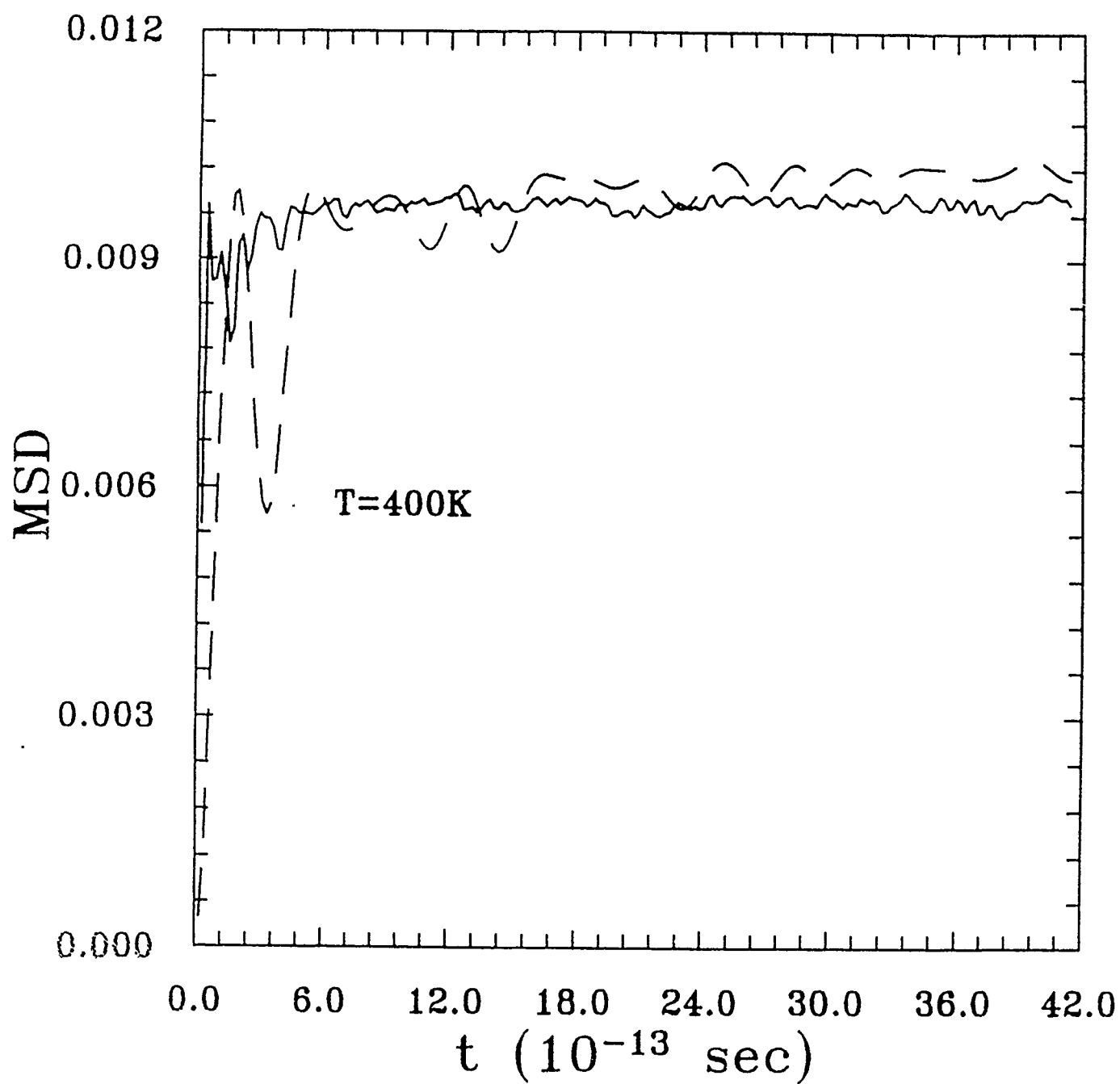


Figure 5: Mean square displacement as a function of time at  $T = 400\text{K}$  for iodine, solid line, and lithium dashed line.

collapsing at high temperatures.

A large increase in anharmonic broadening in the frequency dependent correlation functions was observed in passing from  $T = 200K$  to  $T = 400K$ , indicating that the Debye temperature for this material most likely lies in this range, as we had inferred from data from other alkali iodides (see Table I). We have been able to reproduce the TO frequency within 10% of the experimental value, although no experimental measurement of the temperature dependence of the infrared absorption or dispersion for this material has been found. It would be very interesting if experimental data on these temperature dependences were to become available to provide a comparison with our theoretical results.

## References

- [\*] Present address: Laboratoire de Physique des Solides, Université Pierre et Marie Curie, 4 Place Jussieu, 75252 Paris Cédex 05, France.
- [\*\*] Permanent address: Laboratoire de Physique des Solides, Université Pierre et Marie Curie, 4 Place Jussieu, 75252 Paris Cédex 05, France.
- [+] Permanent address: Department of Physics, Western Michigan University, Kalamazoo, MI 49008-5151.
- [1] P. P. Ewald, Ann. Phys.(Leipzig) 54, 519, 557 (1917).
- [2] M. Born, *Atomtheorie des festen Zustandes* (J. B. Teubner, Berlin, 1923).
- [3] B. G. Dick and A. W. Overhauser, Phys. Rev. 112, 90 (1958).
- [4] J. R. Hardy, Phil. Mag. 7, 315 (1962).
- [5] A. M. Karo and J. R. Hardy, Phys. Rev. 129, 2024 (1963).
- [6] C. V. Briscoe and C. F. Squire, Phys. Rev. 106, 1175 (1957).
- [7] M. P. Verma and R. K. Singh, Phys. Stat. Solidi 33, 769 (1969).
- [8] R. K. Singh, J. Phys. C. 4, 2749 (1971).
- [9] A. Rastogi, J. P. Hawranek and R. P. Lowndes, Phys. Rev. B. 9, 1938 (1973)
- [10] J. Michielsen, P. Woerlee, F. v.d. Graaf and J. A. A. Ketelaar, J. of Non-Cryst. Solids 101, 101-110 (1988).

- [11] P. M. Roger A. J. Stone and D. J. Tildesley, Chem. Phys. Let. 145, 365 (1988).
- [12] P. A. Madden and J. A. Board, J. Chem. Soc. Fara. Trans. II 83, 1891 (1987).
- [13] K. O. McClean and C. S. Smith, J. Phys. Chem. Solids 33, 275 (1972).
- [14] M. J. Gillan, Physica 131B, 157 (1985).
- [15] J. Moscinski and P. W. M. Jacobs, Proc. Roy. Soc. of London A 398, 141 (1985).
- [16] P. Vashishta, R. K. Kalia and I. Ebbsjo, J. Non-Cryst. Sol. 106, 301 (1988).
- [17] Q. Xu. K. Kamamura and T. Yokokawa, J. Non-Cryst Sol. 104, 261 (1988).
- [18] W. A. Kamitakahara, R. Biswas, A. M. Bouchard and F. Gompf, Physica B 156.157, 213 (1989).
- [19] A. Rahman, Phys. Rev. 136, A405 (1964).
- [20] R. P. Lowndes and D. H. Martin, Proc. Roy. Soc. A. 308, 473 (1969).
- [21] See e.g., C. Kittel, *Introduction to Solid State Physics*, 5<sup>th</sup> edition, (John Wiley and Sons, New York, 1976), p. 92.
- [22] M. P. Tosi, Solid State Phys. 16, 1 (1964).
- [23] B. J. H. Jackson and D. A. Young, Phys. Chem. of Solids 30, 1973 (1969).
- [24] A. B. Lidiard, *Handbuch der Physik*, edited by S. Flugge (Springer-Verlag, Berlin, 1957), Vol. 20, p. 246.
- [25] M. P. Tosi and F. C. Fumi, Phys. Rev. B 131, 1458 (1963).

- [26] A. I. P. Handbook, D. W. Gray ed. (McGraw-Hill Book co., New York, 1973), p. 4-116.
- [27] L. Pauling, *The Nature of the Chemical Bond*, (Cornell University Press, Ithaca, NY, 2<sup>nd</sup> edn., 1940).
- [28] M. J. L. Sangster and M. Dixon, *Adv. Phys.* 25, 247 (1976).
- [29] M. Born and J. E. Mayer, *Z. Phys.* 75, 1 (1932).
- [30] D. Cubicciotti, *J. Chem. Phys.* 31, 1646 (1959).
- [31] M. F. C. Ladd, *J. Chem. Phys.* 60, 1954 (1974).
- [32] P. Vashishta and A. Rahman, *Phys. Rev. Lett.* 40, 1337 (1978).
- [33] M. Parrinello, A. Rahman and P. Vashishta, *Phys. Rev. Lett.* 50, 1073 (1983).
- [34] J. P. Hansen and M. L. Klein, *Phys. Rev. B* 13, 878 (1976).
- [35] R. F. Wallis and M. Balkanski, *Many-Body Aspects of Solid State Spectroscopy* (North- Holland Physics, New York, 1986), p.49.
- [36] A. R. McGurn, A. A. Maradudin, R. F. Wallis and A. J. C. Ladd, *Phys. Rev. B* 37, 3964 (1988).
- [37] R. K. Pathria, *Statistical Mechanics*, (Pergamon Press, Oxford. 1972), p. 455.
- [38] see e.g., G. Arfken, *Mathematical Methods for Physicists*, (Academic Press, Inc., Orlando, 1985) p. 425.

### III. Publications

1. "Lattice-Dynamics and Network-Dynamics Studies of Vibrational Modes in Lithium-Doped Borate Glasses," J. Deppe, M. Balkanski and R. F. Wallis, Phys. Rev. **B41**, 7767 (1990).
2. "Effect of Intercalated Lithium on the Direct Band Gaps of Indium Selenide," P. Gomes da Costa, M. Balkanski and R. F. Wallis, Phys. Rev. **B43**, 7066 (1991).
3. "Dynamical Properties of Fast Ion Conducting Borate Glasses," M. Balkanski, R. F. Wallis, J. Deppe and M. Massot, Festschrift for Rogério Leite, to appear.
4. "Lattice Vibrational Properties of  $\gamma$ -InSe With and Without Intercalated Lithium," P. Gomes da Costa, M. Balkanski and R. F. Wallis, Festschrift for Rogério Leite, to appear.
5. "Lattice Dynamics and Network Dynamics Calculations on Vibrational Modes of Lithium Borate Glasses," J. Deppe, M. Balkanski, R. F. Wallis and M. Massot, Mat. Res. Soc. Symp. Proc., **210**, 125 (1991).
6. "Electronic Energy Bands in  $\gamma$ -InSe With and Without Intercalated Lithium," P. Gomes da Costa, M. Balkanski and R. F. Wallis, Mat. Res. Soc. Symp. Proc., **210**, 137 (1991).
7. "Molecular Dynamics Study of the Lattice Vibration Contribution to the Frequency-Dependent Dielectric Constant of Lithium Iodide," J. Deppe, M. Balkanski, R. F. Wallis and A. R. McGurn, Phys. Rev. B, submitted for publication.
8. "Dynamical Properties of Fast Ion Conducting Borate Glasses," (review paper) M. Balkanski, R. F. Wallis, J. Deppe and M. Massot, Materials Science and Engineering B, to appear.

IV. Ph.D. Theses Completed

1. J. Deppe: "Ionic Conductivity and Vibrations of Glasses and Molecular Dynamics of Lithium Iodide," University of California, Irvine, 1990.
2. P. Gomes da Costa: "Theoretical Investigations of the Effects of Lithium Intercalation on the Properties of Indium Selenide", University of California, Irvine, 1990.